

UNIVERSITÀ DEGLI STUDI DI PADOVA

Dipartimento di Fisica e Astronomia “Galileo Galilei”

Corso di Laurea Magistrale in Fisica

Tesi di Laurea

Development and characterization of an atmospheric plasma source for non-thermal blood coagulation

Relatore

Prof. Emilio Martines

Correlatore

Dr. Gianluca De Masi

Dr. Luigi Cordaro

Laureando

Davide Mancini

Anno Accademico 2018/2019

Abstract

In this thesis is developed and characterized Plasma Coagulation Controller (PCC): a cold atmospheric plasma source designed for acceleration of non thermal blood coagulation. PCC is based on the Dielectric Barrier Discharge (DBD), it ionizes a neutral gas through the application of a fast voltage pulse to an electrode covered in dielectric material. Electrical characterization of the prototype developed in this work allows to observe voltage pulses with amplitude up to 10 kV while current intensity is always lower than 10 mA, for repetition rates from 1 to 40 kHz. A peculiar phenomenon in DBD sources is that plasma propagates producing *bullets*: localized zone of plasma expelled at velocities higher than 10 km/s. In this work plasma bullets are observed with a fast frame acquisition setup that allows to observe the discharge with an integration time of 15 ns. The principal analysis revolves around production and propagation of plasma bullets with different experimental setups such as: voltage pulse amplitude, composition of neutral gas (chosen between helium, neon and argon) or typology of the target placed in front of the source (e.g. insulating or conductive targets). The comparision of bullets produced with helium and neon gas suggests that bullet propagation velocity is related to electron mobility. The measurements of current intensity in a conductive target allows to observe that current flows in the target before impact with the bullet. Bullets are not observed using argon, with this gas plasma dynamics is characterized by the production of filaments that differs from bullets. Emission spectroscopy analysis is performed assuring the presence of OH, N₂ and N₂⁺ molecules, with different intensities for different operational regimes. The relative emission of gas components is studied for different plasma positions and gas composition, finding that during plasma propagation in air emission is always dominated by nitrogen transitions. Temperature increase due to plasma application on an inorganic target is measured with a thermal camera. Power deposition of a single voltage pulse is found to be inversely proportional to pulse repetition rate and to target distance, while it increases with higher voltage peaks.

Contents

1	Introduction	7
1.1	Plasma medicine	7
1.2	Cold Atmospheric Plasma	8
1.2.1	Plasma generation	9
2	Plasma source description and electric characterization	15
2.1	General source description	15
2.2	Electric scheme	17
2.3	Output characterization	19
2.3.1	Measurements without gas	19
2.3.2	Measurements with gas	20
2.3.3	Effective current	25
2.3.4	Plasma impedance estimate	25
3	Plasma dynamics	29
3.1	Experimental setup	29
3.1.1	Source, power lines and electric signals	32
3.1.2	Trigger synchronization	32
3.1.3	Different setups	33
3.1.4	Frame analysis and calibration	35
3.2	Helium flow	36
3.2.1	Bullet description	36
3.2.2	Voltage influence	40
3.2.3	Flow influence	42
3.2.4	Insulating target	44
3.2.5	Conductive target	45
3.3	Neon flow	50
3.3.1	Bullet description	52
3.3.2	Insulating target	52
3.3.3	Conductive target	55
3.4	Argon flow	55
3.4.1	Dynamics example	57
3.4.2	Absence of target	60
3.4.3	Influence of target	60
3.5	Hints on bullet propagation model	63
3.5.1	Ion waves or electron drift	66
3.5.2	Mobility and velocity	68
4	Plasma spectrum	71
4.1	Optical Emission Spectroscopy	71
4.2	Line recognition	72
4.2.1	Emission measurements	73
4.2.2	Pulse settings	77

4.2.3	Estimation of plasma temperatures	77
4.3	Line intensity analysis	80
4.3.1	Experimental setup	81
4.3.2	Position	82
4.3.3	Gas composition	82
5	Plasma power estimate	87
5.1	Experimental setup	87
5.2	Temperature profile	88
5.3	Power estimation	89
6	Conclusions	95

Chapter 1

Introduction

Plasma medicine is an emerging field that is broadening its applications from uses on medical equipments (sterilization, decontamination) to uses on living tissues [1]. One of the research groups working in Consorzio RFX laboratories, in Padova, developed a source for the production of Cold Atmospheric Plasma (CAP) to be used for medical treatment on biological tissues: Plasma Coagulation Controller (PCC) [2]. The source is a Dielectric Barrier Discharge reactor, where a dielectric is used to produce plasma with low charge density. It is developed to promote non thermal blood coagulation, i.e. acceleration of blood clot formation thanks to plasma direct application.

CAPs are of particular interest in plasma medicine for two characteristics:

- **Cold plasma** : given non thermal equilibrium and ion low temperature, this plasma can be applied on surfaces without a dangerous increase in target temperature. In plasma medicine CAPs allow treatment on living tissues, where target temperature must be kept below a safe value.
- **Reactive Species** : When a gas is ionized at atmospheric pressure, the produced plasma is mixed with the surrounding air molecules. The peculiarity of a plasma in air is the presence of reactive species, ions, produced by ionization and recombination of nitrogen, oxygen, water and other atoms or molecules. There are several biological processes where activation and reactions speed is thought to be related to concentration of Reactive Oxydant Species (ROS) and Reactive Nitrogen Species (RNS) [3], [4].

In this chapter there is the presentation of some results obtained with PCC and a general description of the production of CAP, describing the sources developed at Consorzio RFX.

1.1 Plasma medicine

The most studied therapeutic effects of plasma application are:

- sterilization and decontamination [5], [6];
- blood coagulation [7];
- wound disinfection and healing [8];
- cancer cell treatment [9].

How plasma interacts with living tissues and produces those effects is not fully understood. Reactive species, along with UV radiation and electromagnetic field, are considered fundamental participants of the mechanism.

Previous works studied PCC induced bactericidal effects and non thermal blood coagulation; in the following their results will be described briefly.

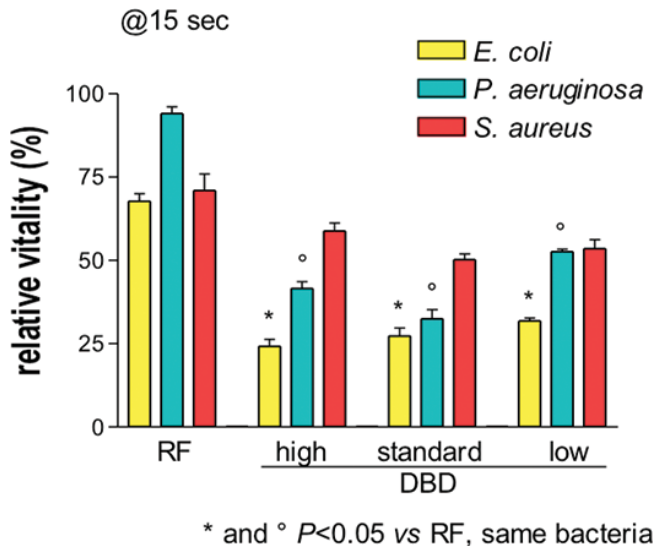


Figure 1.1: Relative vitality on different bacteria colonies after plasma treatment of 15 s with different sources. On the left there is treatment with an RF plasma source; on the right there is treatment with the DBD plasma source studied in this work, PCC, for three different combinations of parameters for the discharge (low, standard and high).

Bactericidal effects There are numerous studies on the effects of CAPs on bacteria [10], [11], however mechanisms leading to inactivation of bacteria are not fully understood. It is thought that plasma application has an effect when reactive species, UV photons and charged particles come into direct contact with cell's membrane and structures [1].

In figure 1.1 is presented the reduction of bacteria vitality due to application of plasma produced with our sources. From the figure it's possible to see results of the experiment on three different bacteria species, for an RF source and for the DBD source, PCC, with three different experimental setups. PCC seems to have a faster effect on the reduction of bacteria, for all analyzed species.

Blood coagulation Cauterization devices that produce quasi-thermal blood coagulation with high-temperature plasma have been used for a long time in wound treatment and surgery. Only recently studies shown that with cold plasma application is possible to induce natural blood coagulation, without temperature increase [7], [12]. Treatments with CAPs activate the coagulation cascade shown in figure 1.2, a chain of reactions that involves many tissue factors and proteins. The exact mechanisms that accelerates clot formation have to be understood yet, as of today studies show that plasma induces the production of fibrin that catalyses blood coagulation factors [1].

Treatment with PCC is done applying plasma on blood samples, as shown in figure 1.3 (a). The study involves the use of different plasma application times and different discharge parameters. The effect of plasma application is evaluated from samples as those in figure 1.3 (b), where the blood is removed and the area of the remaining coagulated blood is measured, leading to results in figure 1.3 (c). Results show always an increase on blood coagulation when treated with plasma.

1.2 Cold Atmospheric Plasma

In a CAP thermodynamical equilibrium is not reached. Electron energy is usually much higher than ion energy [13]. In those conditions plasma dynamics can be described as the collective motion of two interpenetrating fluids, where the thermal motion of ions can be ignored [14]. There are several studies on CAP plasma characteristics [15], [16], [17] typical values are electron temperatures between $T_e = 1 - 10 \text{ eV}$ and electron densities between $n_e = 10^{17} - 10^{22} \text{ m}^{-3}$, inside the box outlined in figure 1.4.

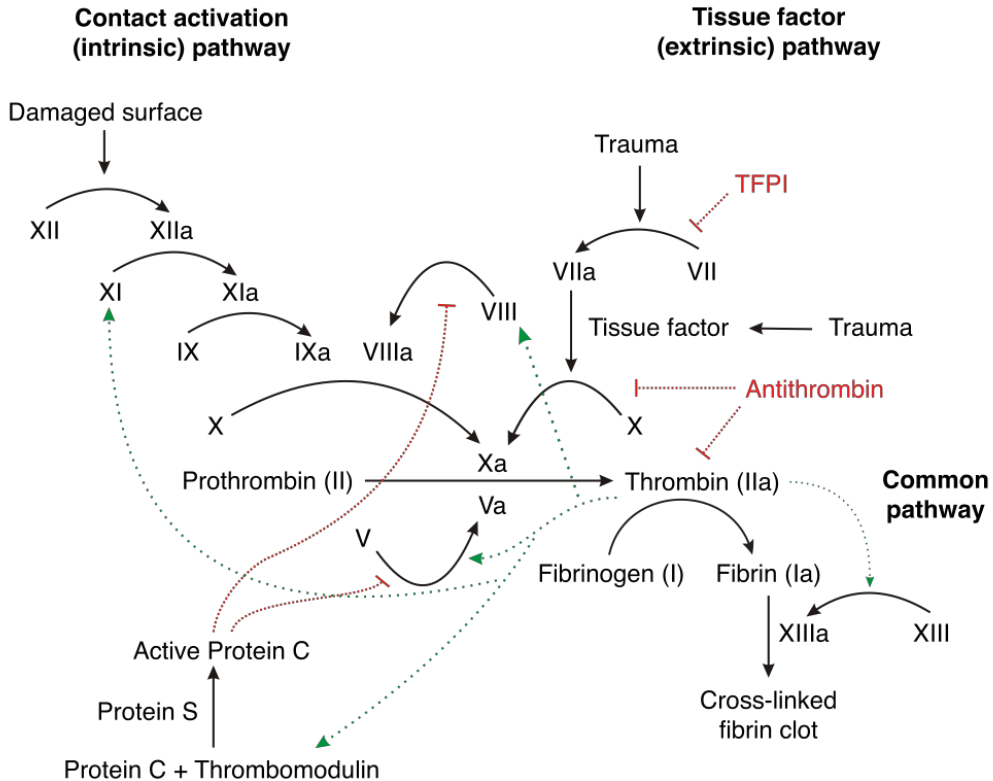


Figure 1.2: Reaction chain that leads to blood coagulation. The analysis of blood samples treated with plasma, allows to find where and how plasma intervenes in this scheme.

1.2.1 Plasma generation

Electron density in CAPs is much smaller than the neutral density of an ideal gas $n_n = 2.50 \times 10^{25} \text{ m}^{-3}$. However it is higher than the density of free electrons naturally present in air at atmospheric pressure. Radioactive substances and cosmic rays generates electron-ion pairs with a total ionization rate of $10^7 \text{ m}^{-3}\text{s}^{-1}$ [18].

The application of a steady electric field to a gas accelerate free electrons that collide with atoms and molecules resulting in excitation or ionization reactions. If the electric field has enough intensity it extract electrons from atoms and molecules ionizing them. Those reactions form ion-electron pairs that are accelerated producing other pairs, inducing chain reactions that could sustain plasma discharge. If and how this process starts is influenced by:

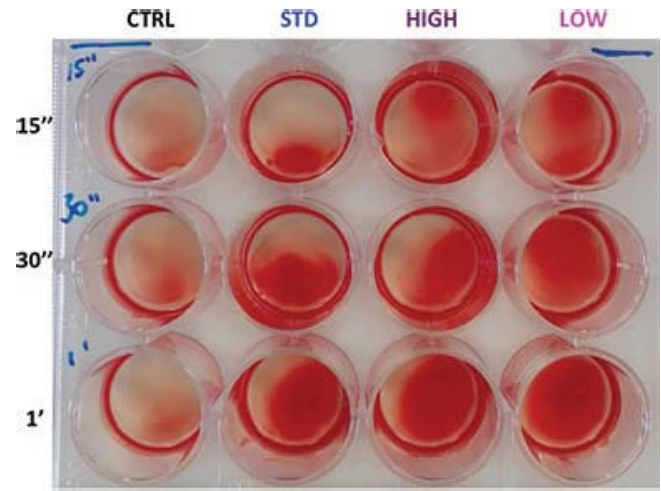
- gas species, by their ionization potential and cross section for different reactions
- characteristics lenght of the system, that influences charged particle's acceleration
- gas pressure, that is proportional to reaction rates

Generally electrons acquire more energy from the electric field due to the lower mass and higher mobility, so electronic temperature increases more rapidly then ion temperature. If we apply a steady DC electric fields, electrons and ions reach thermal equilibrium trough collisions, generating thermal plasma at high temperatures. To avoid thermalization and produce cold plasma at high densities is possible to give energy selectively to electrons with AC electric fields at high frequency [19].

Two examples of sources that produce plasma for medical application are the ones built at RFX: the RF source based on a radio transmitter ([5]) and the DBD source, studied in this work ([2]).



(a) Picture of plasma application.



(b) Coagulated blood samples.

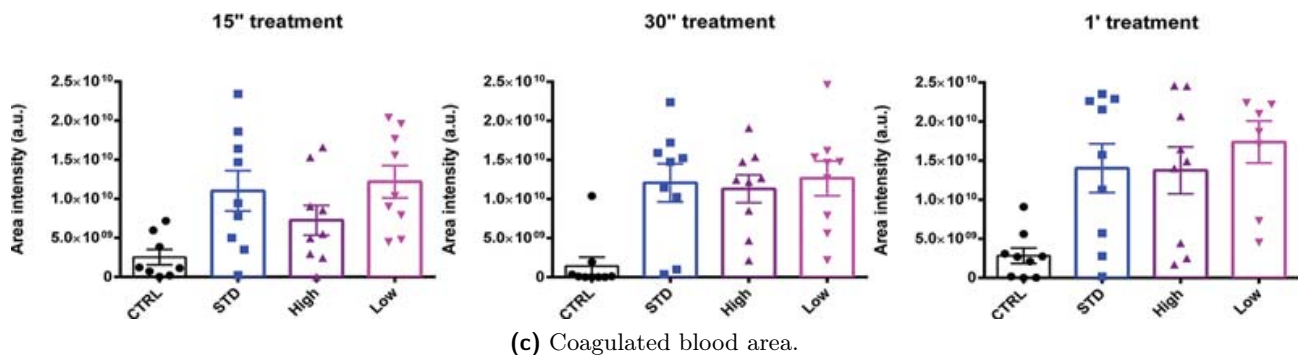


Figure 1.3: Pictures and results of the blood coagulation study with PCC. Blood samples are treated with three different parameters of the DBD discharge, for three different application times. In (c) is possible to see the increase of coagulated blood area for samples treated by plasma, if compared to the control sample.

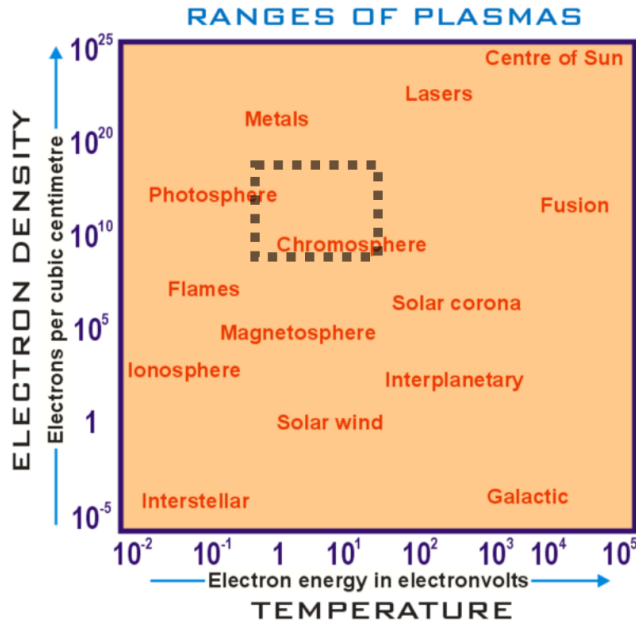


Figure 1.4: Plasma classification in function of electron density and electron temperature. Inside the square there are typical parameters for CAPs.

RF source The RF source developed in RFX works applying an AC electric field between two electrodes. It is composed by two coaxial tubes as shown in figure 1.5: the internal one is connected to a radio transmitter in series with a matching network and with an electrode formed by a wire grid; the external one ends with a second electrode fixed at ground potential. The radio transmitter works with fixed power (5 W) and is set to a specific frequency that is the resonance frequency for the LC series circuit formed by the inductance in the matching network and the parasitic capacitance of the device. When neutral gas flows inside the inner tube, the electric field between the electrodes ionizes it, producing cold plasma in air. The source is built with an inductance of $100 \mu\text{H}$, capacitance is estimated as 10 pF , resulting in a resonance for a frequency around 4.8 MHz, reaching voltage peak to peak values up to 900 V on the electrode. By setting an appropriate gas flow, the discharge starts more easily and to reach lower peak voltage values. This source produces plasma directly in air, so it ionizes a mixture of neutral gas and air, giving birth to plasma rich in reactive species coming from oxygen and nitrogen molecules. The presence of reactive species allows to use this source for non-thermal sterilization of living tissues: plasma produced by it has bactericidal effects and does not damage human cells ([20]).

DBD source The source developed in this work is based on the Dielectric Barrier Discharge (DBD): it applies an electric field on the gas with one electrode or a pair of electrodes, where a dielectric covers at least one of them, as in figure 1.6. The dielectric works as an insulator and does not allow DC current to flow in the gap, so gas between the electrodes can be ionized without large current densities flowing through the resulting plasma ([21]). The discharge can be modeled as in the circuit in figure 1.6 (b) ([22]), C_1 is capacitance of dielectric, C_2 of air and R_p and C_p are plasma resistance and capacitance (in other studies it is possible to find more refined models [23]). Typical values for discharge parameters are AC voltage frequency or pulse rates $f \geq 1 \text{ kHz}$, voltage peak values from $V_p = 1 - 20 \text{ kV}$, and current peak intensities on a conductive target $I < 100 \text{ mA}$.

DBD plasma reactors changed in the last decades following the development of pulse power technology: from the classic sinusoidal voltage now is common to apply pulsed voltage. Plasma generated with sub-microseconds voltage pulses allows to avoid local discharges overheat and increases discharge production of reactive species inside the plasma ([24]). Those progresses in DBD plasma technology led to the development of sources for biomedical plasma applications. Those plasma sources, including PCC, have to produce plasma rich in reactive species, while meeting stringent requirements such as low

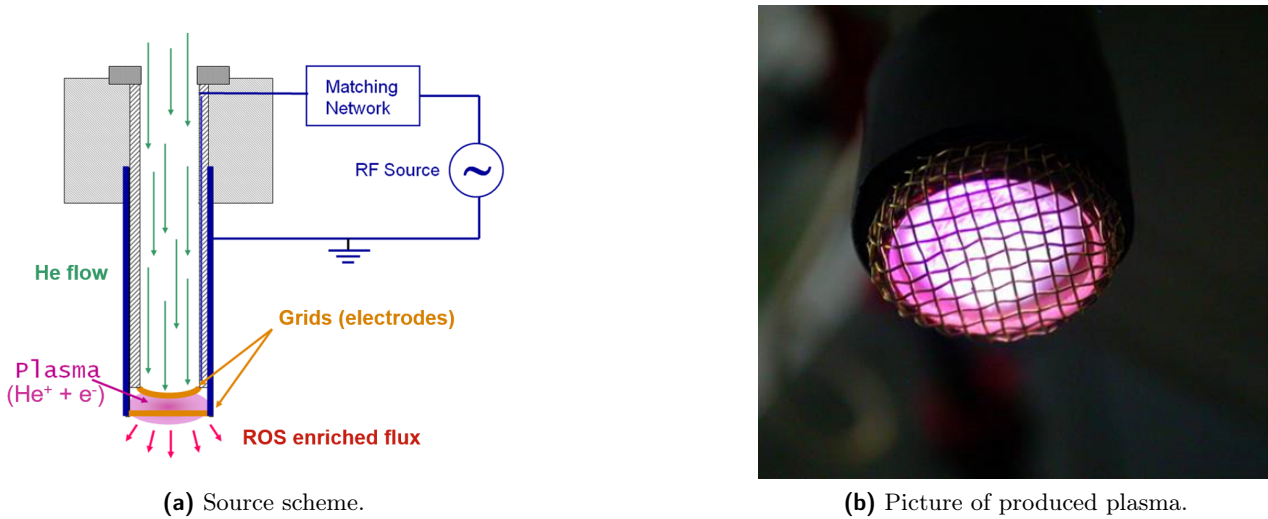


Figure 1.5: Plasma RF source developed in RFX.

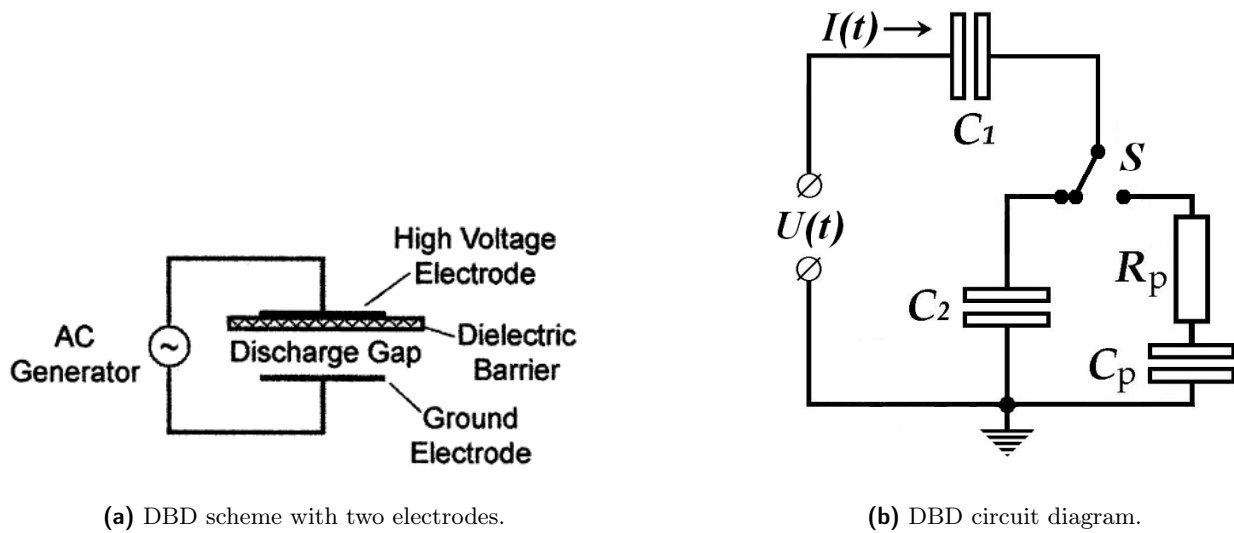


Figure 1.6: Representation of the concept behind DBD plasma production: on the left an experimental setup composed by two electrodes, one dielectric and a voltage AC generator; on the right a circuit diagram of the setup for DBD discharge. In the circuit, C_1 is the dielectric capacitance, C_2 the air capacitance, C_p and R_p are plasma capacitance and resistance.

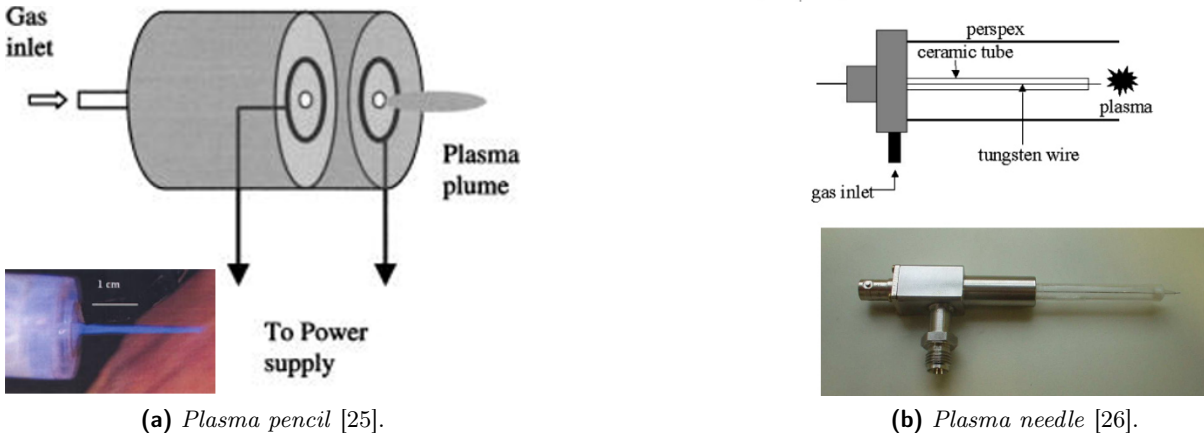


Figure 1.7: Two example of DBD plasma sources for medical applications. In both sources we have one electrode that applies an electric field to neutral gas, ionizing it. Plasma is then expelled in air at atmospheric pressure.

temperature (at or near room temperature), no risk of arcing, operation at atmospheric pressure, preferably hand-held operation, low concentration of ozone generation, etc.

The design used in many works is in figure 1.7 ([25], [26]): a cylindrical electrode is covered in dielectric material and inserted in a tube with neutral gas flowing in it. The gas, typically helium or argon, allows to start plasma discharge, then plasma is expelled in air where it produces reactive species needed for medical treatment. PCC developed and studied in this thesis will be described in details in chapter 2, along with its electrical characterization.

An interesting phenomenon in sources with this design is plasma formation and propagation. High speed camera measurements of the process show that plasma is not produced in a uniform steady column, but every pulse of the electric field gives start to localized plasma emission. Once produced, the ionization wave moves from the electrode and propagates in air, with velocities from 10 to over 150 km/s. Those localized plasma emissions are called “bullet” and only recently is possible to find models that describe them [27]. In this thesis this phenomenon is observed and studied in details in chapter 3, with different voltage pulse parameters, target position and gas composition.

As said before, the purpose of non thermal plasma application for medical uses is the deposition of reactive species on biological tissues. The presence and characteristics of reactive species can be studied by emission spectroscopy, with intensity and temperature estimation. Chapter 4 is dedicated to the study of plasma radiation emission around visible wavelengths.

The other fundamental feature of plasma produced by our source is that can be applied on human body without danger. Temperature measurements on the target of plasma application can lead to an estimation of plasma power deposition. In chapter 5 are presented thermocamera measurements and power estimation.

Chapter 2

Plasma source description and electric characterization

Plasma Coagulation Controller (PCC) developed at Consorzio RFX is a DBD cold plasma source that produces plasma at atmospheric pressure for biomedical applications. The entire design is developed to guarantee the flexibility necessary to easy application on target. In this chapter the source functioning scheme is described and its features are characterized.

2.1 General source description

Plasma is produced applying a fast high voltage pulse (from 2 to 10 kV) to a cylindrical electrode covered by pyrex glass. The glass act as a dielectric allowing to produce plasma in DBD conditions [2]. The electrode is positioned along the axis of a nozzle where there is a flow of neutral gas that allows to start the discharge. The gas is a pure noble gas, sometime mixed with other gasses. It is possible to put a second electrode formed by a conducting ring around the nozzle, set to ground voltage or other voltage values, to modify the electric field if necessary.

The electrode generates an electric field that ionizes the gas producing plasma with low free charge density thanks to the glass dielectric. Plasma forms a column of glowing gas, the plasma plume, that goes out from the nozzle exit and travels in the air outside, until it reaches a certain lenght or a target, as shown in figure 2.1. The plume is formed by cold plasma, it can be touched without a relevant increase of temperature on the skin or any other danger.

PCC development goes through different designs (an example of the first one is described in [28]). In this work are studied two different prototypes, here named **A** and **B**, with same concepts and little differences.

PCC is made of two modules: a controller box and a source head, shown in figure 2.2.

The high voltage controller is separated from the head, the first one controls the trigger for the voltage pulse, the second one is where there is plasma production. The controller contains power cables and circuits and an Arduino Leonardo that controls pulse repetition rate and amplitude, as explained later. The head is a cylinder 30 cm long with diameter of 8 cm. Inside there is a transformer made by three coils with three *N87* ferrite cores of dimensions $32 \times 16 \times 9$ mm and inductance $2.3 \mu\text{H}$ ([29]). The spire ratio between primary and secondary circuit of the transformer is 1/30. On one end of the head there is the driver circuit that receives an optical signal from the controller, that is the trigger signal for voltage pulse; on the other end there is the electrode. The driver circuit is connected to the primary circuit of the transformer, the electrode to the secondary circuit. When the controller sends the trigger signal, there is a voltage variation on primary circuit that produces the voltage pulse on the electrode.

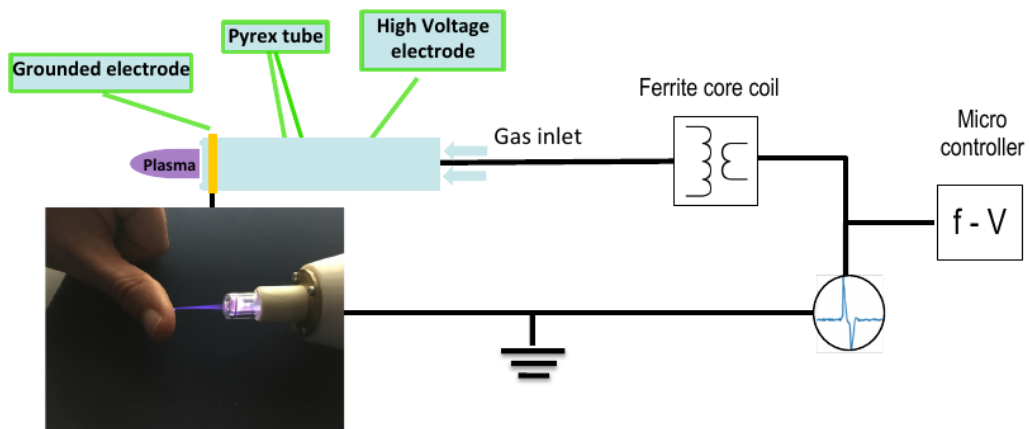


Figure 2.1: Scheme of the source. The micro-controller on the right sends a trigger signal to produce variable voltage on the coil mounted in the head, that produces an high voltage pulse on the electrode. The electric field ionizes the neutral gas and produces the plasma plume in the picture. The grounded ring around the nozzle is removable.



Figure 2.2: Picture of PCC source, prototype B. The black box on the left is the *Controller*, the cylinder on the right is the *Head* where plasma is produced.

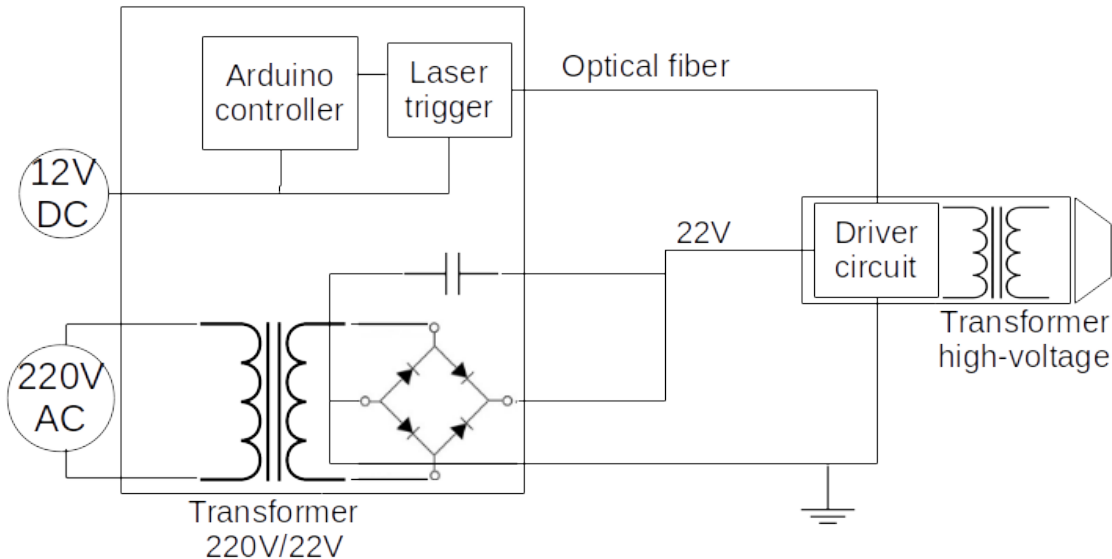


Figure 2.3: Electric scheme of the source. On the left there is the controller, on the right there is the head.

Controller and head are connected only with power cables for driver circuit and an optical fiber that sends the trigger for the voltage pulse.

Gas is inserted through a separated channel that goes from one end of the source to the other end near the electrode. The nozzle at the end of the head can be selected between different materials and shapes. For this study are used a plastic nozzle that expels plasma through a cylinder with diameter of 1 mm and a cylindrical glass nozzle that shrinks at the end, until a diameter of 5 mm.

Prototype **A** is the first version used during this work, prototype **B** is the latest one. Generally the second one is characterized by an higher ionization efficiency. Principal differences are:

- different geometries for the coils inside the head;
- prototype **B** has positive voltage pulse polarity while prototype **A** has negative voltage pulse polarity;
- **A** presents a problem of neutral gas diffusion in the area where there are the coils due to geometry problems of the prototype. For this reason other measurements (described in following chapters) are made only with prototype **B**.

2.2 Electric scheme

In this chapter development of PCC electric scheme is discussed and its output is characterized. To produce plasma as DBD, in air, with helium or argon as ignition gasses, it is necessary to apply high voltage difference in short distances, resulting in high electric field. It is common to produce electric fields with fast voltage pulses for various uses, including jet or DBD plasma production ([30], [31], [32]). The scheme that PCC uses outputs a voltage pulse with an amplitude from 1 kV to 10 kV and pulses repetition rates from 5 kHz to 60 kHz.

One representation of the electric scheme is in figure 2.3. As already explained, the circuit divides in two parts: the controller, with power task and voltage pulse settings, and the head, where plasma is produced.

Line divides in:

- **Power line** : the controller is connected to a 220 V AC (50 Hz) power line. This signal goes in

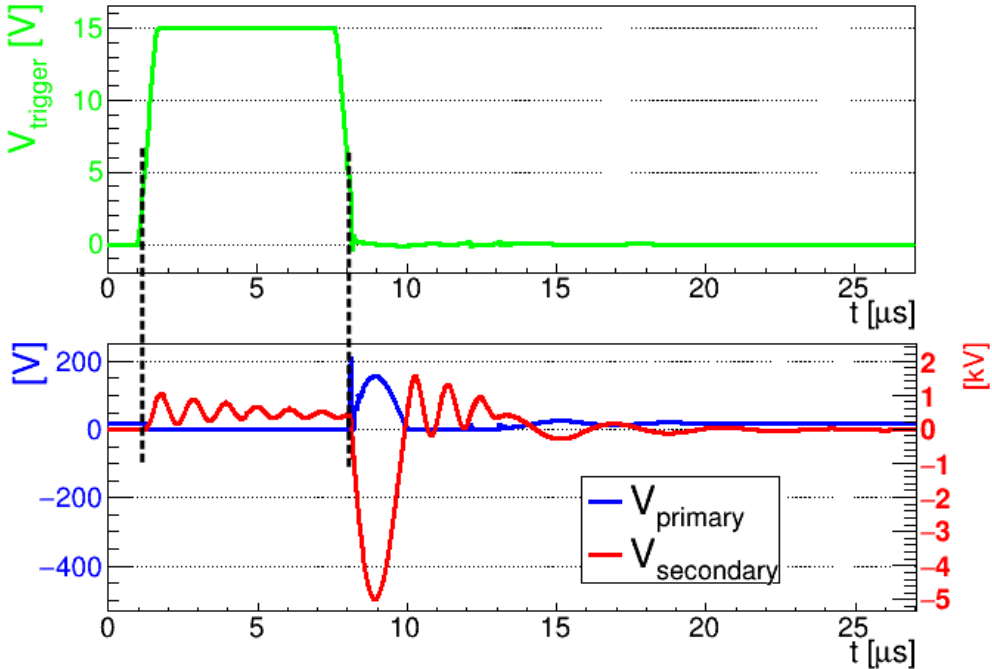


Figure 2.4: Simulation of signals on the components of the head. Top in green there is the PWM trigger signal; bottom in blue there is the voltage of primary circuit with values in volts, in red the voltage of secondary circuit with values in kilovolts.

a transformer that reduces voltage value and to a diode bridge that rectifies the signal, resulting in an output of 22 V DC. This voltage powers the Driver Circuit on the head.

- **Arduino and trigger :** Arduino and a laser are connected to a power line at 12 V. One of the Arduino analogical outputs sends a square wave (PWM) to the laser trigger, that transmits an optical signal with the same duration and pulse repetition rate of the PWM through an optical fiber. The fiber ends on a photodiode installed on the driver circuit that works as a switch to trigger the voltage pulse. With this setup pulse repetition rate and pulse amplitude are set by Arduino and the high voltage signal that circulate on the head is entirely decoupled from the controller. This setup was developed as a solution for reflection problems observed in the first PCC prototype.
- **Head :** on the driver circuit there are the photodiode, a capacitor and a MOSFET that works as a switch for conductive and charging phases of the circuit. When the photodiode measures the laser signal, voltage goes from power value to 0 and the capacitor starts charging. When the trigger signal ends, the voltage goes back to power value and the variation leads to a peak of thousands V on the output of the secondary circuit, connected to the electrode. Pulse repetition rate, f , is set precisely by the Arduino, PWM duration is set giving the opening time of the MOSFET, i.e. the duration of the charging time of the capacitor.

An example of voltage values on relevant components is presented in figure 2.4, obtained with a simplified scheme with Spice. Once the PWM trigger starts, voltage on the primary goes from power value to 0, after 6 μs the PWM signal ends, and the output of the secondary circuit shows a peak of -5000 V and width of 1.2 μs . A longer PWM implies a longer charging time and an higher voltage. Ultimately, amplitude of the pulse is proportional to the width of the PWM signal and source peak output V_p can be calibrated as a function of Δt for every pulse repetition rate f . It is necessary to note that when the charging phase ends, at the end of the PWM signal, there is a voltage peak also on primary circuit with amplitude of 150 V and several oscillations of the same amplitude on the secondary. Those could influence the output behavior if the pulse repetition rate is set too high, i.e. for values that would result in signal periods comparable to Δt .

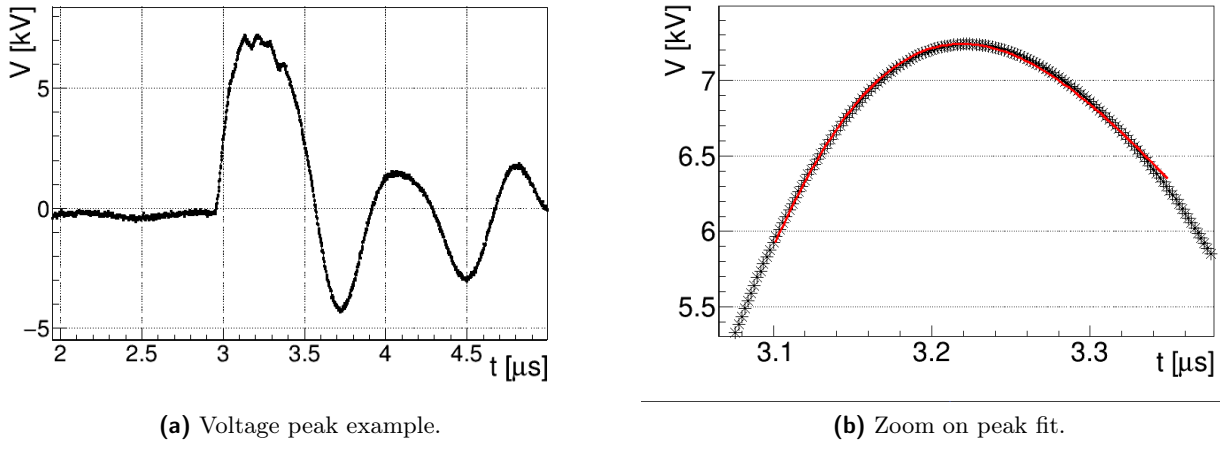


Figure 2.5: (a) Example of voltage measurements with prototype **B** for $f = 5 \text{ kHz}$ and $\Delta t = 4 \mu\text{s}$; (b) reconstructed signal after low pass filter and fit of the peak.

2.3 Output characterization

The electric field generated by the electrode defines plasma production and discharge features. It is studied the dependency of plasma behavior from voltage peak value and from pulse repetition rate, f . In addition, medical application of plasma requires low current intensity on target, in this study it's measured current intensity flowing on a copper sheet targeted by the plasma plume at a certain distance. Ultimately the different parameters for the measures are: Δt , opening time of the MOSFET in the circuit that is proportional to voltage peak value, and f , pulse repetition rate.

Voltage signals are measured with a voltage probe (*hv probe*) built for high voltage measurements *Tektronix P6015A*, with an attenuation factor $\times 1000$. The voltage output from secondary circuit is taken right before the connection between secondary circuit and electrode. Current signal are measured with *Tektronix CT2* current probe for current measurements. This probe have an output of 1 mV for a current of 1 mA. An oscilloscope *Yokogawa DL9040* allows to observe both signals and to store the total measured waveform.

First measurements are taken without gas flow to characterize output voltage of the circuit. After those an helium flow of 2 L/min is inserted in the head, to measure the output in presence of plasma. For both conditions the output is observed changing Δt and for different repetition rate f . The average current intensity over a time period, i.e. an effective current intensity I_{eff} , is also observed to evaluate plasma application's effects over a longer time period.

Every lenght measure is done with a decimal caliper, that gives a measurement uncertainty of 0.1 mm.

2.3.1 Measurements without gas

With a set repetition rate f voltage signal is measured for different values of the opening time Δt in the operational range. To assure that a voltage pulse ends before another starts, this range is different for different f : if there are more pulses in a given time and take into consideration pulse oscillations, the range of possible Δt is smaller for higher rates. A typical voltage waveform is in figure 2.5 (a). The scope of those measurements is to verify proportionality between amplitude of the peak, V_p , and Δt , for different f . Signals are analyzed with a low-pass filter where their Fourier Power Spectrum is evaluated (using ROOT C++ libraries [33]) and the signal reconstructed without higher frequencies, to exclude noise fluctuations. The reconstructed peak is an asymmetric function in time as in figure 2.5 (b). It is possible to fit the signal with a Landau function [34] and obtain peak value and position. The error on the measure is evaluated adding contributes from the low-pass filter.

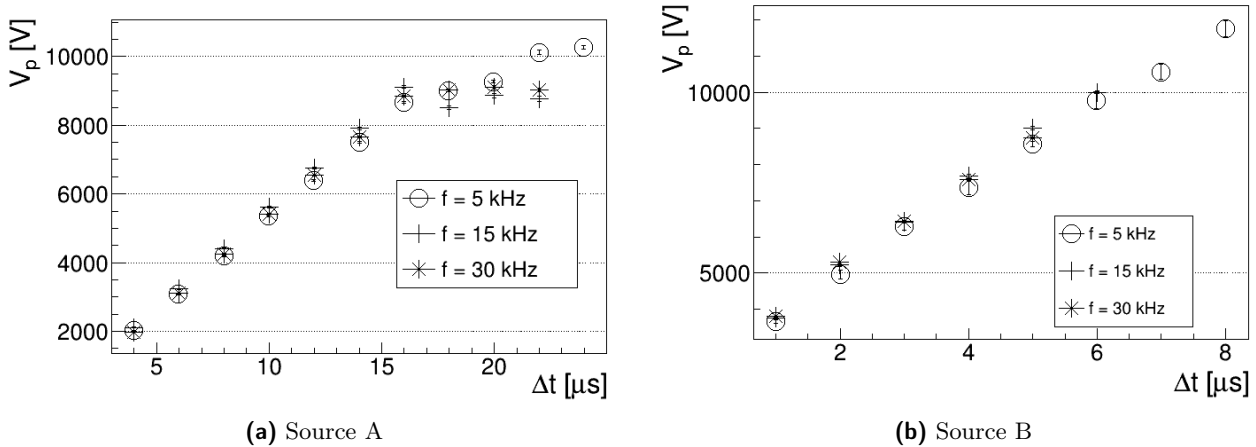


Figure 2.6: Absolute voltage peak values of secondary circuit output in function of Δt at different f , for both prototypes. Voltage peaks show linear behavior for $V_p \leq 10\text{ kV}$.

Results are shown in figure 2.6 for prototype **A** and **B**. For **A** there is a linear behavior for $4 \leq \Delta t \leq 16 \mu\text{s}$, with peak values from 2.02 ± 0.01 to $9.25 \pm 0.05 \text{ kV}$; for larger Δt the relation is not linear. The upper limit on Δt is given by the need of a minimum time interval between two pulses. Also for **B** there is a linear behavior, but with higher values: for $1 \leq \Delta t \leq 8 \mu\text{s}$ voltage peak goes from 3.66 ± 0.06 to $11.76 \pm 0.22 \text{ kV}$. With this source the upper limit for Δt is chosen considering the maximum voltage value sustainable by the dielectric. To avoid the risk of dielectric breakdown the maximum opening time for prototype **B** is set at $\Delta t = 8 \mu\text{s}$.

Voltage output doesn't show significative differences changing repetition rate. To confirm this observation measures are interpolated with a linear function in the range $0 - 16 \mu\text{s}$ for **A** and range $0 - 8 \mu\text{s}$ for **B**. Parameters resulting from the fit are compared as in figure 2.7. Values are displaced with random distances from the mean value, so it can be concluded that the behavior is not defined by the repetition rate.

2.3.2 Measurements with gas

Helium gas with a flow of 2 L/min is introduced at the end of the head, near the electrode, to produce plasma in DBD conditions. Measurements are repeated as before to study how voltage value changes with plasma introduction. A conductive target is placed in front of the source to measure the intensity of current carried by plasma. To assure safety of plasma application large current intensities and the possibility of arc formation needs to be avoided. Studies of conditions for DBD discharges and arc transitions ([35], [36], [37]) suggests that for fast pulses it's safe to have current intensity < 10 mA.

Current intensity is measured with a copper sheet of dimensions $10\text{ mm} \times 10\text{ mm} \times 1\text{ mm}$. The plasma plume impacts on the sheet that is connected to the current robe that converts the signal in a voltage measurements that the oscilloscope can measure. Due to low current intensities it is necessary to pay attention to cables shielding, decreasing noise. The relation between current intensity and target distance is studied in [28]. In this work the distance between target and electrode is chosen around typical values for treatments: 10 mm for prototype **A** and 15 mm for prototype **B**.

In figure 2.8 is presented a measure for $\Delta t = 8 \mu\text{s}$ and $f = 5 \text{ kHz}$ with prototype **B**. For both sources there is a current peak in correspondence of voltage pulse, that increases with voltage.

Data analysis is the same described before, for both voltage and current values. Results are shown in figures 2.9 and 2.10, measurements where the current peak is not distinguishable from noise are excluded from plots.

Voltage peaks are lower than values without gas. It is an expected behavior if the plume is considered

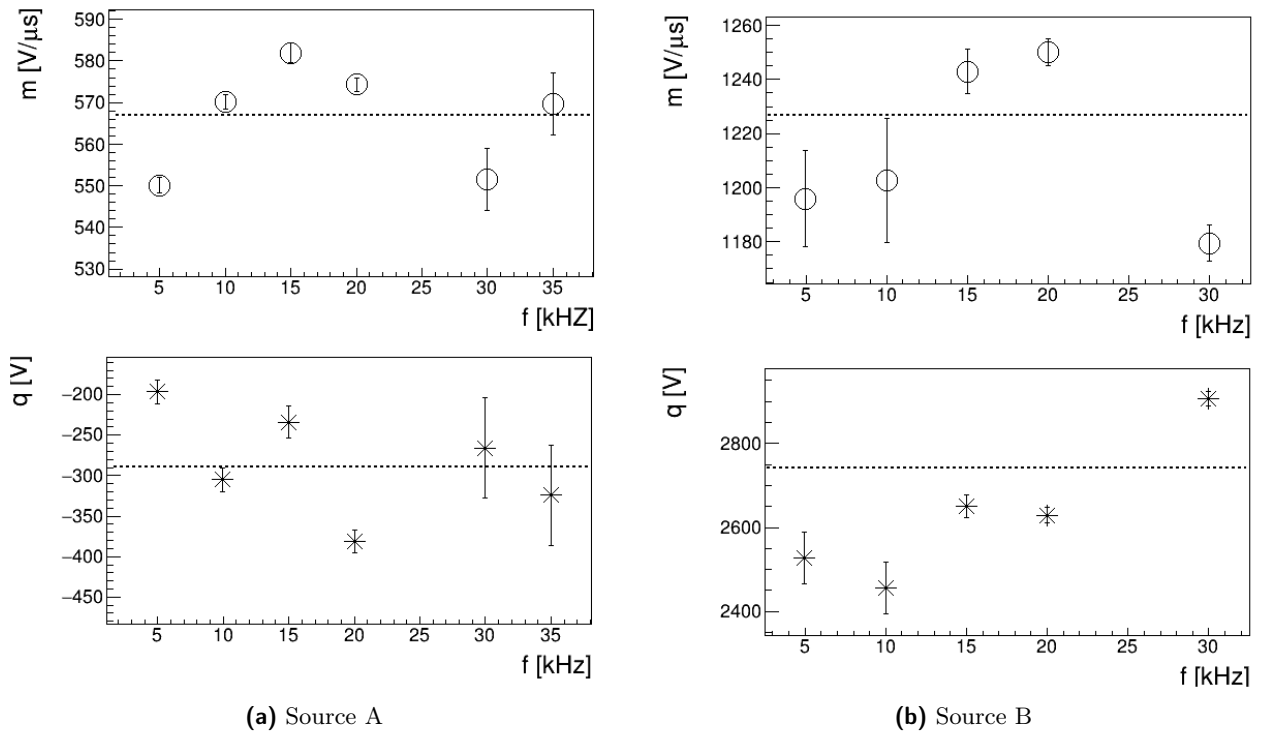


Figure 2.7: Resulting parameters from the linear fit of voltage values as a function of opening time without plasma, for different repetition rates, for both prototypes. Voltage peaks are interpolated with a linear function $V_{peak} = m\Delta t + q$, in figure there are slopes m on top and intercepts q on bottom. Dashed line is the average value of the parameter. There isn't a specific behavior in parameters, is possible to conclude that output voltage does not depend on pulse repetition rate.

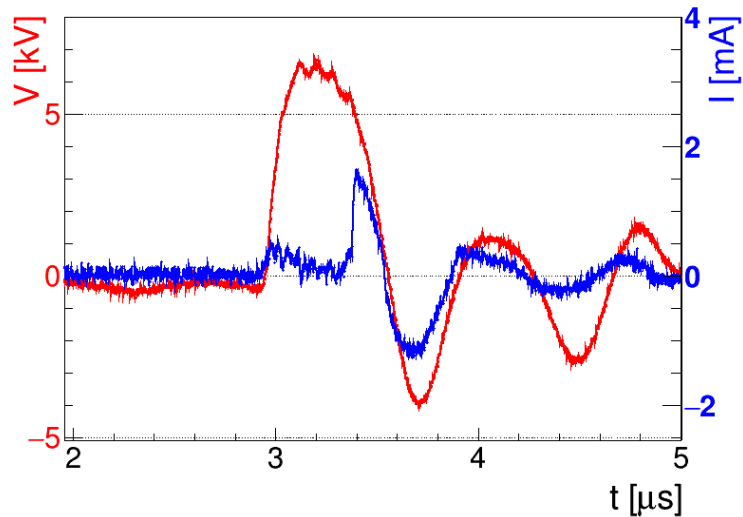


Figure 2.8: Voltage output (red) and current measurements (blue) for a discharge with prototype **B**, $f = 5$ kHz and $\Delta t = 3$ μ s

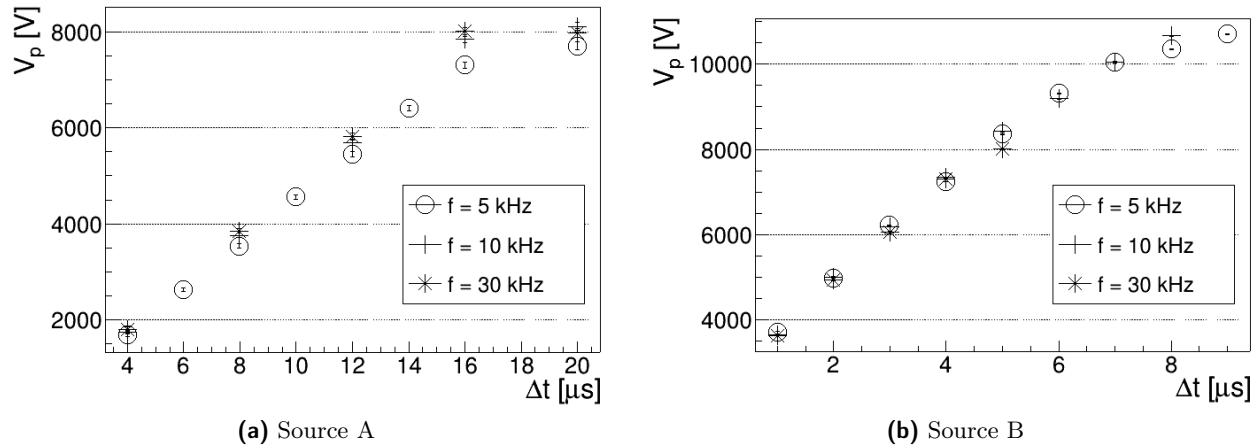


Figure 2.9: Absolute voltage peak values of secondary circuit as a function of Δt at different f , with an helium flux of 2 L/min, for both sources.

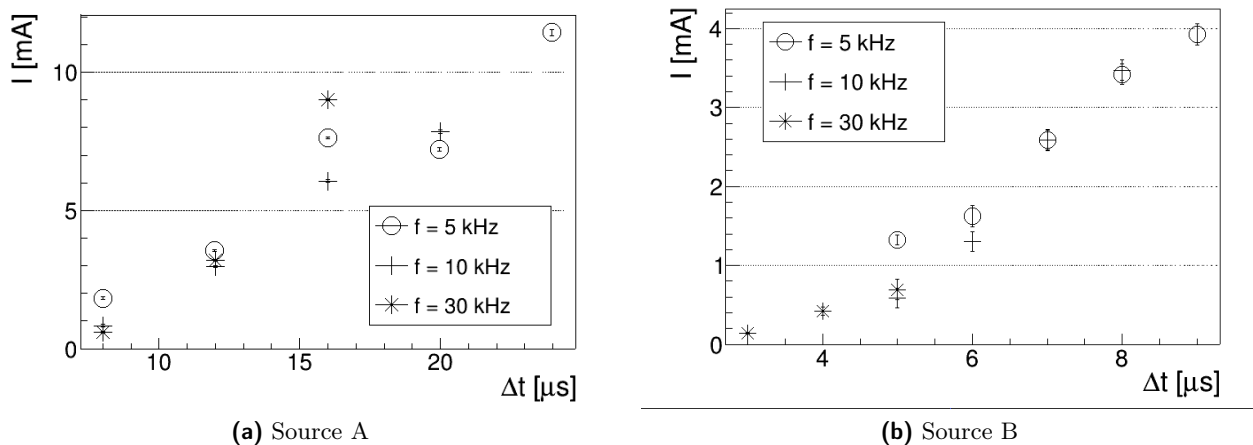


Figure 2.10: Absolute current peak values measured with helium flux of 2 L/min, on a copper target, as a function of Δt at different f , for both sources.

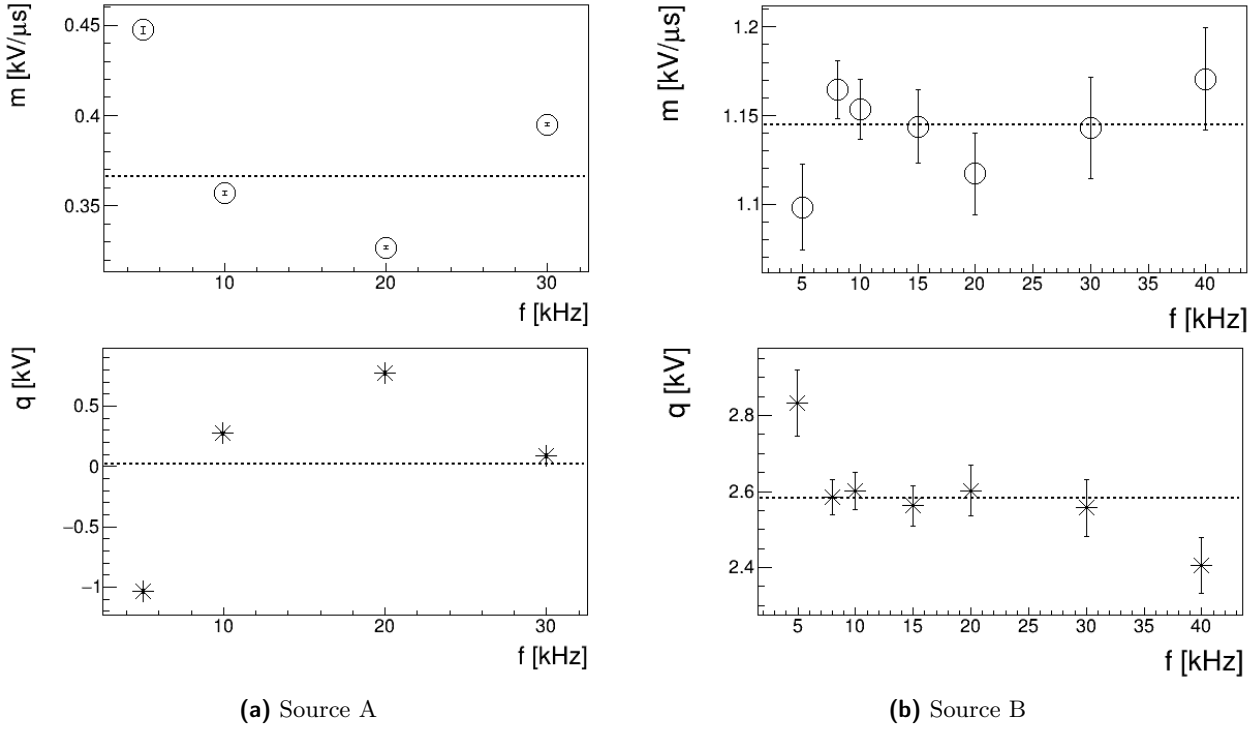


Figure 2.11: Resulting parameters from the linear fit of voltage values as a function of opening time in presence of plasma, for different repetition rates, for both prototypes. Voltage peaks are interpolated with a linear function $V_{peak} = m\Delta t + q$, in figure there are slopes m on top and intercepts q on bottom. Dashed line is the average value of the parameter. Also with plasma there is not a specific behavior in parameters. It is possible to conclude that output voltage does not depend on pulse repetition rate.

as an additional resistive load at the end of the circuit [38]. Also for this measurements there is a linear dependency between voltage and Δt for $V_p \leq 10$ kV. Linear fit parameters are again compared for different f . Current intensities increase as voltage and are higher for prototype **A**, as expected given different distances electrode-target. Analysis of linearity also for those measures can show if there is a different behavior changing pulse repetition rate. Figures 2.11 and 2.12 shows results of the linearity study for different pulse rates.

For voltage fit parameters are scattered around their average value for both sources, confirming the hypothesis that voltage growth is independent from pulse repetition rates. For prototype **A** the voltage average increase is $m_V = 0.366 \pm 0.001$ kV/μs, for prototype **B** is $m_V = 1.145 \pm 0.008$ kV/μs, higher, as explained before.

Current values shows a different behavior: in prototype **A** there are increasing parameters with increasing repetition rates, in prototype **B** data are more scattered and it is not possible to extrapolate a behavior. Despite this behavior the slope is in the same range of values for both prototypes, with a maximum for **A** of $m_I = 1.10 \pm 0.01$ mA/μs and for **B** of $m_I = 1.04 \pm 0.17$ mA/μs.

The parameter trend in prototype **A** could suggest a variation of reaction parameters happening inside the plasma. If with higher repetition rate there are more ionization reactions, there would be higher charge densities and higher measured current intensity. Due to low signal to noise ratio in measures for prototype **B**, it is not possible to esclude a relation between current slope and repetition rate for this source, however it is established a maximum limit value to take into consideration when using the device.

Time intervals From voltage and current waveforms it is possible to extrapolate informations on time width of those signals. They can be defined as the FWHM of measured peaks, evaluated as

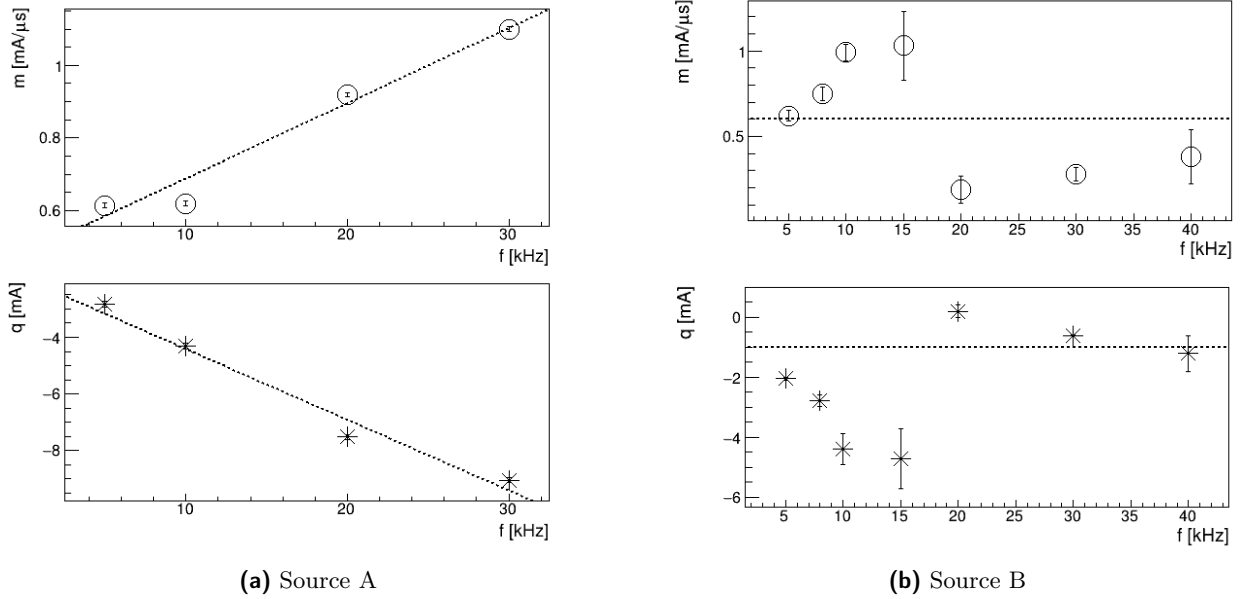


Figure 2.12: Resulting parameters from the linear fit of current values as a function of opening time, for different repetition rates, for both prototypes. Current peaks are interpolated with a linear function $I_{peak} = m\Delta t + q$, in figure there are slopes m on top and intercepts q on bottom. Dashed line is the average value of the parameter. For prototype **A** there is a linear dependency from f , in dashes in the figure. For prototype **B** it is not possible to extrapolate a behaviour.

the time when we measure half of tension or current maximum value. As the characterization of the sources shows an almost equal behavior, this study is made only for prototype **B**, that is the only one used in the following chapters. Results are shown in figure 3.6. For every repetition rate there is a quadratic behavior of voltage widths with a minimum for a $\Delta t = 5 \mu s$. It is possible to give an estimation of pulse width with a mean value between this minimum and maximum values obtained for $\Delta t = 1 \mu s$, it is $T_V = 963 \pm 15 \text{ ns}$. For currents, widths have great uncertainty where the peak is low, but it is possible to evaluate a mean value for $\Delta t \geq 6 \mu s$, and it is $T_I = 968 \pm 28 \text{ ns}$. Values from the two measurements are compatible and they are a good estimation of pulse time duration.

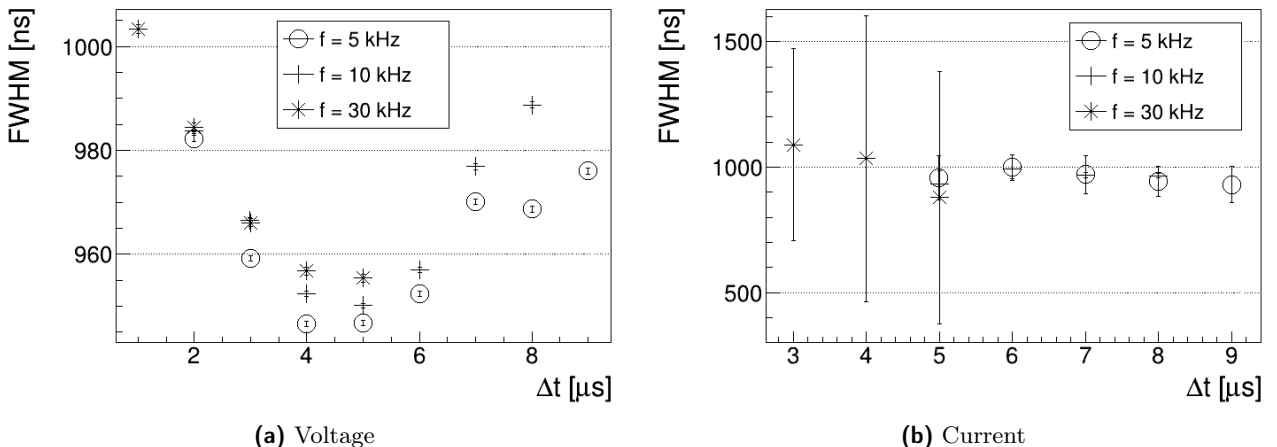


Figure 2.13: FWHM of voltage and current pulses varying opening time, for different pulse repetition rates.

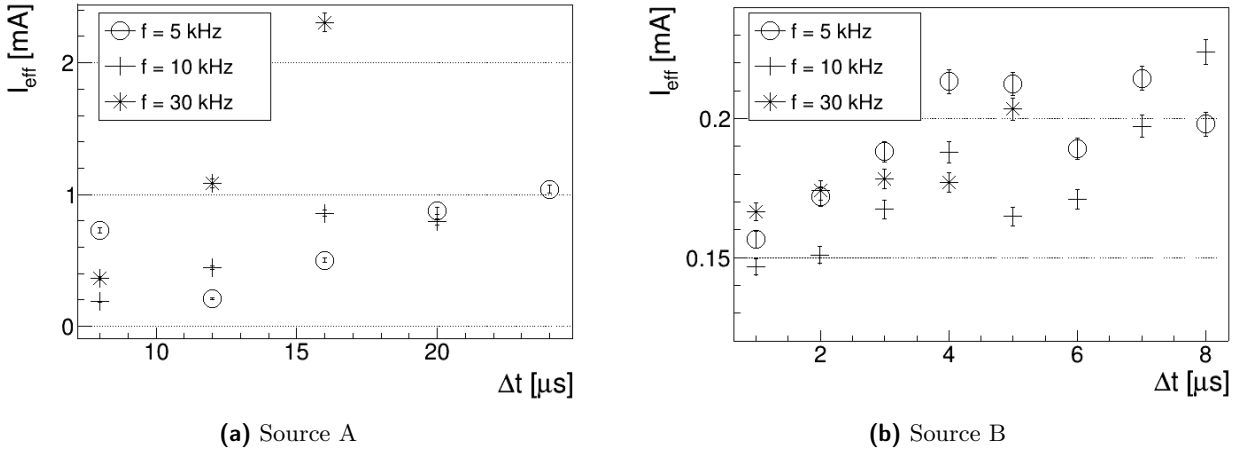


Figure 2.14: Effective current values measured for a time interval of 1 ms as a function of Δt , for different repetition rates, for both sources.

2.3.3 Effective current

Current effects in applications on biological tissues have to take into consideration current intensity in a time interval typically larger than the pulse widths used in our sources ([39], [28]). It's possible to estimate an effective current that is more appropriate to take into consideration when evaluating damage due to currents, as a mean of current intensity in a defined time interval calculated with equation 2.1, taking $t_2 - t_1 = 1 \text{ ms}$. The effective current takes into consideration that current values are very small for all the time between two pulses.

$$I_{\text{eff}} = \sqrt{\frac{1}{(t_2 - t_1)} \int_{t_1}^{t_2} I^2 dt} \quad (2.1)$$

Figure 2.14 shows effective currents measured for both sources. Values are significantly smaller than maximum peak values, especially for prototype **B** where oscillations after the main peak are smaller. The maximum value for the two prototypes is given by $I_{\text{effA}} = 2.47 \pm 0.07 \text{ mA}$ and $I_{\text{effB}} = 0.23 \pm 0.01 \text{ mA}$.

2.3.4 Plasma impedance estimate

From voltage and current measurements can be extrapolated plasma's electric behavior. In this subsection plasma impedance is estimated with measurements from prototype **B**. Voltage output from head's transformer can be modeled as a damped sine wave around the peak, as in equation 2.2, where V_{pulse} is the amplitude of the undamped pulse, τ is the characteristic damping time and f_{V_s} is the explicit parametrization of the frequency of the single pulse that we observe on measurements.

$$V_S = V_0 + V_{\text{pulse}} \sin(2\pi f_{V_s} t) e^{-t/\tau} \quad (2.2)$$

It's possible to study how plasma impedance changes for different frequency pulse f_{V_s} to understand its electric behavior. Frequency pulse is different for each opening time of the circuit, Δt , but it is constant when changing pulse repetition rate, as explained before analyzing voltage outputs. In figure 2.15 there is an example of a peak interpolated with the function in formula 2.2 while in figure 2.16 there are the resulting fit parameters for different Δt .

With higher opening times V_{pulse} is higher as expected, while f_{V_s} and τ have their own behaviors that depends from V_s . To estimate plasma's impedance it's useful to observe that voltage peak is quite large in time: it varies of less than 3% of peak's value in an interval of 150 ns around it. As voltage

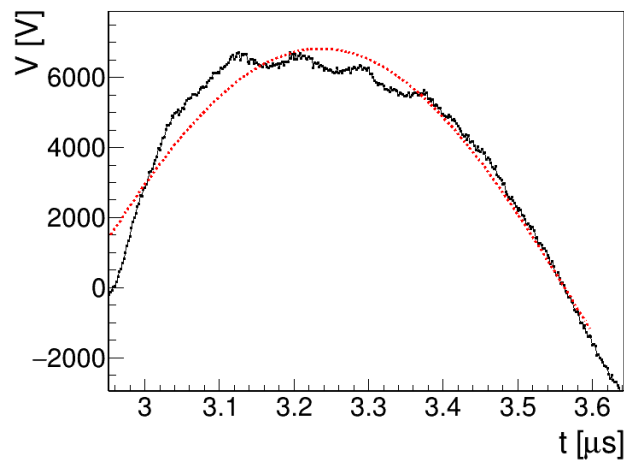


Figure 2.15: Example of a fit of voltage measurements with function 2.2.

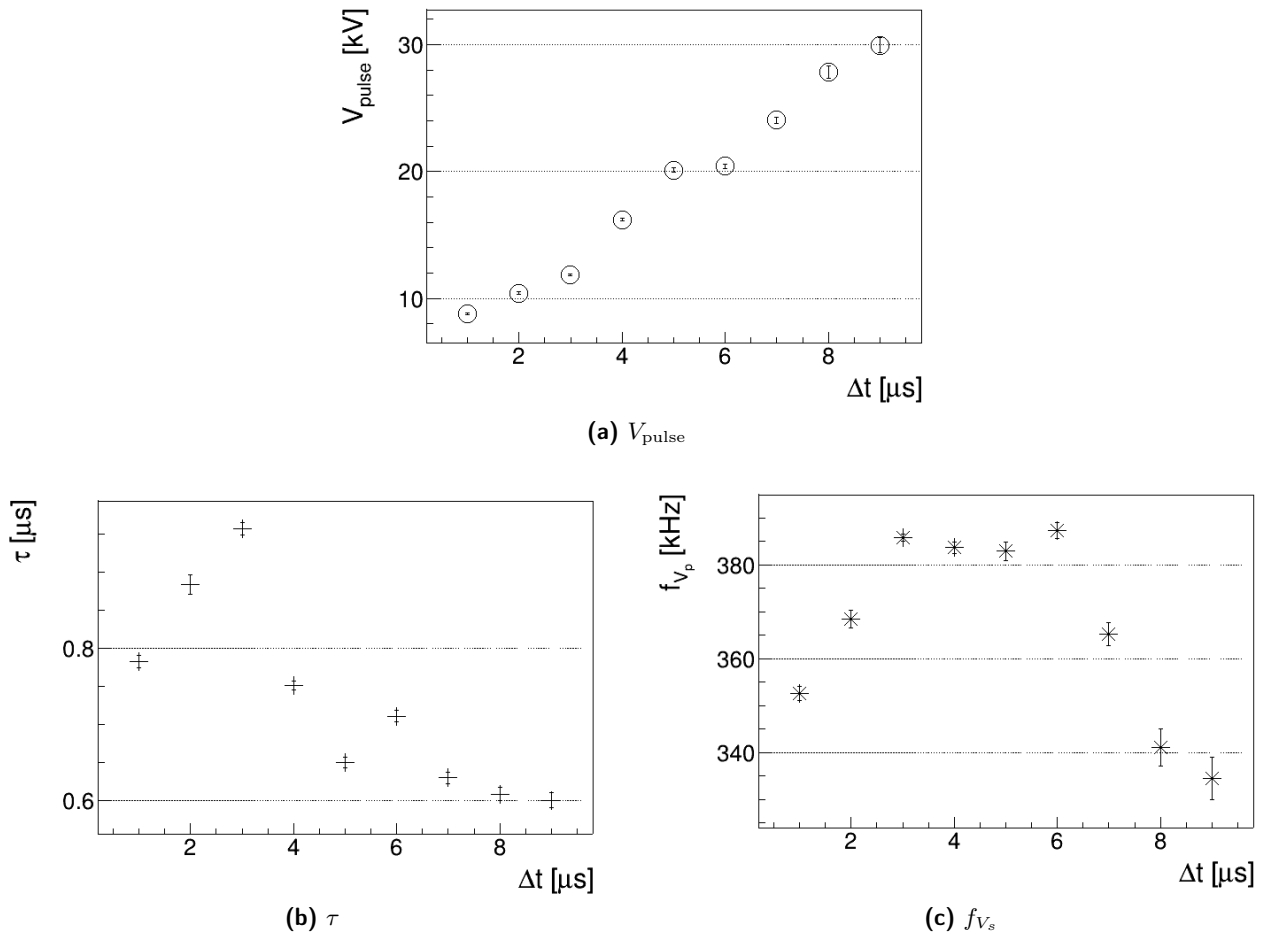


Figure 2.16: Resulting parameters from the interpolation of measurements with a dumped sin, as in equation 2.2, for pulses with $f = 8$ kHz and different Δt .

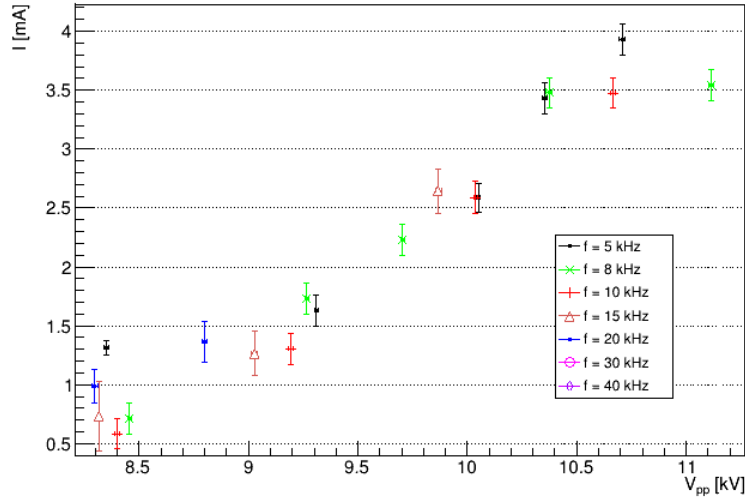


Figure 2.17: Voltage peak values against current peak values for different f .

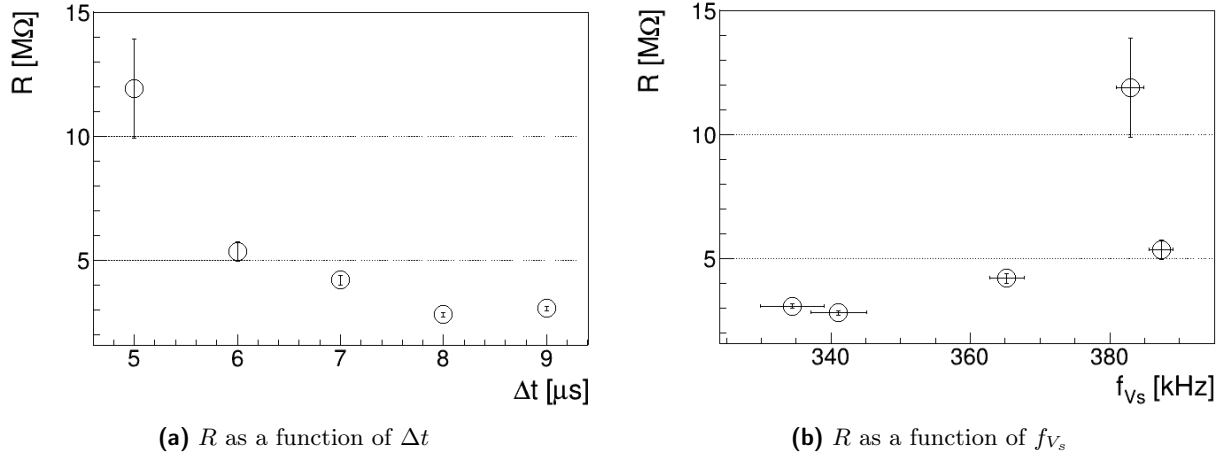


Figure 2.18: Plasma resistance for different opening times (a) corresponding to different frequencies fit parameter (b).

and current peak times differ always by a time interval $|t_{V_p} - t_{I_p}| \leq 150\text{ ns}$, it is possible to assume $V_{t_{I_p}} \simeq V(t_{V_p})$, i.e. that voltage during the current peak maximum is equal to voltage peak value. With this approximation, voltage peak values can be studied as a function of current peak value, as in figure 2.17. An estimation of average plasma resistance is the slope resulting from a linear fit or it is possible to estimate the resistance as $R = \frac{V_p}{I_p}$ for a particular Δt . Results are shown in figure 2.18, changing opening times and changing frequency of single pulse f_{V_s} .

From the graphs it's possible to extrapolate that plasma resistance goes from $2.98 \pm 0.11\text{ M}\Omega$ to $11.82 \pm 2.19\text{ M}\Omega$, with near constant values in the range of opening times $7 - 9\text{ }\mu\text{s}$. From a deeper analysis and specific measures it could be possible to expand the analysis here presented and estimate plasma's electrical capacitance or inductance.

Chapter 3

Plasma dynamics

PCC expels a column shaped plasma plume that emits radiation in a visible range, with different colour and intensity for different gas composition, gas flow and intensity of electric field. In figure 3.1 there are pictures of plasma plume with different gas used to start the discharge.

Recent studies shows that what is expelled is not a continuos flow, but the plume is formed by compact collections of emitting particles called *bullets*. Those bullets forms in coincidence of voltage pulses and propagates in air with velocities from 10 to over 150 km/s ([40], [41]).

An example of this phenomenon measured with the experimental apparatus used in thesis is shown in figure 3.2.

Plasma bullets still needs to be studied in depth, at today are known the basic dynamic of formation and expulsion. Some general features are that:

- bullets velocities are $> 10 \text{ km/s}$;
- bullet formation, it's velocity and it's travel distance depend on applied voltage on the electrode.

The scope of this experiment is to observe plasma bullets produced by our source, their shape and their velocity and how they change with different discharge conditions.

Given their typical velocities and the temperature of the plasma, bullet propagation is tought to be related to a travelling ionization front. This propagation can be studied with simplified simulation of DBD discharges, where it's reproduced the behaviour of plasma bullets ([42], [43]) or the interaction between plasma and a target ([44]). Possible explanations for bullet propagation are analyzed at the end of this chapter, with estimates of electron temperature and electron mobility that give better insight on the phenomenology.

3.1 Experimental setup

To visually observe dynamics of plasma formation and propagation with enough resolution, it is needed an acquisition setup with a fast camera that has short integration time, below 20 ns, and an image intensifier that allows to visualize light emitted in such a short time interval.

To guarantee synchrony between plasma discharge and frame acquisition it is necessary to consider instruments and plasma source specific delays and give appropriate triggers.

Experimental setup is shown in figure 3.3 and a scheme is presented in 3.4. In the scheme there are the voltage signal lines that trigger the discharge and the acquisition, the optical acquisition apparatus pointed at source exit and the measurements acquisition instruments that are a computer and an oscilloscope.

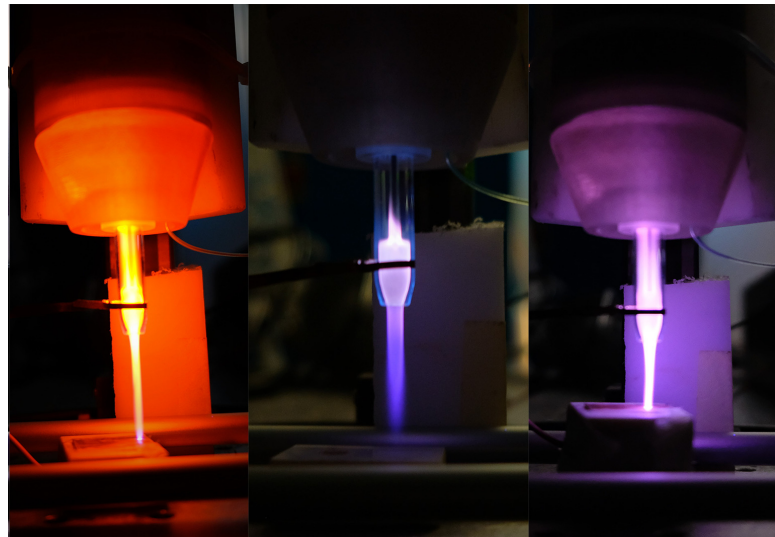


Figure 3.1: Plasma plume pictures with different gasses used to start the discharge: neon on the left, argon in center and helium on the right. The source points to a conductive target positioned in front of the nozzle, after 22 mm for neon and argon, after 14 mm for helium.

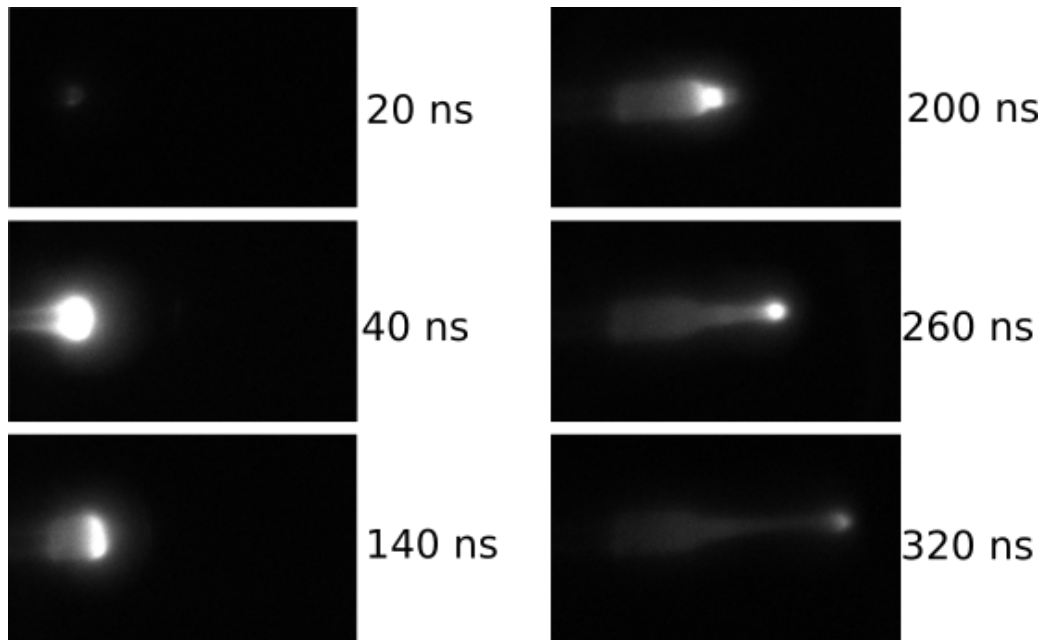


Figure 3.2: Example of helium plasma bullet expulsion, as measured with our experimental setup. The single frames are taken with a fast camera with integration time of 15 μ s.

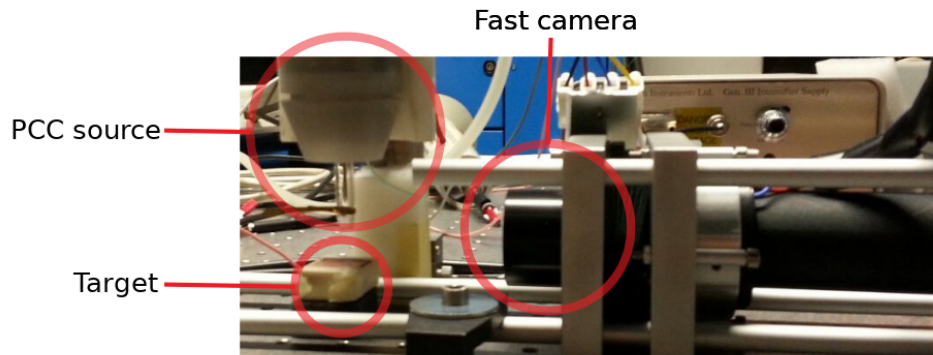


Figure 3.3: Picture of the experimental setup. The source PCC is mounted vertically and points to a removable target that can be positioned at different heights. Plasma is observed with a fast camera from the side.

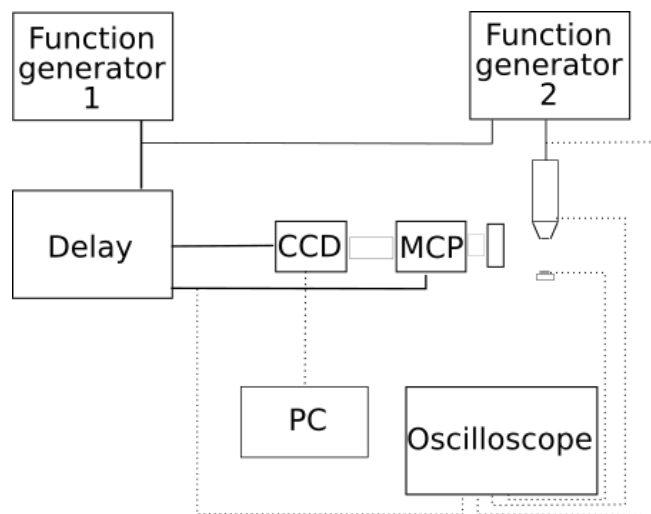


Figure 3.4: Experimental setup scheme. Function generator 1, function generator 2 and delay generator send trigger signal to camera (CCD), to source and to image intensifier (MCP), full lines in the scheme. Camera sends measured frames to a computer (PC). From source, source's target, function generator 2 and delay are taken signals read on the oscilloscope, pointed lines in the scheme.

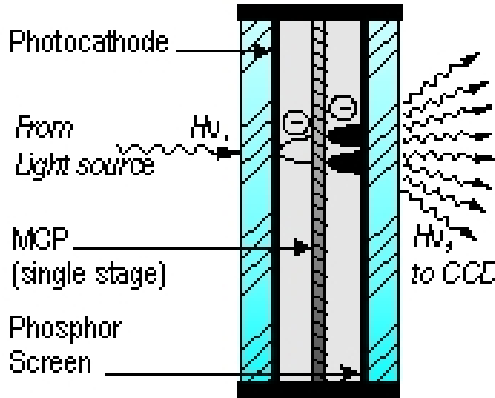


Figure 3.5: Micro Channel Plate image intensifier functioning.

Optical apparatus is composed by a lens coupled with a Micro Channel Plate image intensifier (MCP). An MCP works as in figure 3.5: for every photon received it emits many photons with little angular deviation.

Those photons are received by an high-speed camera *Point Grey Flea* [45] equipped with a CCD of 1024×768 square pixels $4.75 \mu\text{m}$ wide. Every frame is sent to the pc where FLIR software elaborates and saves them in pgm format [46].

3.1.1 Source, power lines and electric signals

The source utilized is the latest prototype, **B** in chapter 2. It has a voltage pulse peak value between 3 and 10 kV, regulated by the lenght of the trigger signal Δt (see chapter 2). To synchronize measurements and discharge a generator function gives the trigger signal (generator 2 in the scheme) instead of the usual controller module of the source.

The source is positioned vertically at a distance of 42.0 ± 0.1 mm from optical bench, with the glass nozzle that allows to observe plasma formation inside it (external diameter 8.0 ± 0.1 mm, internal diameter 6.0 ± 0.1 mm). The distance from the end of the electrode and nozzle exit is 12 mm. At the exit the nozzle shrinks for 3.0 ± 0.1 mm, until a diameter of 5.0 ± 0.1 mm

Under the source is possible to position targets. Two different targets are used at different heights: a conductive target and an insulating target. The first one is a copper square sheet of dimensions $10 \text{ mm} \times 10 \text{ mm} \times 1 \text{ mm}$ (used for current measures in chapter 2), the second one is a plastic material.

CCD camera is powered by a common voltage supply, while image intensifier MCP is powered by an high voltage supply. A delay generator triggers both instruments, with different delay times (see next section).

The oscilloscope *Yokogawa DL9040*, utilized in chapter 2, reads on different channels the trigger signal given to source head, the trigger signal given to MPC, the voltage electrode with high-voltage probe *Tektronix P6015A* and the current intensity when it's used the conductive target. Measurements of current intensity are done by a voltage probe with attenuation $\times 10$ that measures the voltage drop on a resistance of $1 \text{ M}\Omega$ connected to the conductive target.

3.1.2 Trigger synchronization

Experiment's objective is to observe plasma formation and propagation in synchronization with the measurement of voltage on the electrode, so it's necessary to know precisely discharge and measure times.

The trigger lines is composed by:

- function generator *Or-x 310*, 1 in figure, that sends a square pulse with set amplitude and width, with pulse repetition rate f ;
- function generator *Lecroy 9210*, 2 in figure, that sends a square wave with repetition rate given by the trigger, with constant amplitude and variable width Δt ;
- delay time generator *Stanford DG535*, that sends a square wave with constant amplitude and repetition rate given by the voltage input. Start time of this signal is given by input starting time plus settable delays (4 different channels).

Every measuring instrument has it's own time delay between trigger signal and effective measure. The higher delay is the arming time for fast camera, in the order of ms, the shortest one is the integration time for acquisition system, that starts from the activation of the image intensifier and span 15 ns.

A time line is shown in figure 3.6, an example of signals taken with the oscilloscope is in figure 3.7. There are three relevant times defined by function and delay generators:

1. t_0 is the starting time for the square pulse given by *Function generator 1*, with an amplitude of 5 V and repetition rate f . The pulse is the external trigger for *Function generator 2* and the voltage input of *Delay generator*. The square wave that triggers the voltage pulse on the source starts at t_0 from *Function generator 2*; it has a time width of Δt that defines voltage amplitude (see chapter 2) and repetition rate f . The trigger signal that arms the camera starts at t_0 from *Delay generator*.
2. t_{DIS} is the effective discharge starting time, when the voltage peak starts. From trigger signal end to voltage peak start there is a time delay given mainly by the response time of the photodiode on source head. Measuring the signals as in figure 3.7, it's possible to estimate this delay as 987.7 ± 56.7 ns, constant for every f and Δt . The discharge happens after t_{DIS} , measurement times must be inside the grey zone in the scheme.
3. t_{MIS} is the measurement time, when MCP is triggered on. *Delay generator* gives the delay between t_0 and t_{MIS} , called t_D , with possible steps of 1 ps. Changing t_D it's possible to see plasma dynamics at different times that corresponds to different electrode voltage values, as in figure 3.7.

Integration time for a single frame is 15 ns, so the time step between two measures has to be larger than it. Time steps chosen are 20 ns for high resolution measurements, 50 ns for standard measurements.

It's important to point out that pulse repetition rates are $f \geq 1$ kHz corresponding to a time interval between two pulses lower than 1 ms; while the measure interval time between the acquisition of two frames is larger than 50 ms because of the camera. It is not possible to see two consecutive times for the same discharge, the frames are always measures of different discharges.

Each pixel on the CCD has a minimum and maximum intensity value, is possible to maintain the measure on the wanted level changing the settings on camera acquisition software. One of the parameters is the *Shutter time*, the opening time of the camera shutter. If the emission intensity is too low we can set the shutter time larger than the time between two acquisition, to acquire a frame that is the sum of two discharge. Another parameter is the *Gain* value, that amplifies or reduces the output. For each used gas we select an appropriate *Gain* value and an appropriate *Shutter time*.

3.1.3 Different setups

Many parameters have an effect on plasma formation: voltage pulse repetition rate, voltage rise time, voltage peak value, gas type, gas flow, presence of a target and its features (see [40], [47]). This study presents different setups with three different gasses, as shown in table 3.1. There is a lower limit value for pulse repetition rate, different for each gas, under which there is no discharge. The electric behavior

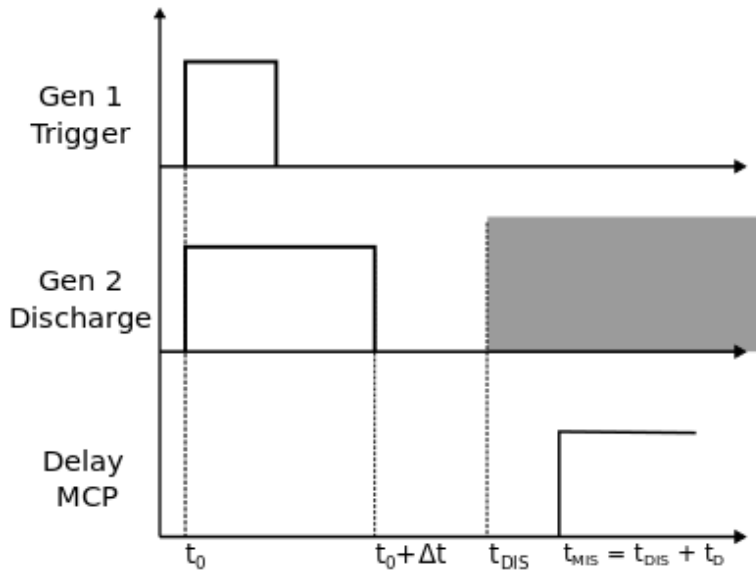


Figure 3.6: Time signal synchronization scheme: t_0 is the starting trigger time, Δt is the opening time for plasma source (see chapter 2), t_{DIS} is the starting time for the discharge and t_{MIS} the starting time for the MCP i.e. the measure time

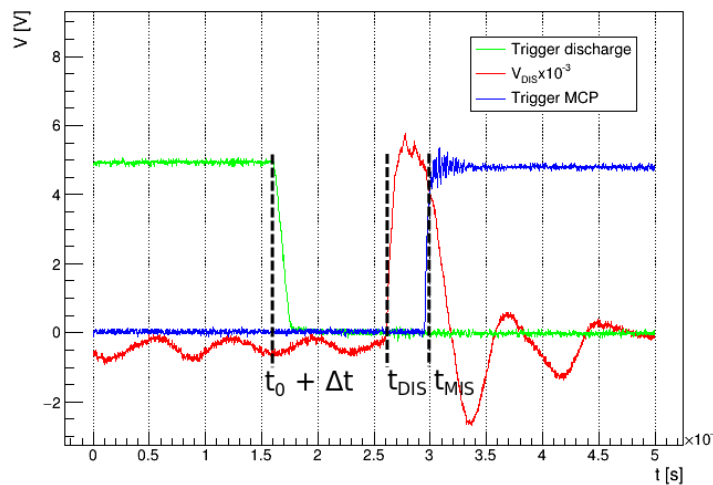


Figure 3.7: Example of oscilloscope measure. In green the discharge trigger, in red the electrode voltage output and in blue the MCP trigger. The dashed lines indicate times described in 3.6.

Gas	Setup	Δt [μs]	Target	Target position [mm]	Flow rate [L/min]	Other	Δt_D [ns]
He	A	3, 3.5, 4	-	-	2	-	20
	B	3.5	-	-	1	-	20
	C	3.5	-	-	3	-	20
	D	3.5	-	-	4	-	20
	E	3, 3.5, 4	Insulator	24	2	-	20
	F	3, 3.5, 4	Conductor	32	2	-	20
	G	3, 3.5, 4	Conductor	24	2	-	20
Ne	A	2, 2.5, 3	Insulator	24	2	-	50
	B	2, 2.5, 3	Conductor	32	2	-	50
	C	2, 2.5, 3	Conductor	24	2	-	50
	D	2, 2.5, 3	-	-	2	-	50
Ar	A	3.5	-	-	2	Grounded ring	50
	B	3.5	-	-	2	-	50
	C	3.5	Conductor	20	2	Grounded ring	50
	D	3.5	Conductor	20	2	-	50

Table 3.1: Description of measurement setups. In first column there is the gas; second column is the setup name; third column is voltage pulse time width; four and fifth columns are target information, if it's used a target; sixth column is gas flow; seventh column are other informations, e.g. if it's positioned a grounded ring around the nozzle; eight column is the time step between acquisitions.

of the source is the same for values higher than this threshold (see chapter 2). For each gas is chosen a repetition rate value that allows the discharge to start.

Gasses with different composition will have different ionization reactions and will produce different reactive species, with different masses and ionization energies. With this study is possible to observe how peak voltage value, gas type and gas flow determine plasma bullet formation and affect its expulsion velocity.

A conductive target near plasma exit at ground potential will modify the electric field produced by the electrode. With this study is possible to observe how the target affects bullet expulsion and propagation. Furthermore the bullet can hit the target, introducing into reactions balance also the electrons on the target.

When argon is the neutral gas used to start the discharge a grounded conductive ring can be placed around the nozzle after the electrode, to help the start of the discharge.

3.1.4 Frame analysis and calibration

Once a measure setup is chosen, the first acquisition is set around the start of the discharge. On the oscilloscope is saved the signal waveform for every channel (setup as explained before), on the computer 5 frames for every t_D are saved. Measures are taken with steps of Δt_D until it is not possible to observe plasma anymore.

Measure time from the start of the discharge can be evaluated from waveforms on the oscilloscope.

Frame analysis is done converting the pgm files in 2-dimensional histograms, with *TH2* class written in *ROOT* libraries (see [48]).

From the five frames taken it is evaluated the average value for each pixel. From the resulting frame

the plasma bullet is isolated as the collection of pixels with maximum intensity in the frame. The estimation of the bullet position is given by the coordinates of its luminosity barycenter on the plane seen by camera, called x-y in the analysis. Once established the center, the points were luminosity goes under a certain percentage of the maximum define its contour. Bullet dimensions along x and y axis are evaluated from the contour, while average luminosity is given by pixel values inside the contour. With barycenter coordinates it's possible to compute bullet velocity using a finite difference formula [49].

Frame dimensions are found through a calibration with a known target: at plasma exit is positioned a plate with 4 holes, diameter of 1.0 ± 0.1 mm at the vertices of a square with an edge lenght of 10.0 ± 0.1 mm, and illuminated from behind with a torch. From the frame relative to this setup it's possible to extrapolate the pixel distance that corresponds to 10 mm for every square edge, average them, and calculate pixel's width in frames, resulting a value of $d_{pix} = 0.172 \pm 0.002$ mm.

3.2 Helium flow

Helium it's an element with standard atomic weight of 4.002, 1st ionization energy of 24.587 eV and 2nd ionization energy of 54.418 eV. It is easy to produce helium plasma, when ionized it emits radiation with principal wavelengths in violet and orange ($\lambda = 388.86$ and 587.56 nm).

In this work helium plasma is produced with pulse repetition rate $f = 5$ kHz and different voltage peak values, as explained in table 3.1. Delays are setted to take a single frame during every acquisition, for every measure are acquired 5 frames.

3.2.1 Bullet description

A description of bullet propagation can be given with setup A, for $\Delta t = 3.5$ μ s, i.e. absence of a target and gas flow of 2 L/min.

It's possible to divide the phenomenon in four phases, as presented in figure 3.8: bullet formation, bullet displacement inside the nozzle, bullet expulsion and bullet propagation outside the nozzle, in air. When the voltage goes over a definite value, a rapid increase in luminosity is observed around the electrode. From there, in a time of ~ 50 ns the plasma modifies it's shape and becomes the bullet: a zone with high luminosity confined in space. The bullet then moves in the exit direction and it's expelled always with a well defined front. The round shaped bullet propagation can be seen in air until it reaches a maximum travel distance and then luminosity decreases rapidly. In these measurements conditions plasma forms again in correspondence of the negative tension peak, but it is a rapid process without propagation.

Electrode voltage and bullet intensity The time interval where there is the bullet can be defined as where it is possible to see a definite zone with mean luminosity higher than the background. The starting time is given by voltage reaching a certain value, and the bullet expires when it's luminosity decreases.

The average intensity value inside the bullet and the voltage measurement in the intersted time interval are presented in figure 3.9. Plasma formation is observed around 120.93 ns after peak start, at a tension value of 5710.00 ± 285.50 V. Luminosity is higher during plasma formation around the electrode and it decrease very little during all the propagation, even after the expulsion in air (pointed line on the graph). After a time of 440 ns the bullet luminosity decreases rapidly and it disperses in the air.

Barycenter coordinates and direction The motion of the bullet on observing plane can be extrapolated from its barycenter coordinates.

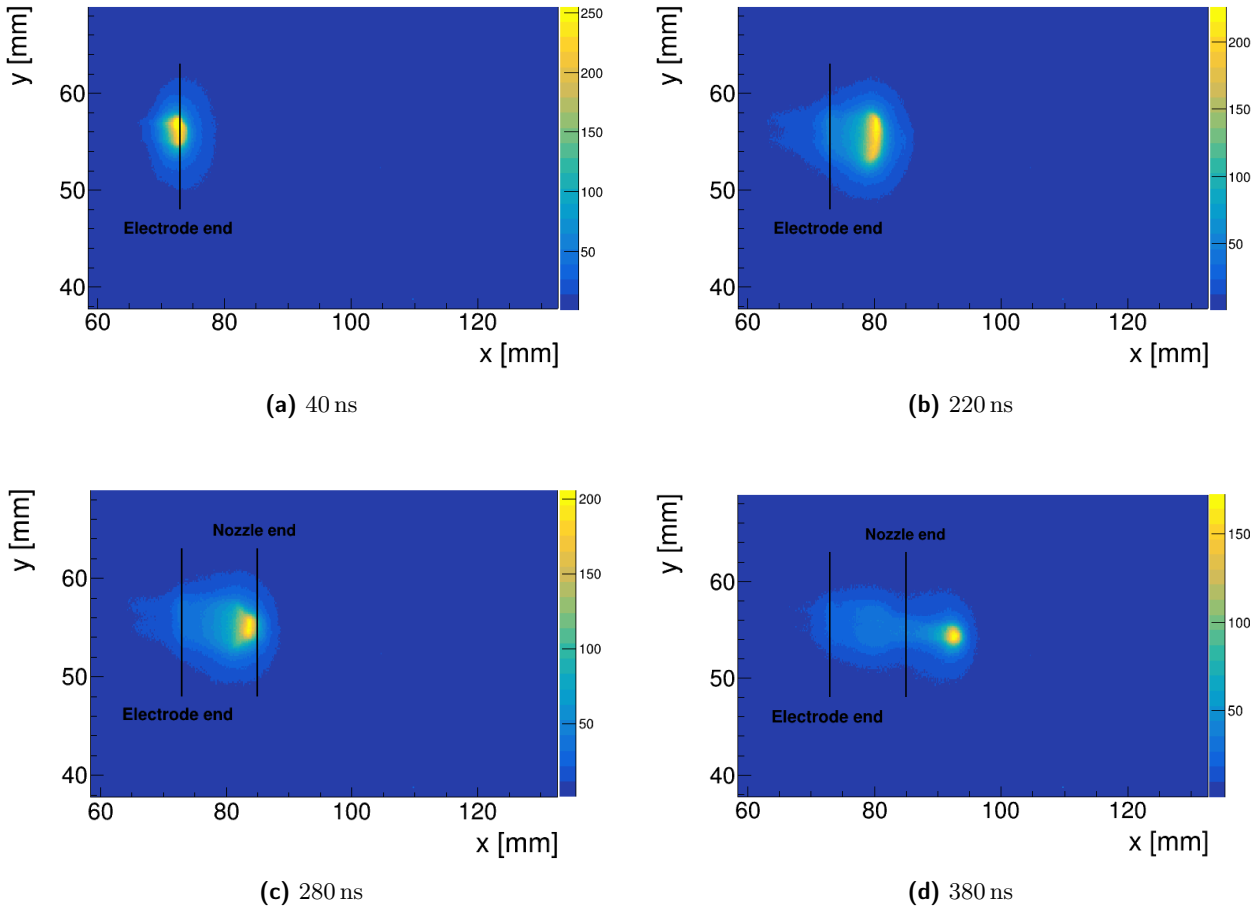


Figure 3.8: 2D histograms relative to four phases of plasma dynamics: bullet formation (a), bullet displacement inside the nozzle (b), bullet expulsion (c) and bullet propagation outside the nozzle (d). Measurement setup A with voltage peak 6.6 kV. Time intervals are calculated from the start of the voltage peak.

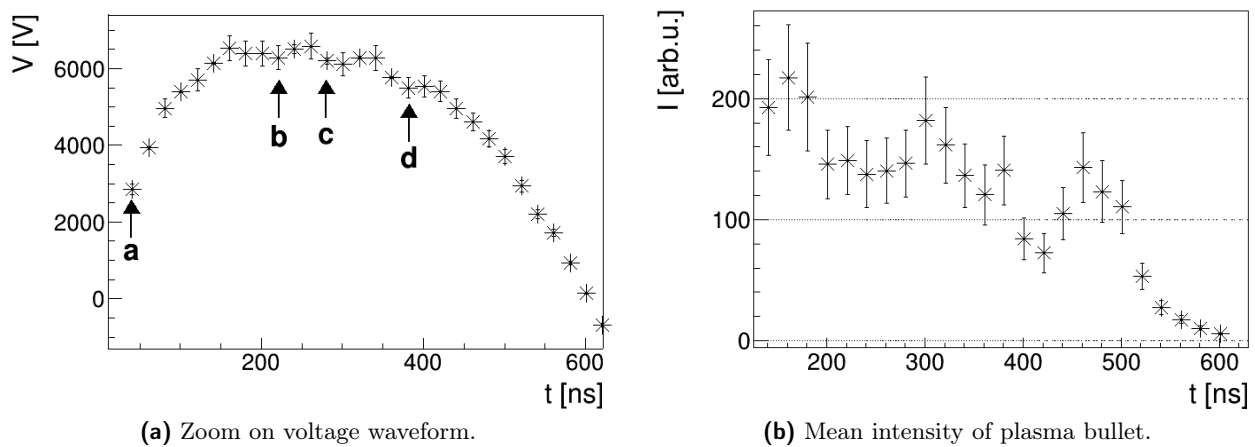


Figure 3.9: Voltage waveform and intensity of the bullet versus time, measurements setup A with voltage peak of 6.6 kV. Time zero is the start of the voltage peak. The letters on the voltage peak indicate frames shown in figure 3.8. Ending time is taken as the time where intensity reaches background value.

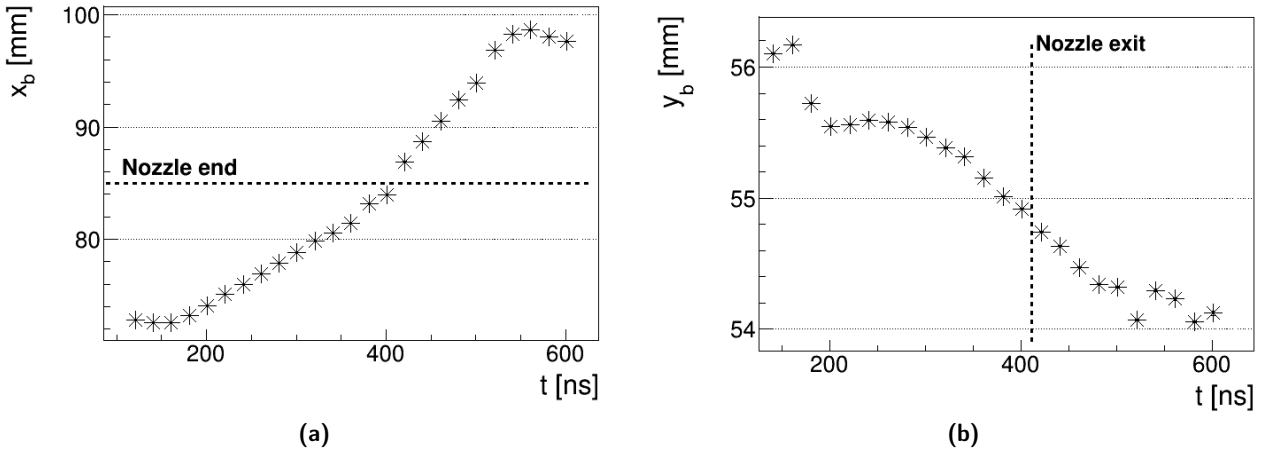


Figure 3.10: Barycenter coordinates of the bullet for measurements setup A with voltage peak of 6.6 kV. Pointed lines indicate the end of the nozzle.

In figure 3.10 there are the two coordinates for different times. Coordinate x , along the axis of the source is more relevant to observe bullet expulsion. Plasma forms around position 73 mm and the nozzle ends at 85 mm, compatible with the distance described before. Plasma bullet moves in the nozzle with a certain velocity, until it reaches the exit and propagates in the air more rapidly. In air the bullet travels until it reaches a maximum x , covering a distance of 26.08 ± 0.02 mm from the electrode. The bullet stops before its luminosity reaches the minimum value.

Coordinate y it's relevant to show bullet direction. From figure it is possible to see that it moves in a space interval of 2 mm. The bullet forms over the electrode, then it enlarges to cover all the nozzle diameter and lowers it's barycenter with a constant slope, even after the expulsion. Once the bullet starts to decrease in luminosity, it stops its motion also on the y direction.

Baricenter motion in the y direction it's explainable by a tilt in the source, that is not perfectly perpendicular to the optical bench. In figure 3.11 there is the countour of the bullet in the y direction in function of the x brycenter coordinate, is possible to see that the figure is inclined. Inside the nozzle y maximum is the value that defines the contour of the nozzle, the angle of inclination is given by a linear fit as in figure and it is $3.39 \pm 0.10^\circ$. Outside the nozzle the barycenter direction is inclined at an angle of $3.71 \pm 0.04^\circ$. The values are almost compatible with each other, so it seems that tilting the source it is possible to direct the bullet even after its propagation in air.

Bullet dimensions Once the contour of the bullet is defined, it is simple to evaluate its dimensions along x and y directions, in figure 3.12 are presented the results for each time. . In the x direction, the bullet presents constant diameter until it approaches nozzle exit, where it enlarges to reach the exit. In air the bullet mantaines its dimension, with lower values than inside the nozzle, but compatible within the error. When it stops the measure loses significance as the bullet loses luminosity and it is not distinguishable from the background. In y direction there is a constant value of 4.65 ± 0.20 mm during propagation in the nozzle, as expected because the bullet covers all the nozzle area. Once the nozzle shrinks, the bullet diminish it's diameter and maintains a constant value of 2.07 ± 0.20 mm during all the propagation in air.

Bullet velocity From barycenter graphs it is possible to estimate the bullet velocity at different times. With a linear fit of the x barycenter inside the nozzle, as shown in figure 3.13, bullet velocity is found to be $v_N = 46.48 \pm 0.20$ km/s. Once it exits the nozzle the speed goes up, until a value of $v_A = 95.16 \pm 0.60$ km/s.

Velocity for each time can be calculated with a 3 point finite difference formula (that excludes the first and the last point), finding the values shown in figure 3.13. The average velocity value inside

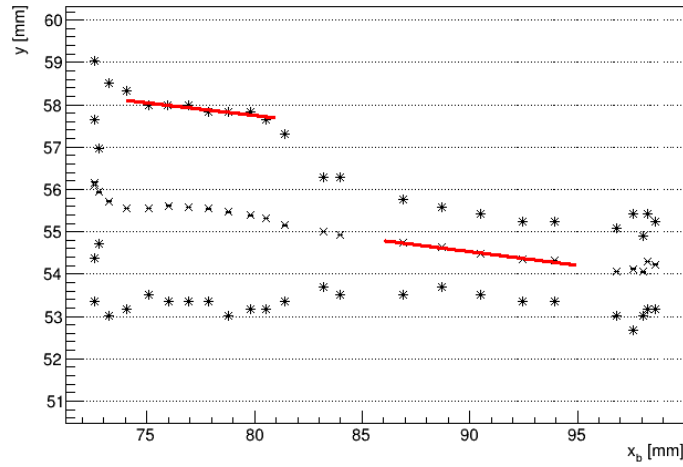


Figure 3.11: Contour of the bullet in y direction as a function of barycenter coordinate x , for measurements setup A with voltage peak of 6.6 kV. For each x value is possible to see y maximum, y minimum and y barycenter of the bullet. There are two linear fits to compare the inclination of the source (first linear fit of y maximum inside the nozzle) with the inclination of bullet propagation direction in air (second linear fit of y barycenter).

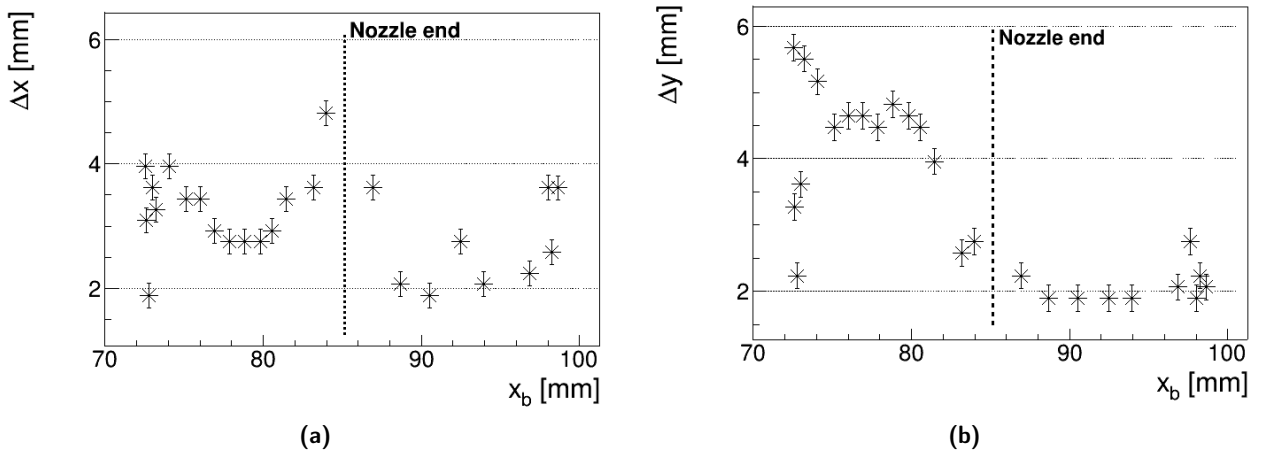
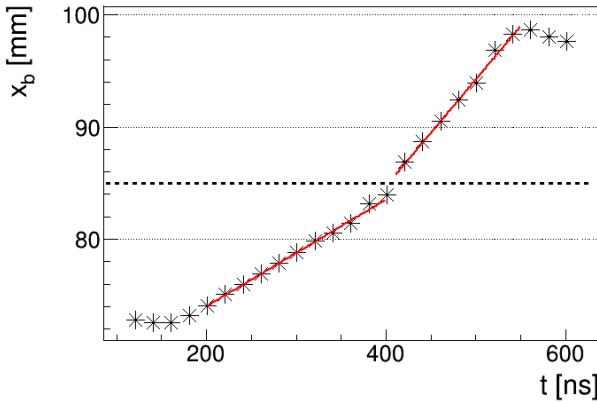
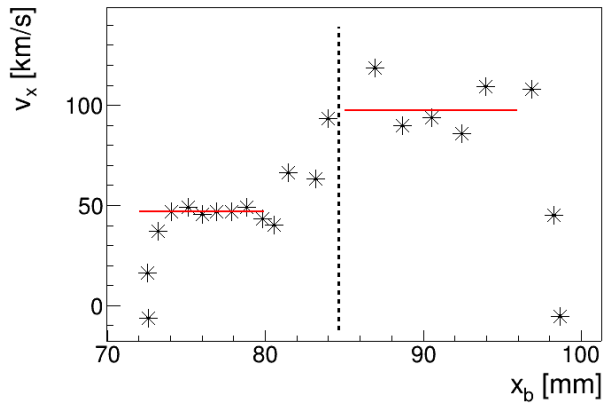


Figure 3.12: Dimensions of the bullet for measurements setup A with voltage peak of 6.6 kV. Pointed lines indicate the end of the nozzle.



(a) Fit of x barycenter.



(b) Velocities in x direction.

Figure 3.13: Velocity of the bullet in x direction for measurements setup A with voltage peak of 6.6 kV. In (a) linear fit of barycenter position as function of time inside the nozzle and in air; in (b) velocities evaluated for each time with a three point difference formula, where lines indicate average values inside the nozzle and in air.

the nozzle and in air is compatible with the result from the linear fit: $v_N = 48.23 \pm 1.03$ km/s and $v_A = 95.16 \pm 1.82$ km/s.

It's interesting to point out that those velocities are much higher then the average velocity of the neutral gas: for a flow of 2 L/min it is of 12 m/s.

3.2.2 Voltage influence

An increase in trigger width Δt correspond to an increase in voltage peak values (see chapter 2) and an increase in electric field intensity. The voltage peak value could change bullet formation and propagation. The results of the analysis for setup A with different voltage values are in figure 3.14 and table 3.2.

The discharge starts always in the same voltage interval, around 5.7 kV. At an higher voltage corresponds an higher luminosity, but the time interval where luminosity decreases is always around 100 ns once it exits the nozzle (figure 3.14 (a)).

The plot for the barycenter coordinates (figure 3.14 (b) - (c)) shows that higher voltage corresponds to further distances reached by the bullet (x_{dist} and y_{dist} in table). For the lower voltage peak the bullet doesn't even propagate in air, as it stops right after nozzle exit.

Dimensions of the bullet (figure 3.14 (d) - (e)) are not influenced by voltage value, they have the exact same behaviour for every measurements set. A single notable difference it's in the y diameter inside the nozzle, where for higher voltage there are slightly larger values. However inside the nozzle there are refraction effects due to the glass, the increase is compatible with the variation in dimensions that could be given by higher luminosity.

Velocity values (figure 3.14 (f)) show how the bullet behaviour is costant during the propagation inside the nozzle and becomes more erratic once it exits. As mentioned before, for the lowest voltage value the bullet stops right after it exits the nozzle, in this configuration it's not possible to find a propagation velocity in air. For other sets velocity has the same profile, with a proportionality between peak voltage value and velocity value: increasing voltage velocity goes from $v_A = 92.93 \pm 0.06$ km/s to $v_A = 149.47 \pm 0.09$ km/s.

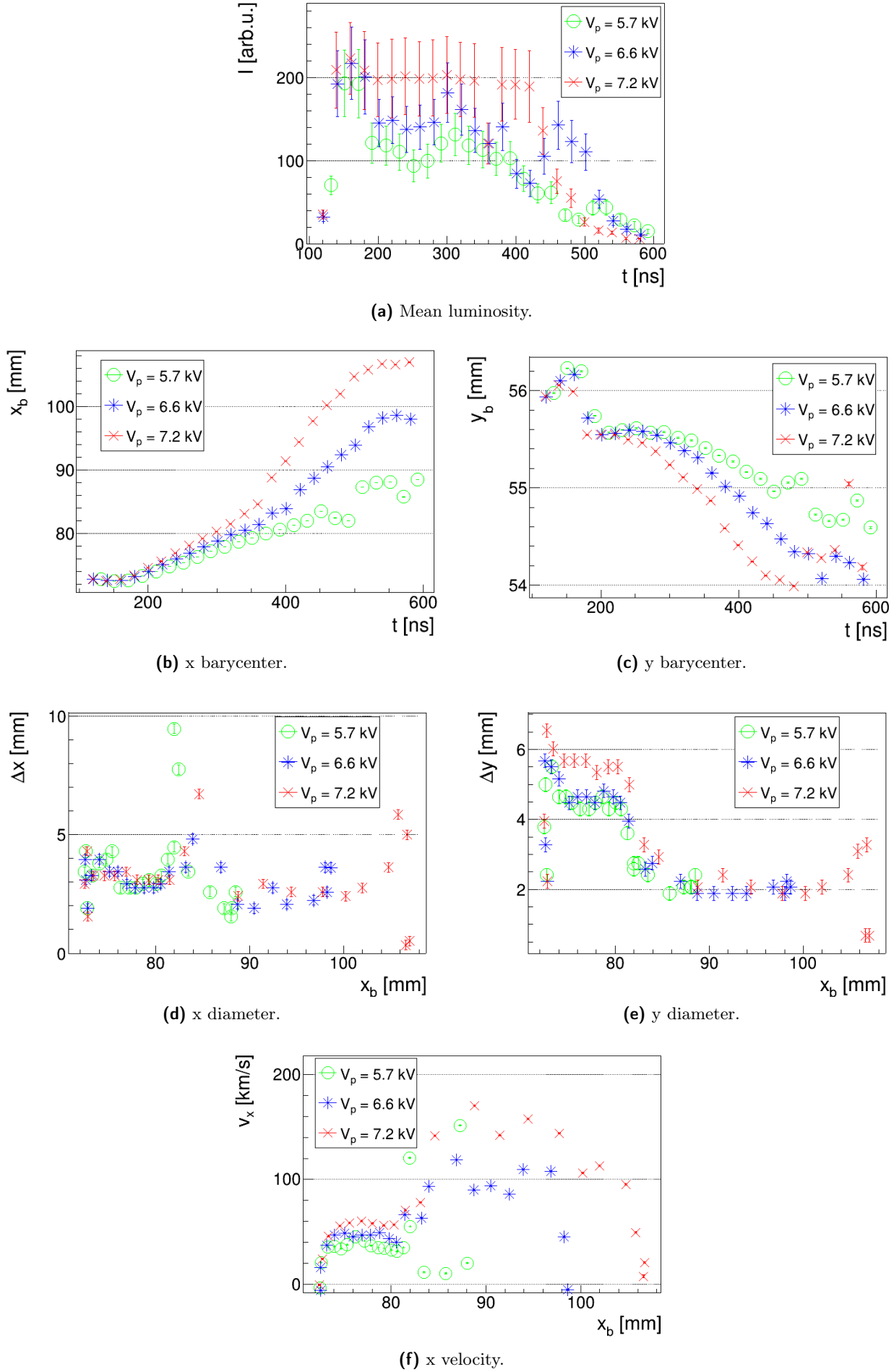


Figure 3.14: Results of the analysis for setup A with helium (gas flow of 2 L/min without target), with different peak voltage values.

V_p [kV]	V_0 [kV]	x_{dist} [mm]	y_{dist} [mm]	v_N [km/s]	v_A [km/s]
5.66 ± 0.30	5.55 ± 0.28	15.99 ± 0.01	1.66 ± 0.02	37.72 ± 0.04	-
6.59 ± 0.33	5.71 ± 0.29	26.08 ± 0.02	1.92 ± 0.04	46.48 ± 0.02	95.16 ± 0.06
7.22 ± 0.36	6.01 ± 0.30	34.55 ± 0.05	2.07 ± 0.01	59.80 ± 0.03	149.47 ± 0.09

Table 3.2: Result of the analysis for measurements setup A with helium. V_p is the voltage peak value, V_0 is the voltage value at plasma formation time, x_{dist} and y_{dist} are the highest distances reached by the bullet from electrode position, v_N is the velocity in x direction reached inside the nozzle, v_A is the velocity of propagation in air in x direction.

Q [L/min]	V_0 [kV]	x_{dist} [mm]	y_{dist} [mm]	v_N [km/s]	v_A [km/s]
1	5.87 ± 0.08	30.65 ± 0.03	2.75 ± 0.01	54.33 ± 0.10	113.97 ± 0.09
2	5.71 ± 0.29	26.08 ± 0.02	1.92 ± 0.04	46.48 ± 0.02	95.16 ± 0.06
3	5.41 ± 0.27	19.38 ± 0.01	1.84 ± 0.01	39.88 ± 0.04	80.96 ± 0.30
4	5.90 ± 0.12	22.80 ± 0.03	2.30 ± 0.01	58.89 ± 0.14	41.94 ± 0.44

Table 3.3: Results of the analysis for setup A, B, C and D in helium: different gas flow, voltage peak value of 5.7 kV, without target. Q is gas flow, V_0 is the voltage value at plasma formation time, x_{dist} and y_{dist} are the highest distances reached by the bullet from electrode position, v_N is the average velocity in x direction inside the nozzle, v_A is the average velocity of propagation in air in x direction.

3.2.3 Flow influence

As said before, neutral gas velocity is low if compared to bullet speed, however it could influence the overall dynamic of bullet propagation. Setup A, B, C and D correspond to four different flows with the same peak voltage. In figure 3.15 and table 3.3 are presented the results of the analysis.

Also for this parameter, the discharge starts always in the same voltage interval, for values higher than 5.7 kV. For gas flows of 1 and 2 L/min bullet luminosity decreases in a time interval around 100 ns once it exits the nozzle. For flows > 2 L/min it has luminosity clearly stronger than background for a longer time interval, around 200 ns (figure 3.15 (a)).

From the barycenter coordinates (figure 3.15 (b) - (c)) can be seen that more gas flow is correlated with lower mobility of the bullet: it propagates for shorter distances when there are higher flows. For maximum flow, even if bullet luminosity is comparable to the other measurements, the bullet travels a short distance from the exit of the nozzle and its barycenter stays in the same position until bullet luminosity reaches background value.

The study of bullet's velocity can give more insight to the phenomenology of bullet propagation, it is shown in figure 3.15 (e), with higher detail for values inside the nozzle in figure 3.15 (f). Bullet's velocity always decreases moving inside the nozzle, until it reaches a certain distance. The deceleration inside the nozzle is more evident with higher flow, especially when the flow is higher than 3 L/min (as we can see also in [47]). The distance at which the bullet speeds up is different for different flows as can be seen in table 3.4. Once the bullet exits from the nozzle, its velocity decreases more rapidly with higher gas flow.

The different behavior of the bullet with different neutral gas flow could be related to the variation of the Reynold number of the fluid, that could assume critical values. Following the study in [50] the Reynold number with different flow can be evaluated as in equation 3.1, where v is the gas velocity found from the gas flow value Q , ρ is helium density, μ is helium viscosity and D is the nozzle diameter.

$$Rn = \frac{v\rho D}{\mu} = \frac{Q}{\pi(D/2)^2} \frac{\rho D}{\mu} \quad (3.1)$$

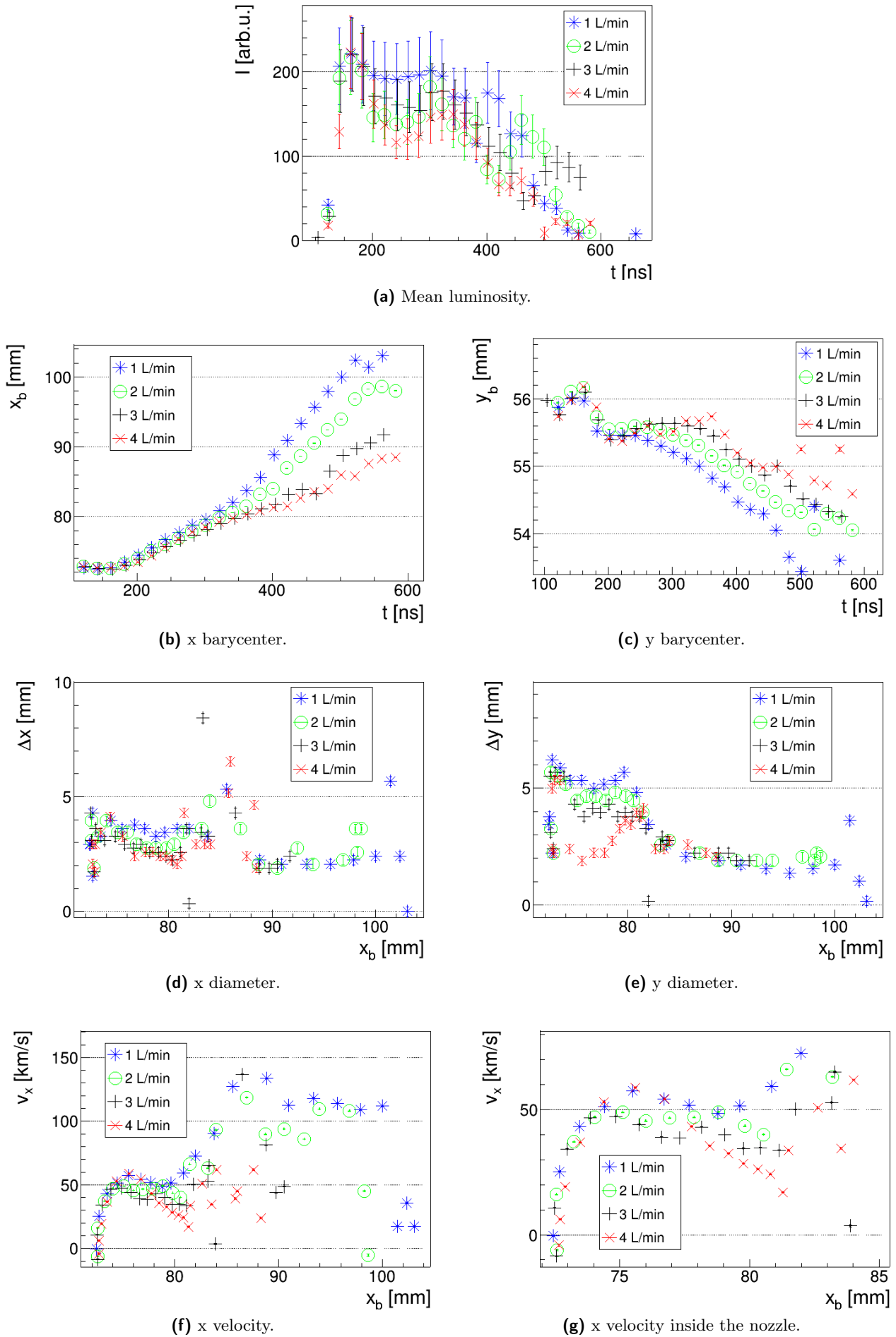
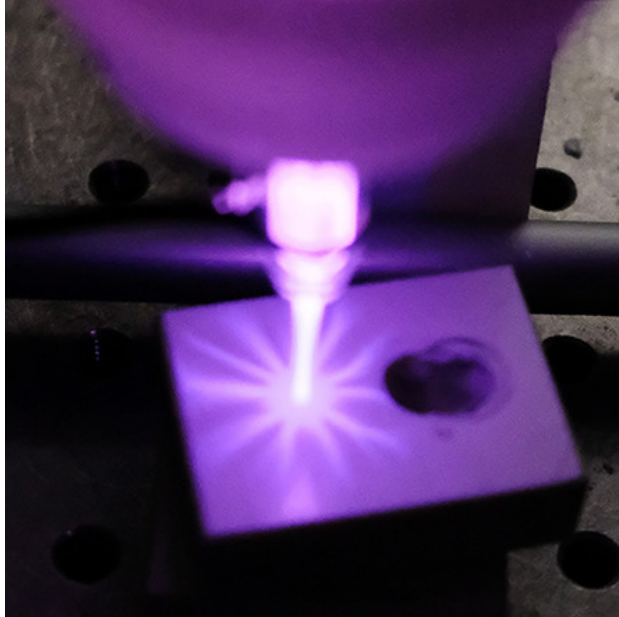


Figure 3.15: Results of the analysis for setup A, B, C and D in helium: different gas flow, voltage peak value of 5.7 kV, without target.

Q [L/min]	$v_{N,\min}$ [km/s]	x_{air} [mm]	Rn
1	48.46 ± 0.10	5.78 ± 0.02	36.88
2	40.09 ± 0.12	7.55 ± 0.02	73.77
3	33.74 ± 0.12	81.75 ± 0.04	110.65
4	17.01 ± 0.16	81.28 ± 0.04	147.54

Table 3.4: Bullet propagation parameters inside the nozzle for different helium gas flow. Q is gas flow, v_N is the lowest velocity reached inside the nozzle; x_{air} is the position where the bullet increases velocity, thought to be where the bullet meets the air outside the nozzle; Rn is the Reynold number associated to the gas flow.



(a) Picture of the setup.



(b) Frame showing bullet on target impact.

Figure 3.16: Impact of plasma on an insulating target with helium gas. In (a) picture of the plume, in (b) frame acquired for setup E, voltage peak 7.2 kV.

Resulting values are presented in table 3.4, always below critical Reynold number (> 2000), there is not transition from laminar to turbulent flow for changes on neutral gas flow from 1 to 4 L/min.

While the bullet propagates inside the nozzle, at a certain time it meets the air outside, changing the elements that participate in ionization reactions from helium to those found in air. The bullet decelerate inside the nozzle and accelerate when it meets air [47]. The change in bullet velocity when there is an increase in neutral gas velocity could be related to the different transition time and position from helium to air. With an higher flow the bullet travels in a gas of almost only helium for longer time and its velocity decreases more, leading to a different dynamic during propagation in air.

3.2.4 Insulating target

The electric field created by the electrode is not expected to change if there is an insulating target in front of the nozzle. An interesting effect is seen after the bullet impacts on the target, as shown in figure 3.16: plasma forms a round shaped figure on the insulator that enlarges on the target until the luminosity decreases.

Barycenter x coordinate of the bullet and its diameter are presented in figure 3.17. While for the lowest tension value the bullet stops before it reaches the target, for the other two sets it clearly stops at

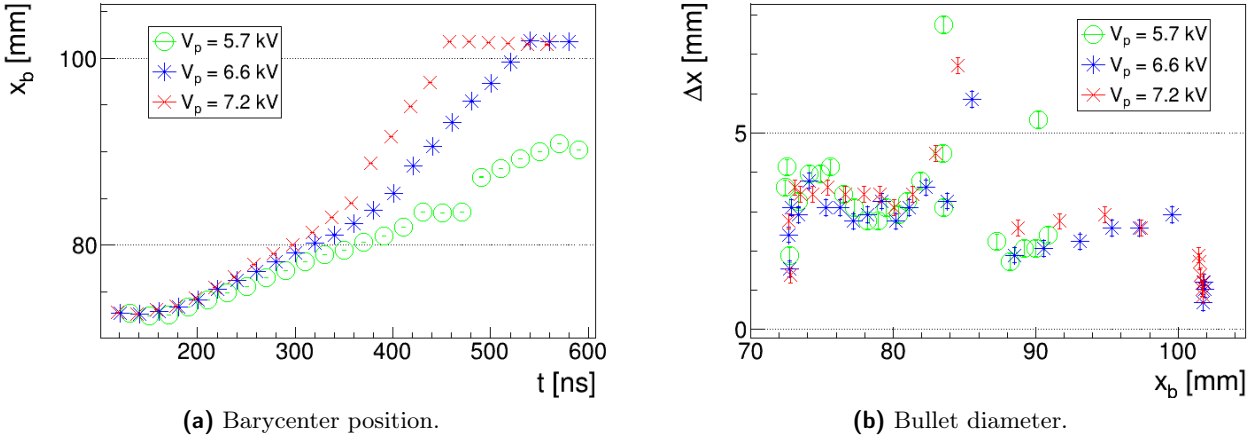


Figure 3.17: Barycenter motion and diameter in x direction for measurements setup E with helium gas (presence of insulating target) for different voltage peak values.

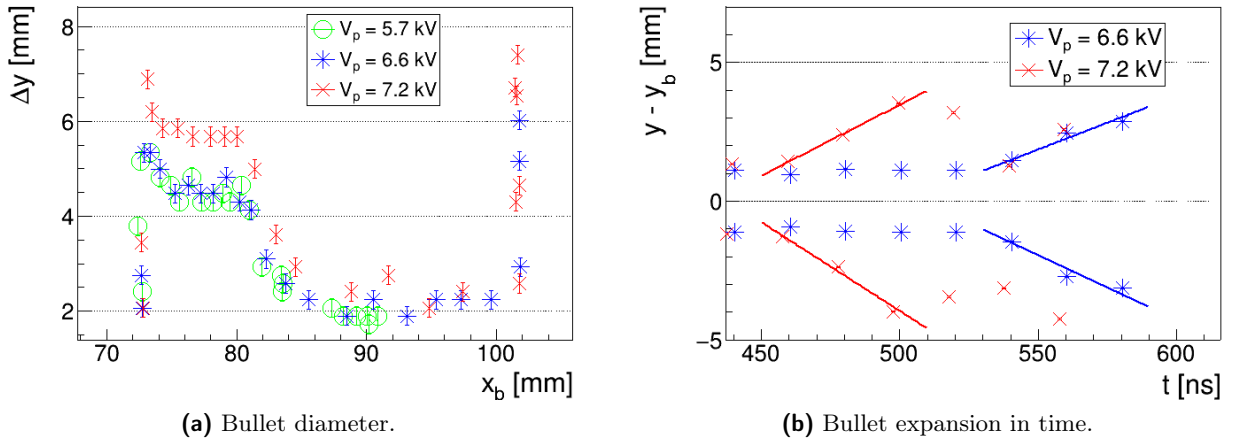


Figure 3.18: Plasma propagation in y direction on an insulating target with helium, for measurements setup E. In (a) there is the absolute value for the diameter for all barycenter positions; in (b) the expansion of y contour after it reaches the target for medium and high voltage peak value. Contour values are calculated as difference with the barycenter y coordinate, linear fits show how much the diameter enlarges in time.

the target position. Distance values are comparable with those without target (figure 3.14), higher for medium voltage value. Bullet width is exactly the same with or without target, it shows differences only when it impacts on the target and shrinks rapidly.

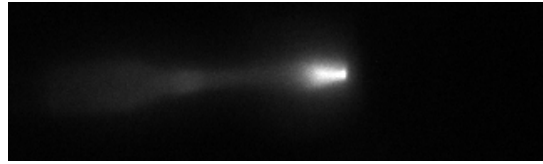
Charge deposition Once the bullet reaches the target it is possible to see how the glowing region enlarges on its surface and the bullet diameter increases, as shown in figure 3.18. Is possible to evaluate the expansion diameter and velocity observing bullet contour in the y direction once the bullet reaches the target. In figure 3.18 can be seen that the diameter and the expansion velocity are higher for higher voltage value: for a voltage peak of 6.6 kV the shape on the insulator has a maximum diameter of 6.54 ± 0.04 mm and an expansion velocity of 31.36 ± 0.25 km/s; for 7.2 kV the values are 7.40 ± 0.02 mm and 64.04 ± 0.39 km/s.

3.2.5 Conductive target

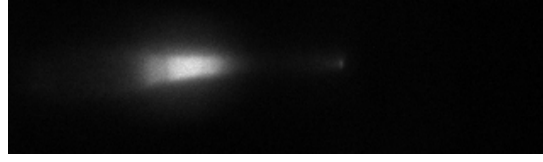
A grounded conductive target could influence bullet propagation because it fixes the value of the electric field on that point in space and it presents free charges on its surface. In measurements setup F and



(a) Bullet propagation 160 ns.



(b) Bullet impact 200 ns.



(c) Backstream 260 ns.

Figure 3.19: Examples of frames showing impact on a conductive target and consequent backstream, measurements setup F with voltage peak value 7.2 kV, helium gas.

G a conductive target is positioned in two different positions.

For measurement setup F a conductive target is positioned at 24 mm from the bench, correponding to 30 mm from the electrode.

When the bullet impacts on the conductive target can be observed a rapid increase in luminosity on the target and in the space between nozzle and target as shown in figure 3.19. In this work it will be referred as “backstream” (because it seems to have motion inverse to that of the bullet). Analysis of bullet propagation, impact and evolution on target is treated separately from analysis of backstream, to allow comparision with other measurements setup.

Bullet dynamics Bullet propagation is different if compared to measurements without conductive target. From figure 3.20 is possible to see that bullet luminosity presents an increase in correspondence of the second voltage peak (negative). This results in an increase of bullet lifetime up to 900 ns from the first voltage peak.

Barycenter motions shows that even with low voltage the bullet reaches the target, different from the behavior with the insulating target. Propagation velocity is higher then values found in other configurations. Bullet diameter doesn't shows different behaviour, it stays constant until nozzle exit and remains constant until it reaches the target and shrinks to a point. As said before, velocities of propagation in air are generally larger then whitout target, they arrives from 112.04 ± 0.05 km/s for low voltage peak to 160.55 ± 0.09 km/s for high voltage peak.

Current measurements Current intensity flowing in the conductive target due to charge transported by plasma can be measured. The correlation between bullet and charge deposition can be verified observing the relation between impact time and peak current starting time.

Current intensity it's shown in figure 3.22, it presents two peaks, a positive one and a negative one. For the lowest voltage value current peaks are not high enough to analyze them, this set is excluded from the following analysis. The positive peak value starts at time $t_{0,i}$ and reaches the maximum at time $t_{0,i}$. Both values are inversely proportional to voltage peak value, we have lower and slower current intensity when the voltage is lower. Those times can be compared with the impact time of the bullet

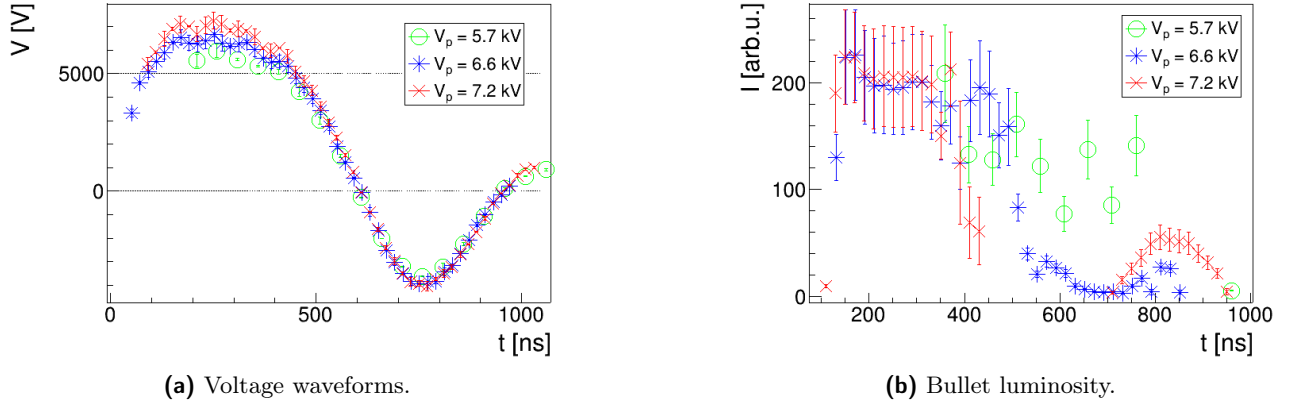


Figure 3.20: Voltage on the electrode and bullet luminosity for measurements setup F for helium gas, different peak voltage values. Note the second luminosity peak in correspondence of the negative voltage peak.

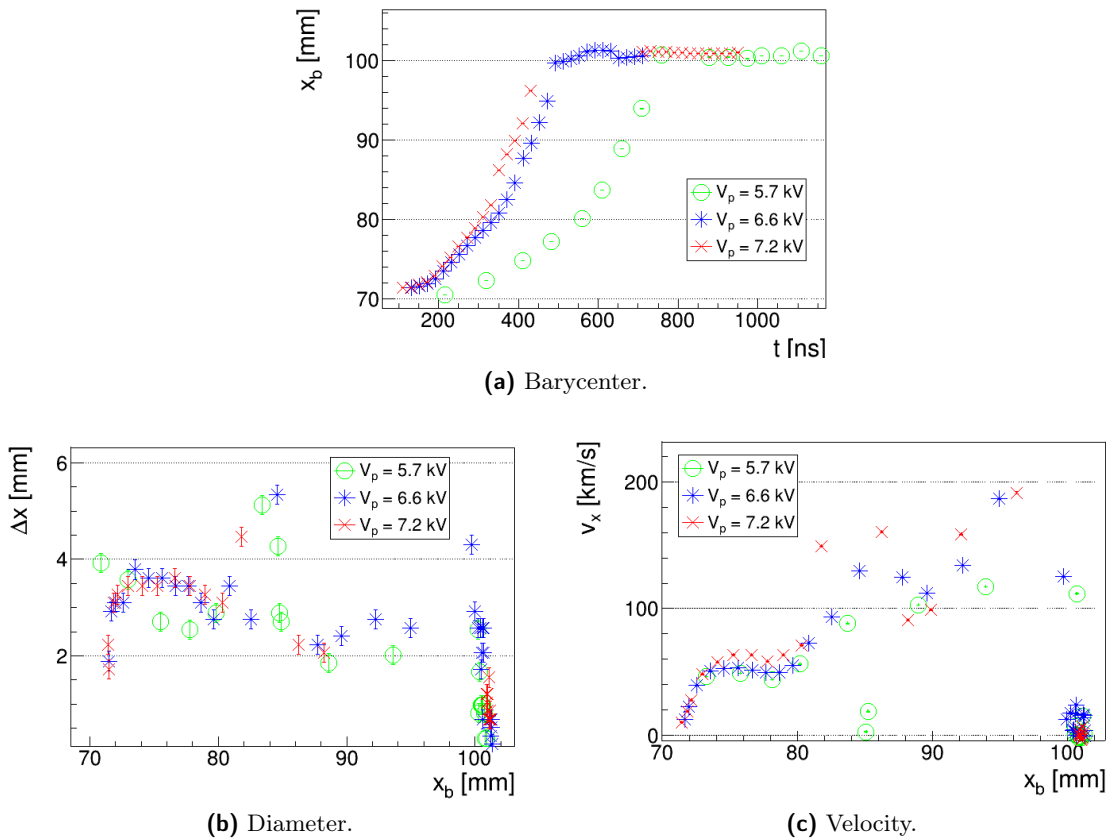


Figure 3.21: Bullet barycenter coordinate, diameter and velocity along x direction, for measurement setup F and for different peak voltage values for helium gas. Can be seen as the bullet reaches the target, it shrinks and stops.

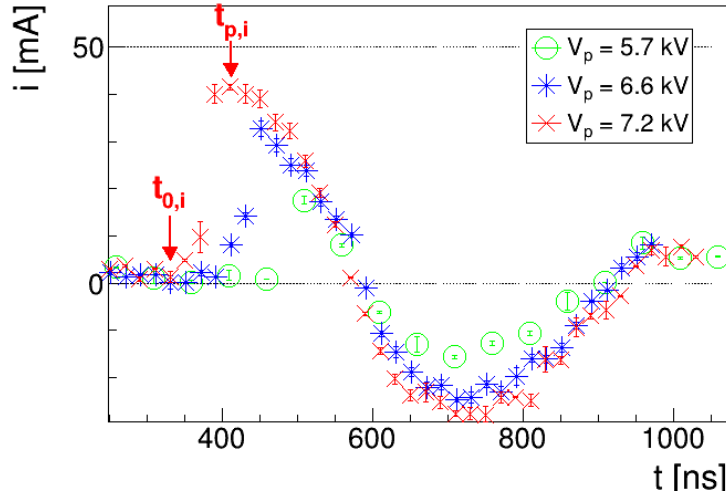


Figure 3.22: Current intensity for measurements setup F with helium, for different voltage peak values. For the measurements set with voltage peak value $V_p = 7.2 \text{ kV}$ it is possible to see $t_{0,i}$, i.e. the starting time of the current pulse, and $t_{p,i}$, i.e. the time relative to maximum current.

V_p [kV]	i_p [mA]	$t_{0,i}$ [ns]	$t_{p,i}$ [ns]	t_{imp} [ns]	$x_{\text{target}} - x(t_{0,i})$ [mm]
6.6 ± 0.3	32.63 ± 1.63	391.6 ± 15.0	451.6 ± 15.0	511.6 ± 15.0	9.22 ± 0.01
7.2 ± 0.4	41.50 ± 0.62	350.3 ± 15.0	410.3 ± 15.0	450.3 ± 15.0	15.18 ± 0.02

Table 3.5: Results of the analysis of current measurements for setup F with helium. V_p is the voltage peak for the pulse, i_p is the current peak value, $t_{0,i}$ is the starting time for the current pulse, $t_{p,i}$ is the time relative to maximum current, t_{imp} is the time impact of bullet on target, $x_{\text{target}} - x(t_{0,i})$ is the distance between bullet position when we start to measure current and target position.

on the target, t_{imp} , in table 3.5 are presented the values. It is possible to see that current starts flowing into the target before the bullet reaches the target, and even maximum current is measured before the impact time of the bullet. It's also interesting to evaluate the distance of bullet from target when we measure current, in table 3.5 there is the difference between bullet barycenter position and target position $x_{\text{target}} - x(t_{0,i})$.

Those results could be explained by the presence of ionized particles that does not produce reactions with emission at visible wavelengths. Current would be measured even without seeing the impact of plasma on the target if the bullet has a diameter higher than the one measurable with the camera. This invisible portion of the bullet would have the same behavior of the bullet for different voltage values, i.e. it would increase its velocity with higher voltage. As can be seen from table 3.5 the current peak starts indeed before with higher voltage.

Backstream Dynamics of the backstream is difficult to analyze as it's a rapid phenomenon with too high luminosity. Frames right after the impact of the bullet on target present another zone with high luminosity right after nozzle exit. This other glow has stable position and diameter, as can be seen in figure 3.23, with a slow tendency to shift towards the target when voltage is positive and towards the electrode when it's negative. The phenomenon can be explained as a very rapid charge stream from the target to the electrode, that stops when meets the nozzle, but to study it are necessary other specific measures with more time resolution.

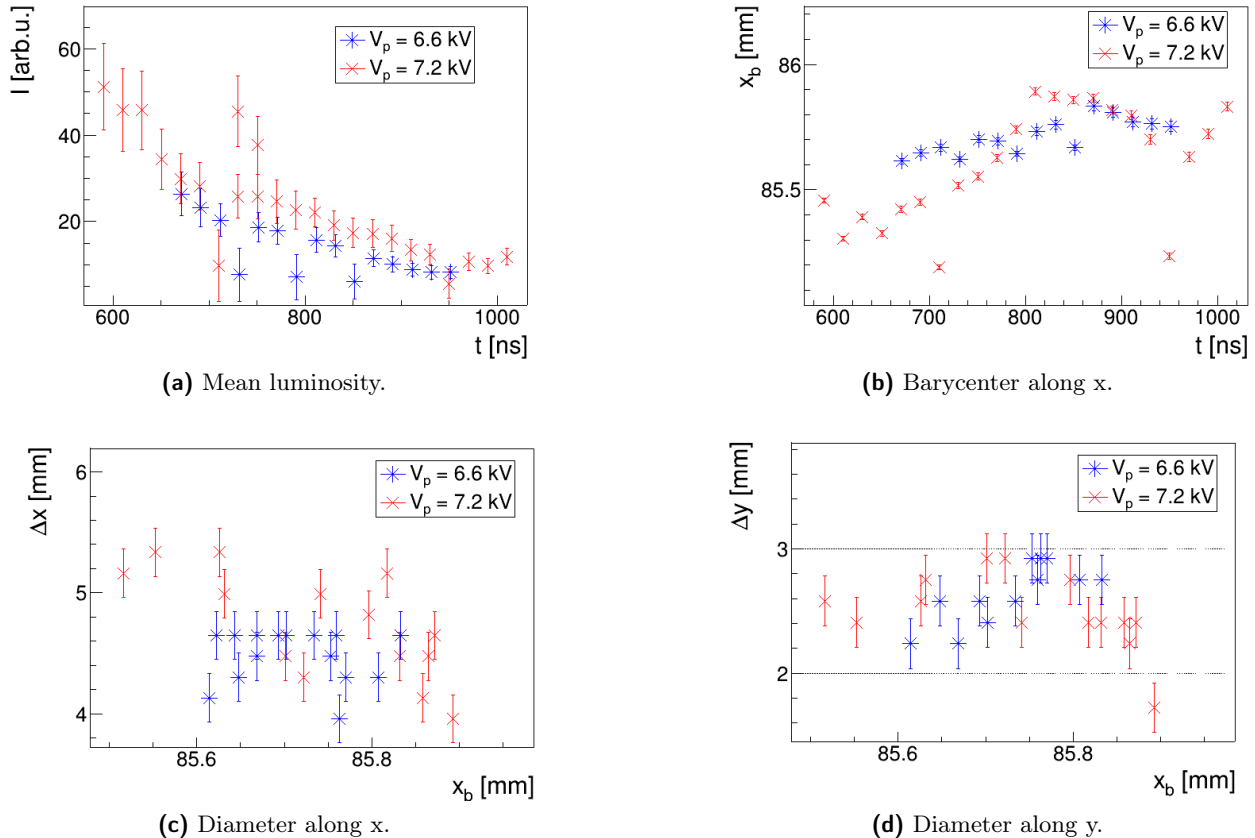


Figure 3.23: Backstream analysis for measurements setup F with helium. It's possible to see the decreasing luminosity while the barycenter stays around the nozzle exit and diameter stays constant.

V_p [kV]	i_p [mA]	$t_{0,i}$ [ns]	$t_{p,i}$ [ns]	t_{imp} [ns]	$x_{\text{target}} - x(t_{0,i})$ [mm]
5.7 ± 0.3	47.41 ± 2.37	370.6 ± 15.0	450.6 ± 15.0	450.6 ± 15.0	11.34 ± 0.02
6.6 ± 0.4	77.41 ± 3.87	311.2 ± 15.0	411.2 ± 15.0	391.2 ± 15.0	13.61 ± 0.04

Table 3.6: Values extrapolated from current measurements and bullet barycenter motion for setup G with helium. V_p is the voltage peak for the pulse, i_p is the current peak value, $t_{0,i}$ is the starting time for the current value, $t_{p,i}$ is the time of current peak value, t_{imp} is the time of the impact of bullet on target, $x_{\text{target}} - x(t_{0,i})$ is the distance between bullet position when current peak starts and target position.

Position of the target

The position of the target could influence bullet propagation. In measurement setup G the conductive target is positioned at 32 mm from the bench, corresponding to 22 mm from the electrode, closer to the nozzle respect setup F.

With a conductive target this close it's more difficult to see the bullet evolution, as it is more rapid and the backstream has even higher relevance.

In figure 3.24 are presented the results of the analysis. For all the sets there is high luminosity, even after a time interval corresponding to the end of the voltage peak. For higher voltage peak values, it is not possible to see the bullet, as it reaches the target in a sort of large plume right after nozzle exit. The other two sets shows the same behaviour described before, with even higher velocities: for medium voltage velocity inside the nozzle velocity is 59.30 ± 0.05 km/s, while maximum velocity in air is 174.44 ± 0.08 km/s.

Current measurements As done with previous setup, for low and medium voltage it's possible to analyze time and space intervals between bullet barycenter motion and current measurements. Obtained values are shown in table 3.6.

Again current flows in target before the impact of the bullet, when it is distant from the target (parameter $x_{\text{target}} - x(t_{0,i})$ in table). Comparing these values with results for setup F, is possible to see that for the same voltage peak value, the current peak starts faster and reaches an higher peak value. Hypothesizing that charge motion is correlated to bullet motion an earlier impact point means that the bullet will lose less charge during the propagation in air and that there will be higher current intensity flowing on target.

3.3 Neon flow

The second noble gas used to produce cold plasma is neon, the one with more emission intensity at visible wavelength. Neon it's an element with standard atomic weight of 20.180, 1st ionization energy of 21.565 eV and 2nd ionization energy of 40.963 eV and several lines with wavelength in visible spectrum. It's easy to produce neon plasma, when the voltage pulse is applied, even with low repetition rates, the gas presents high luminosity in a wide space. This emissivity it's the reason why neon is commonly used to build neon lamps.

The working pulse repetition rate is set to $f = 1$ kHz and three opening times equivalent to low, medium and high voltage in helium. Different measurement setup are presented in table 3.1.

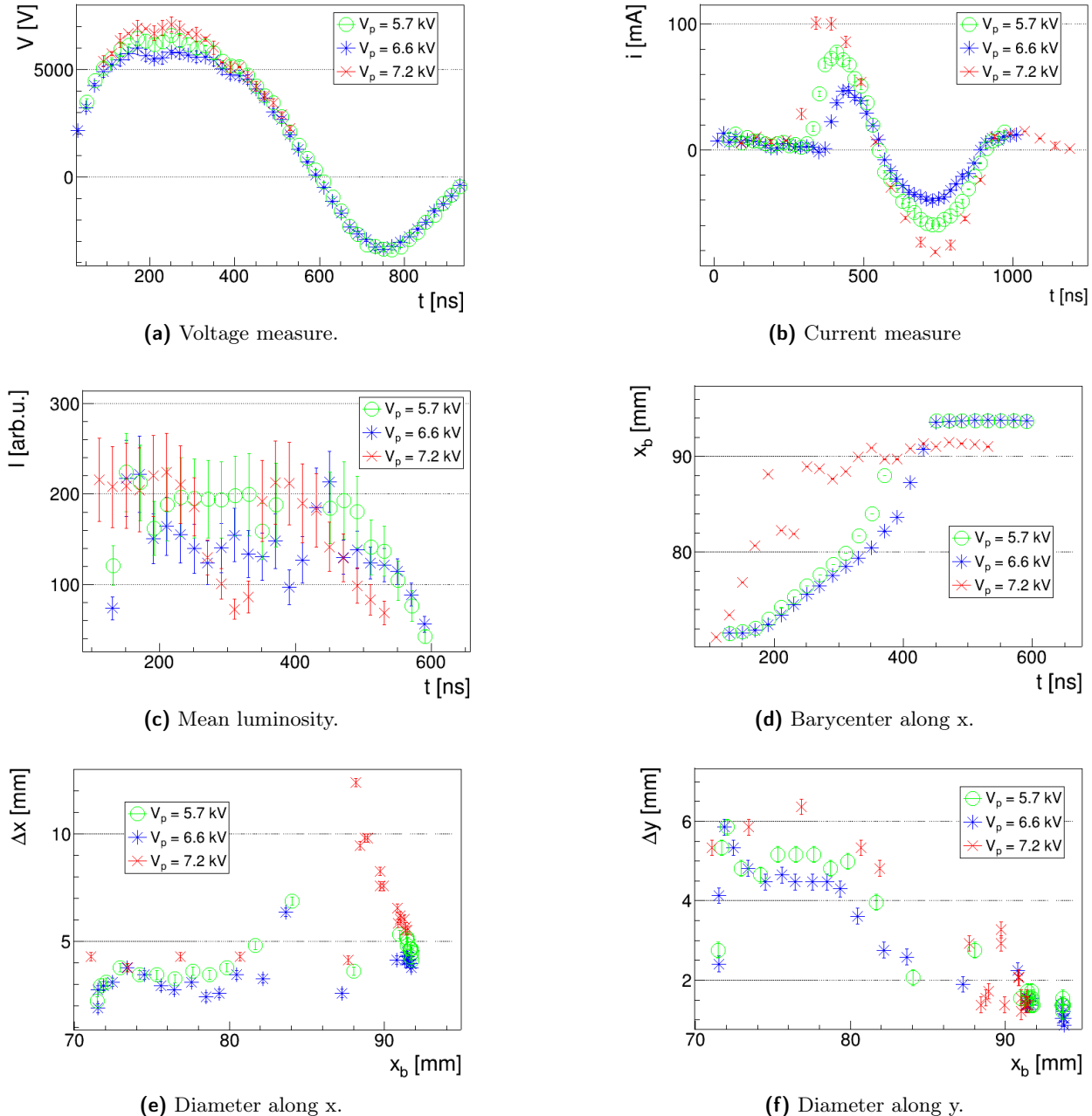


Figure 3.24: Analysis of measurement setup G with helium: conductive target positioned close to the nozzle, at 22 mm from the electrode.

V_p [kV]	V_0 [kV]	x_{dist} [mm]	v_N [km/s]	v_A [km/s]
4.81 ± 0.24	4.81 ± 0.24	18.13 ± 0.05	34.59 ± 0.03	43.19 ± 0.07
5.33 ± 0.27	5.20 ± 0.26	22.42 ± 0.06	42.82 ± 0.04	61.17 ± 0.05
6.05 ± 0.30	5.16 ± 0.26	26.60 ± 0.09	62.92 ± 0.05	160.32 ± 0.07

Table 3.7: Results of the analysis for measurements setup A with neon, for different voltage peak values. V_p is the peak value for the pulse, V_0 bullet formation tension, x_{dist} is the highest distances reached by the bullet from electrode position, v_N is the velocity in x direction reached inside the nozzle, v_A is the velocity of propagation in air.

3.3.1 Bullet description

First measurements are done to see plasma dynamics without a target, changing between low, medium and high tension peak value. Results are shown in figure 3.25 and table 3.7. First thing to notice is that plasma is produced not specifically at electrode's end where the electric field should be higher, as in helium, but a little before, with lower luminosity. Luminosity evolution from there is similar to that of helium bullet, but there is a residual luminosity tail that lasts longer. Barycenter motion and diameter evolution present the same evolution of helium bullets inside the nozzle. Outside the nozzle there are two main differences:

- neon bullets come out of the nozzle more difficultly and lose velocity more rapidly, covering shortest distances. Propagation velocity in air rises exiting the nozzle (until 160.32 ± 0.07 km/s with high voltage), but goes down abruptly and the bullet slows down rapidly.
- neon bullet's x diameter rises increasing voltage. As can be seen from figure 3.25 (e)-(f), diameter evolution is the same as in helium bullet, but there are higher diameter values with higher voltage.

Those differences can be explained by the different reactions that have place in neon plasma. If those reactions need less energetic electrons, we would have more of them that participates, increasing the diameter of the bullet.

For both helium and neon inside the nozzle there is bullet propagation, it is possible to compare how the velocity v_N changes varying voltage peak value for the gasses. In figure 3.26 there is the plot for the two gasses. With few points it's not possible to extrapolate accurately the behavior, but a linear plot shows that helium bullet's velocity grows with a slope of 14.55 ± 2.40 km/s/kV, while neon bullet's velocity has a slope of 23.23 ± 3.66 km/s/kV. Those values are of the same magnitude, but not compatible, suggesting that bullet's velocity may depend from gas composition.

3.3.2 Insulating target

Also for neon is studied the dynamic with an insulating target positioned at 30 mm from the electrode, in measurement setup B. Results are similar with helium or neon bullets: plasma forms near the electrode, exits from the nozzle and the impact on the target produce a round shaped figure on it, as in figure 3.16. Also in neon for low voltage peak value the bullet doesn't reaches the target, as the maximum distance travelled is lower than target distance. This suggests that the target does not influences the bullet when it is not in its proximity. A peculiarity with neon is that there is a second, very low, peak in luminosity corresponding to the second voltage peak of the pulse.

The figure that bullet impact produces on target can be analyzed as with helium. In figure 3.28 there is the y contour in function of time and is possible to extrapolate an expansion velocity of 5.01 ± 0.29 km/s for medium voltage and 30.76 ± 0.25 km/s for high voltage. They are both lower compared to helium, probably because the bullet in neon slows down more rapidly once it's outside the nozzle.

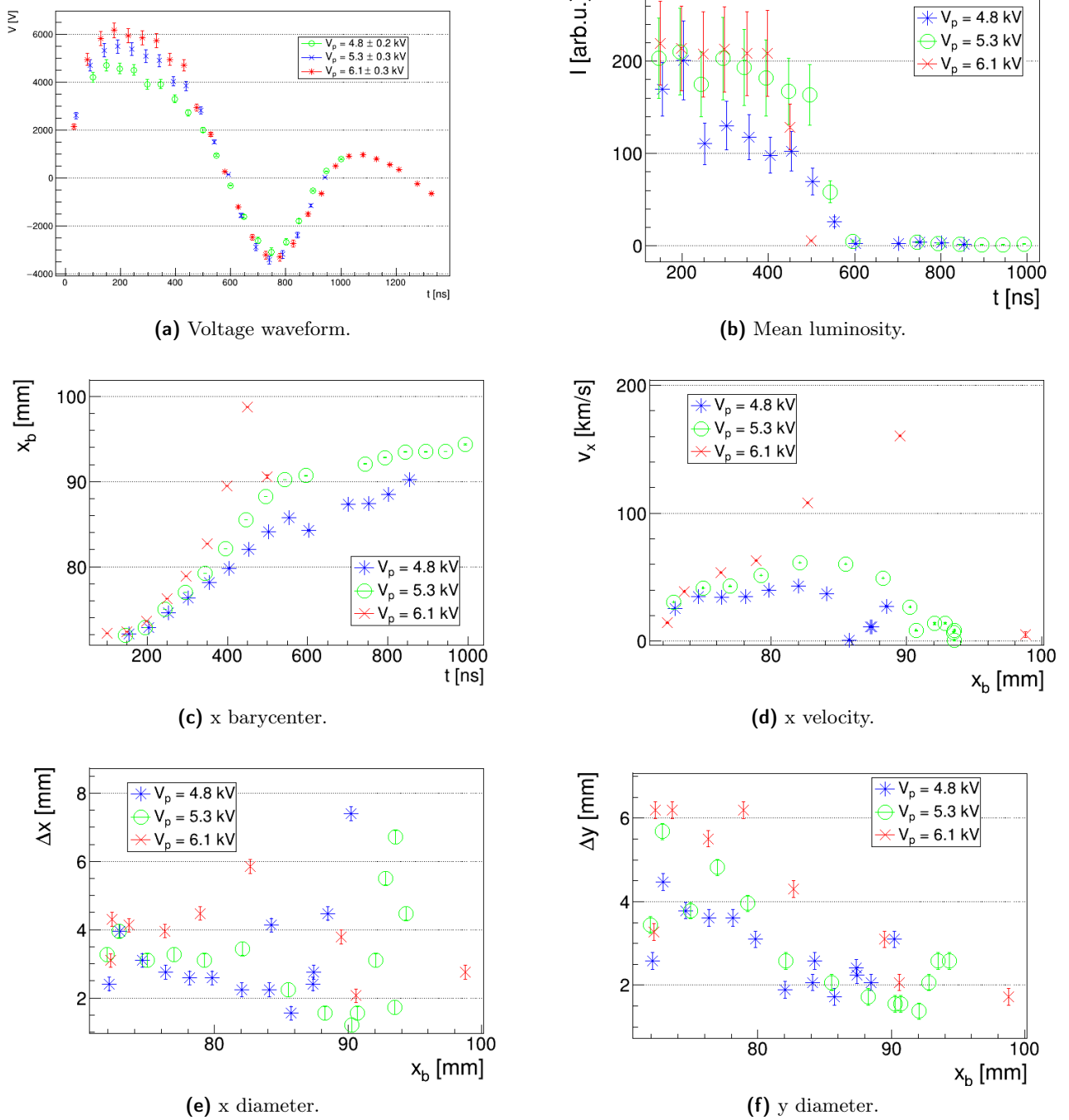


Figure 3.25: Results of the analysis for measurement setup A with neon gas, for different peak voltage values.

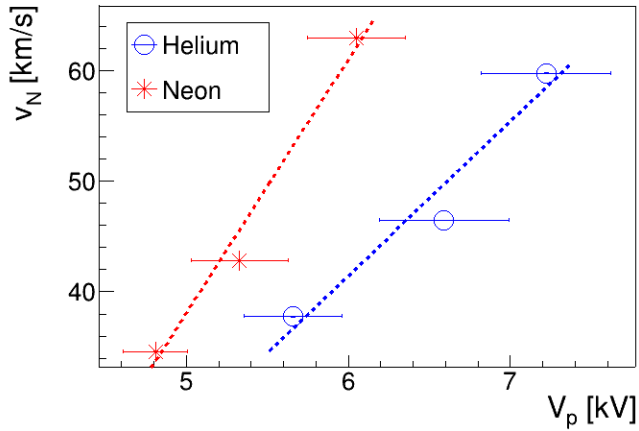


Figure 3.26: Bullet velocity inside the nozzle as a function of voltage peak value, for helium and neon.

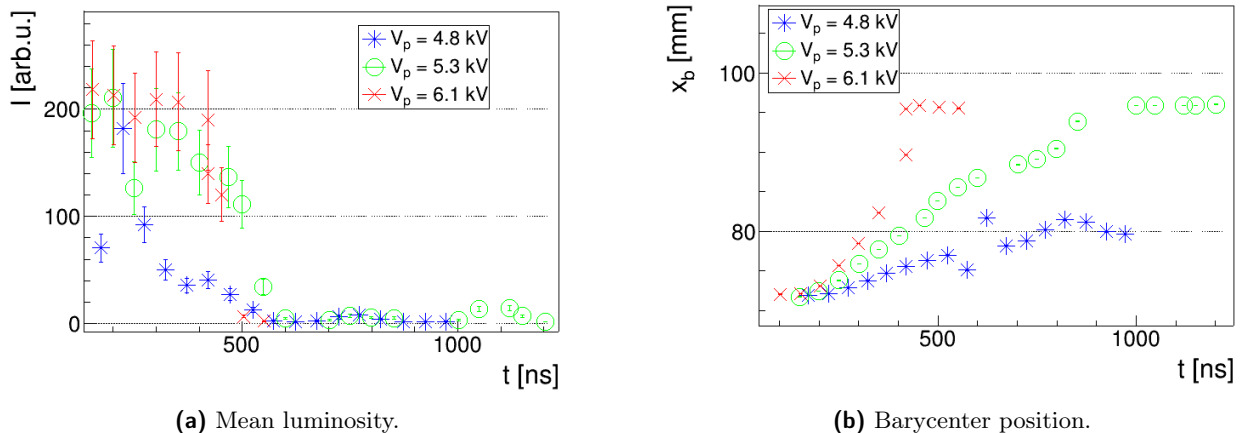


Figure 3.27: Mean luminosity and barycenter motion for neon gas in setup measurement D.

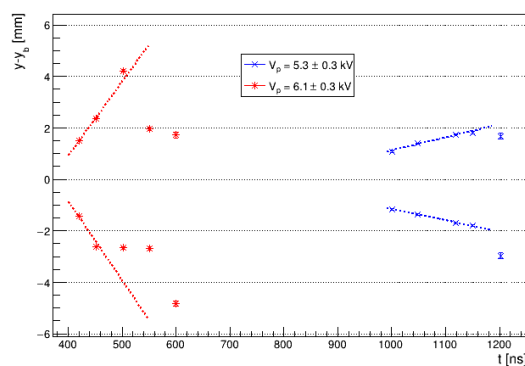


Figure 3.28: Neon plasma expansion on insulator target, measurements setup B for different voltage peak values.

Δx_{targ} [mm]	V_p [kV]	i_p [mA]	$t_{0,i}$ [ns]	$t_{p,i}$ [ns]	t_{imp} [ns]	$x_{\text{target}} - x(t_{0,i})$ [mm]
30	6.05 ± 0.30	6.87 ± 0.34	329 ± 15	477 ± 15	453 ± 21	19.96 ± 0.03
22	5.33 ± 0.27	7.72 ± 0.39	347 ± 15	447 ± 15	447 ± 15	13.06 ± 0.03
	6.05 ± 0.30	14.56 ± 0.73	300 ± 15	398 ± 15	380 ± 21	13.66 ± 0.04

Table 3.8: Values extrapolated from current measure and bullet barycenter motion for neon in setups C and D. Δx_{targ} is the distance between electrode and target, V_p is the voltage peak for the pulse, i_p is the current peak value, $t_{0,i}$ is the starting time for the current value, $t_{p,i}$ is the time of the peak value, t_{imp} is the time of the impact of bullet on target, $x_{\text{target}} - x(t_{0,i})$ is the distance between bullet position when current peak starts and target position.

3.3.3 Conductive target

As with helium, a conductive target has an influence in all neon bullet's dynamics. If compared to helium the bullet goes more rapidly from a round shape to the elongated one that gives rise to the backstream described in figure 3.19.

In figure 3.29 is possible to see that the distant target (setup C) is reached by the bullet with medium and high voltage, but there isn't a change in luminosity. Near nozzle exit the bullet speeds up, reaches rapidly the target, stretches and then reduces its diameter to the impact point. For a close target there is a change in luminosity in correspondence of the negative voltage peak and of the second voltage positive peak. With high voltage the bullet shape is losed completely once plasma exits the nozzle, all the space between nozzle exit and target is completely filled by glowing gas.

Current measurements In figure 3.30 ad in table 3.8 there are results for the analysis of current measurements, similar to those done with helium. A current peak is measured only for high voltage with distant target and for medium and high voltage with close target. Starting time of current peak is again precedent to the impact time of the bullet with the target. Interaction distances presented in table are similar to the ones found for helium. The absence of the current peak for medium voltage with distant target could mean that the target is not reached by the charge carrier, even if we see luminosity on the target. With higher voltage the bullet and the charge carrier are more rapid, reach the target and we measure current.

3.4 Argon flow

The third noble gas used it's Argon, it is the one that usually requires higher voltage to be ionized at atmospheric pressure. Argon has a standard atomic weight of 39.948, 1st ionization energy of 15.760 eV and 2nd ionization energy of 27.629 eV. The peculiarity of this gas is its tendency to form filaments of plasma, instead of a large column as seen with helium or neon. Figure 3.31 shows an example where there is a grounded ring made of copper positioned around the outer nozzle, that allows to produce plasma with lower voltage and repetition rate. The pulse repetition rate and the voltage peak value are chosen to observe plasma formation with and without this ring, to see differences between the setups.

Along the production of filaments, argon shows also the tendency to transite from a glow to an arc discharge when a target is positioned near it, as in figure 3.32. As described in chapter 2, when there is a plasma arc there is also large current intensity circulating in plasma and in the target, a condition that has to be avoided in non thermal blood coagulation. Target position in measurement setups C and D is chosen to allow plasma impact without arc transition.

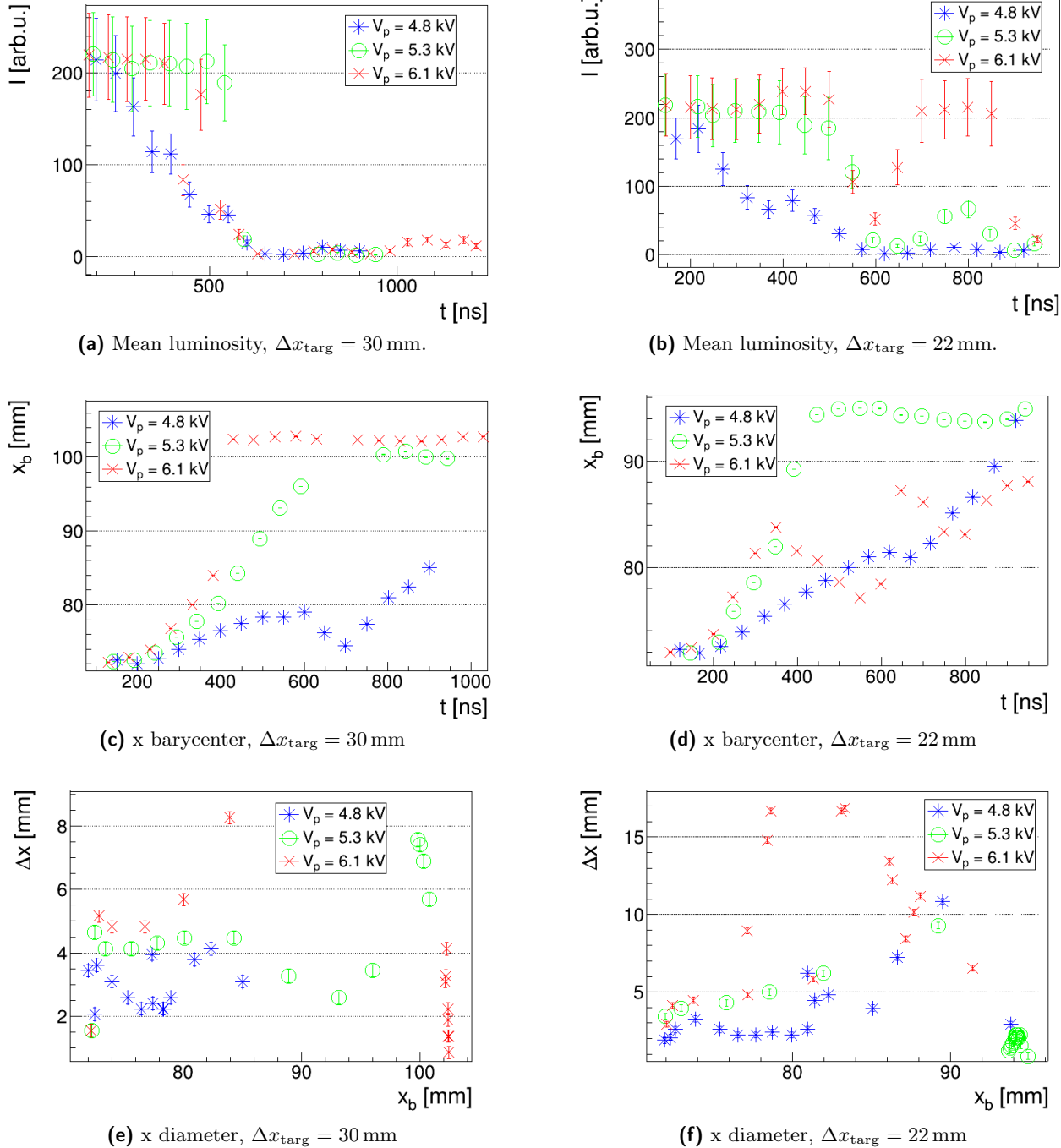


Figure 3.29: Results of the analysis for measurement setup C and D with neon gas, for different peak voltage values.

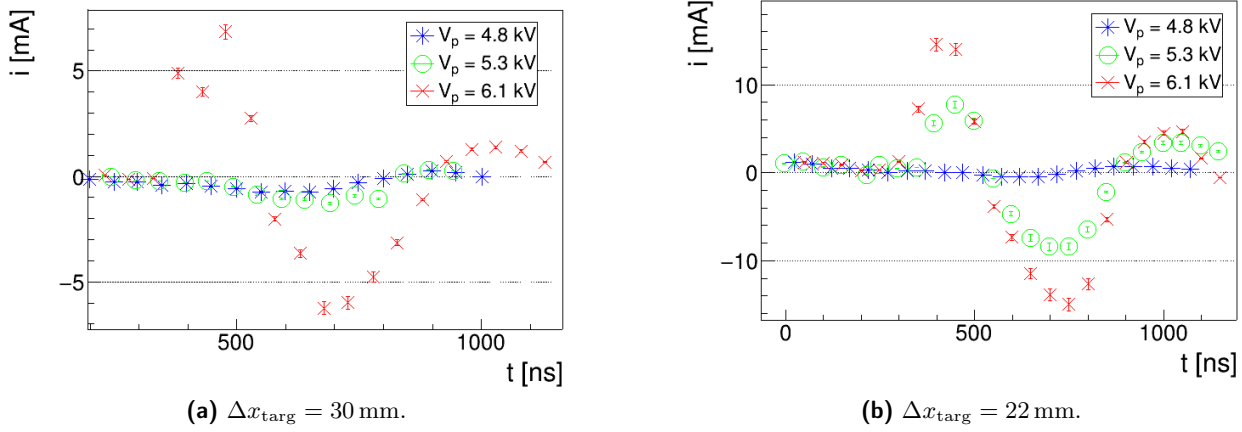


Figure 3.30: Current intensity measured for neon in setups C and D, with different voltage peak values.

3.4.1 Dynamics example

An example of argon plasma propagation can be seen with measurement setup A: argon flow of 2 L/min, presence of the grounded ring outside the nozzle and absence of target. Formation, expulsion and propagation of argon plasma is phenomenologically different if compared to helium or neon plasma, but can always be separated two phases: inside the nozzle and outside it.

Plasma formation Inside the nozzle plasma forms as filaments that start on the electrode and reach nozzle's walls, with different lengths for each frame. There isn't a uniform propagation of those filaments toward the exit, however after a time of 180 ns, every filament covers all the distance between electrode and nozzle exit (10 mm), as in figure 3.33. Under the hypothesis of a propagating front composed by the filament's ends, it would have a velocity of, at least, $v_N = 55.56 \text{ km/s}$.

Plasma expulsion After the time interval where plasma is seen only inside the nozzle, it's possible to observe zones with high luminosity also in air. Plasma is expelled as tiny round shaped formations, separated from each other, as in figure 3.34.

For every frame there are several formations with different positions and diameters. It is possible to study the dynamic of plasma propagation studying the evolution of those parameters. For each frame each formation that presents luminosity over a limit value is isolated. It is possible to count how many formations there are, what are their mean luminosities, barycenter coordinates and diameters, as done with the bullets in helium and neon. Given a frame at a specific time, from those parameters are made histograms and is possible to extrapolate the parameter distribution. For different times, it's possible to compare those distributions, as it's done for barycenter's coordinate x in figure 3.35 as an example.

Given those distributions for every parameter, it's possible to evaluate the mean value for luminosity, barycenter coordinates and diameters at any given time, reconstructing an analysis similar to that presented for other gasses. Results are presented in figure 3.36, where the points are the mean value of the distribution and the error is associated with distribution widths.

The number of plasma formations follows voltage waveform: there are more plasma formations right after the voltage positive peak value and right after the voltage negative peak value. Also average luminosity shows this behavior: there is emission with more intensity right after the positive and the negative voltage peaks, with higher errors during the negative peak, showing that values are more spread around the average value. Barycenter motion in the x direction shows that the distribution propagates during the time interval where voltage is positive and stops when it becomes zero, at a certain distance from the end of the nozzle. It's relevant to point out that the propagation is observed



(a) Picture of argon plasma.



(b) Frame after 120 ns from discharge start.

Figure 3.31: Example of argon discharge in measurement setup A.

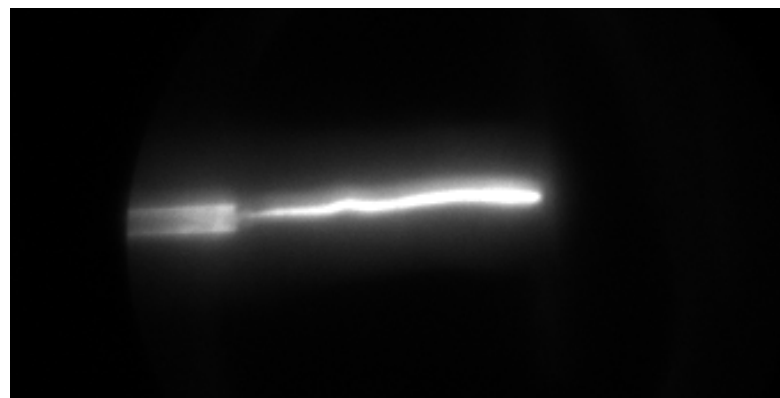


Figure 3.32: Frame of arc discharge with argon and a target positioned 22 mm from the electrode, after 500 ns from discharge start. The arc covers all the gap between electrode on the left and conductive target on the right.

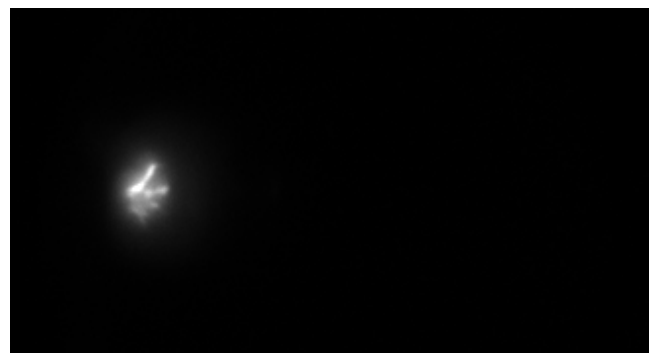
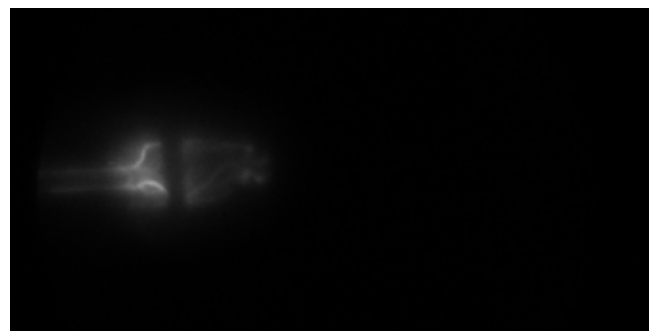
(a) $t = 0 \text{ ns}$ (b) $t = 80 \text{ ns}$ (c) $t = 180 \text{ ns}$

Figure 3.33: Propagation of argon plasma filaments inside the nozzle, measurements setup A.

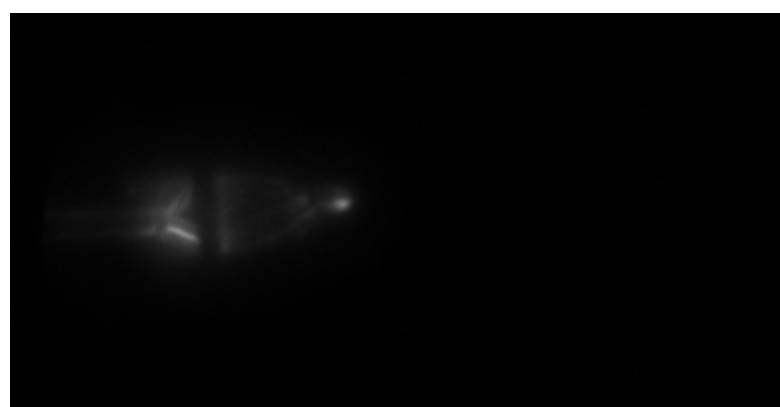


Figure 3.34: Expulsion of argon plasma in air at 220 ns from discharge start, measurements setup A.

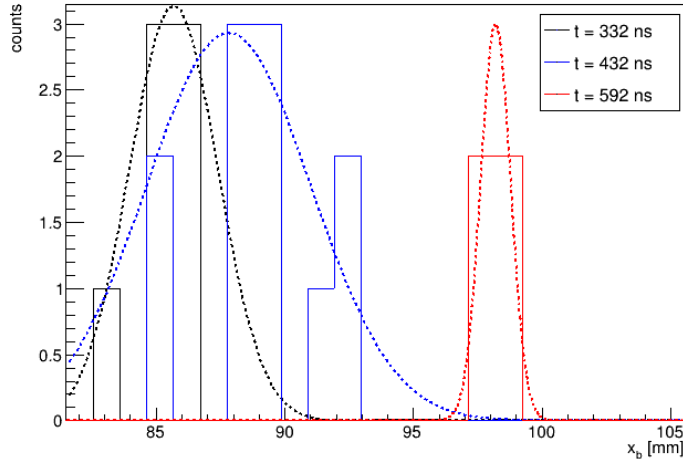


Figure 3.35: Distribution of barycenter's coordinate x , for plasma formations expelled from the source, at three different times, in measurements setup A. For each time, each bin counts how many formations are observed centered at a specific position x_b .

only outside the nozzle, so position values starts around 85 mm, that is the end of the nozzle. During the propagation phase it's possible to estimate a velocity for the mean value of those formations with a fit as shown in figure, resulting in $v_A = 30.16 \pm 3.56$ km/s. Diameters values are presented to show dimensions of plasma formations. Diameter along x and y direction varies in a range between 0.3 and 1.3 mm, with a stretch in the x direction where voltage's absolute value is higher, and a stable value in the y direction around 0.7 ± 0.2 mm.

3.4.2 Absence of target

The grounded ring positioned around the nozzle for measurements sets A and C, phenomenologically, helps the formation of plasma, allowing to produce it with lower amplitude and repetition rate of voltage pulses. The effects of this ring on plasma dynamics is analyzed comparing the expulsion of plasma in setups with or without it, respectively measurements set A and B.

Analysis is done as described before for setup A, results are in figure 3.37, where the voltage waveform is identical to the one presented in figure 3.36. As in setup A, the peak in plasma formation numbers and luminosity is in correspondence of voltage peak values, positive and negative. Interesting thing to note it's that the number of formations is always lower for measurements without the ring, implying that it's expelled more plasma when there is the ring. Baricenter position changes uniformly for both sets, resulting in a velocity of the mean value of $v_A = 47.90 \pm 4.75$ km/s with the ring and $v_A = 39.03 \pm 2.95$ km/s without it. Diameters have an average value higher for set A in both directions, but data is spread a lot for all measurements sets, so it's not possible to note differences outside the error.

Argon plasma dynamics doesn't change behavior introducing the grounded ring on the nozzle, but plasma formations that are expelled reach higher velocities.

3.4.3 Influence of target

In measurements setups C and D is observed plasma formation and evolution with a copper target (the same described before) positioned at 30 mm, respectively with and without grounded ring around the nozzle.

Analysis is done as described before, results are in figure 3.38, where the voltage waveform is identical

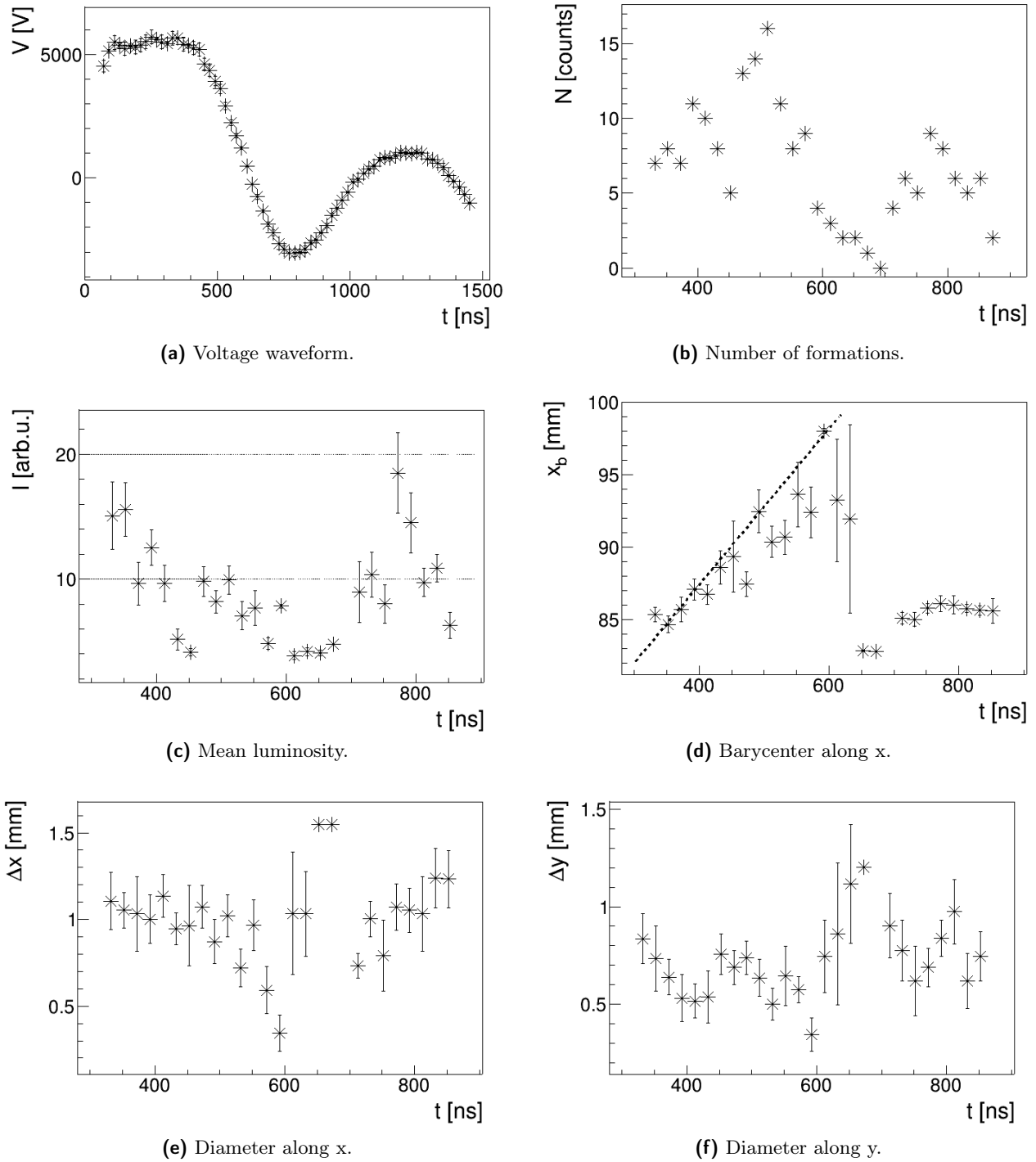


Figure 3.36: Analysis of argon plasma formations, measurements setup A. Every point identifies the mean value of considered parameter between all plasma formations observed at a given time, while the error is associated with the distribution width.

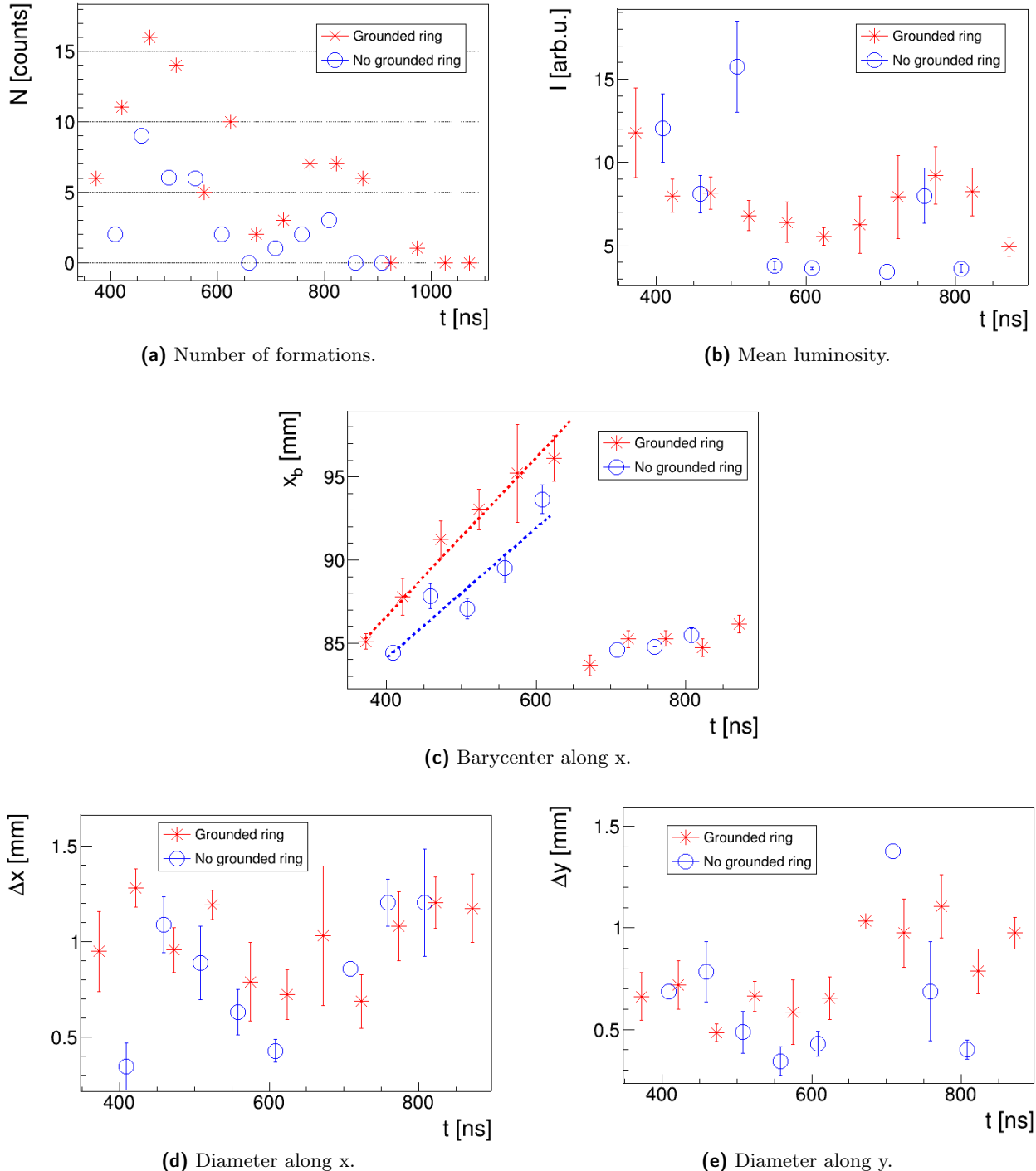


Figure 3.37: Analysis of argon plasma formations, with grounded ring positioned outside the nozzle (setup A) and without it (setup B).

to the one in figure 3.36. For those setup the number of formations, their luminosity and the diameters are not influenced by the presence of the grounded ring. The most relevant difference between those measurements and the ones in setups A and B it's that now with the grounded ring the mean position of formations travels with a velocity lower then the velocity in absence of it. For setup C the velocity is $v_A = 30.49 \pm 4.10 \text{ km/s}$, while for setup D, without the ring, it is $v_A = 61.24 \pm 2.84 \text{ km/s}$.

An explanation could be that plasma is attracted by a conductor at ground potential, when there isn't the grounded ring the target is the conductor at ground potential more close to the electrode, so plasma is attracted by it.

3.5 Hints on bullet propagation model

Formation and propagation of bullets in cold plasma discharges is a phenomenon that still has to be explained, there isn't a specific model that entirely describes it. From measurements shown before it is possible to make some hypothesis and correlate what we observed in terms of plasma parameters such as electron temperature and transport coefficients.

Bolsig+ and electron temperature There are a few softwares that can estimate electron temperature and its transport coefficients. In this work is utilized *Bolsig+*, a Boltzman equation solver that allows to evaluate plasma parameters with different gas temperature and composition [51].

Electron motion in a plasma inside an electric field E is described by the electron energy distribution function in the six-dimensional phase space f . It can be found resolving the Boltzmann equation 3.2, where v is the particle velocity, ∇_v is the gradient in the three velocity coordinates and $C[f]$ represents the change rate of f due to collisions.

$$\frac{\partial f}{\partial t} + v \cdot \nabla f - \frac{e}{m} E \cdot \nabla_v f = C[f] \quad (3.2)$$

Once f is known, it's possible to evaluate the electron temperature T_e of the plasma considering that f should follow a Maxwell-Boltzmann distribution.

The first two moments of 3.2 are, respectively, the continuity equation and the momentum equation, approximated by the drift-diffusion equation, as in 3.3, where Γ is the electron flux, S is the electron source term related to reactions, μ is the mobility coefficient and D is the diffusion coefficient.

$$\begin{aligned} \frac{\partial n}{\partial t} + \nabla \Gamma &= S \\ \Gamma &= -\mu E n - \nabla(Dn) \end{aligned} \quad (3.3)$$

If an high intensity electric fields is applied to the gas, the drift term in electron motion controls plasma dynamics and electron velocity is proportional to its mobility.

Bolsig+ allows to insert reactions that occur inside the plasma, gas temperature and gas composition. Once those input values are inserted it uses approximations on the dependance of f from energy, time and space, to solve the equations shown before and simulate electron temperature and transport coefficients. Those parameters are found as a function of the reduced electric field E/N , where N is the neutral numarical density of the plasma, that is the one of an ideal gas at atmospheric pressure $N = 2.687 \times 10^{25} \text{ m}^{-3}$.

Thys analysis includes four different gases, to simulate the ones used and the main components of air: helium, neon, nitrogen and oxygen. A selection of considered reactions is presented in table 3.9, they are taken from the archive in *LxCat* [52].

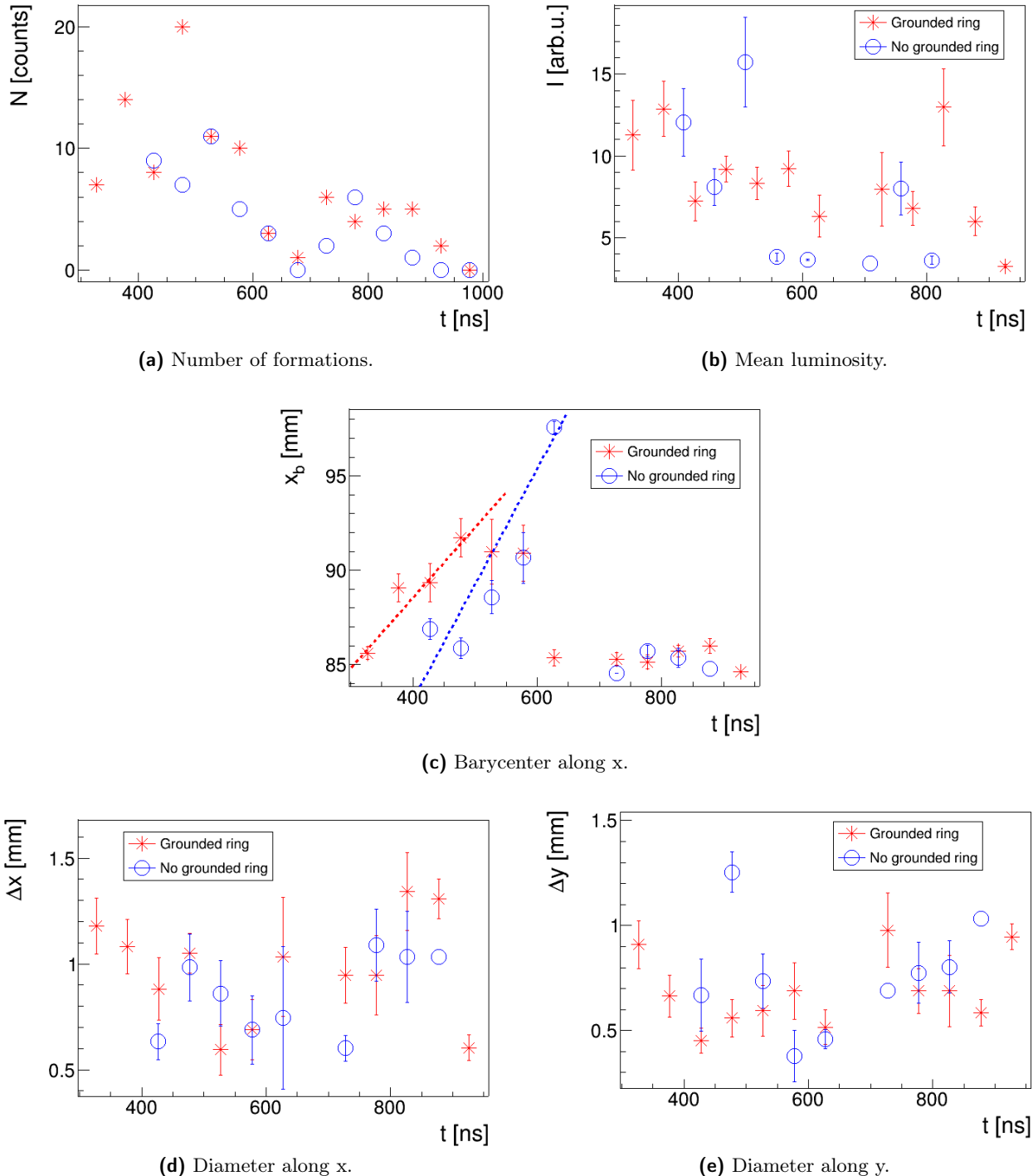


Figure 3.38: Analysis of argon plasma formations, when there is a target in front of nozzle exit, with grounded ring (setup C) and without it (setup D).

Gas	Reaction	Threshold energy [eV]	Description
He	-	-	elastic
	$\text{He} \longrightarrow \text{He}^*$	19.8	excitation
	$\text{He} \longrightarrow \text{He}^+$	24.6	ionization
Ne	-	-	elastic
	$\text{Ne} \longrightarrow \text{Ne}^*$	16.6	excitation (3P2)
	$\text{Ne} \longrightarrow \text{Ne}^*$	16.7	excitation (3P1)
	$\text{Ne} \longrightarrow \text{Ne}^*$	16.8	excitation (1P1)
	$\text{Ne} \longrightarrow \text{Ne}^+$	21.6	ionization
N_2	-	-	elastic
	$\text{N}_2 \longrightarrow \text{N}_2^*$	0.02	excitation (rot)
	$\text{N}_2 \longrightarrow \text{N}_2^*$	0.29	excitation (vib v=1)
	$\text{N}_2 \longrightarrow \text{N}_2^*$	0.59	excitation (vib v=2)
	$\text{N}_2 \longrightarrow \text{N}_2^*$	1.47	excitation (vib v=4)
	$\text{N}_2 \longrightarrow \text{N}_2^*$	6.17	excitation (vib A3 v=1-4)
	$\text{N}_2 \longrightarrow \text{N}_2^*$	7.00	excitation (vib A3 v=5-9)
	$\text{N}_2 \longrightarrow \text{N}_2^*$	11.03	excitation (ele C3)
	$\text{N}_2 \longrightarrow \text{N}_2^*$	11.87	excitation (ele E3)
	$\text{N}_2 \longrightarrow \text{N}_2^+$	15.59	ionization
O_2	$\text{O}_2 \longrightarrow \text{O}^- + \text{O}$	-	attachment (2body)
	-	-	elastic
	$\text{O}_2 \longrightarrow \text{O}_2^*$	0.02	excitation (rot)
	$\text{O}_2 \longrightarrow \text{O}_2^*$	0.19	excitation (vib v=1)
	$\text{O}_2 \longrightarrow \text{O}_2^*$	4.5	excitation
	$\text{O}_2 \longrightarrow \text{O}_2^*$	8.4	excitation
	$\text{O}_2 \longrightarrow \text{O}_2^+$	12.06	ionization

Table 3.9: Selection of reactions used for different gasses. Elastic reactions are momentum transfer reactions; excitation reactions could be rotational, vibrational (it is indicated the starting vibrational quantum number) or electronic.

3.5.1 Ion waves or electron drift

The hypothesis under this study is that bullet visible radiation is emitted by recombination of ions and electrons inside the gas, giving birth to molecules and atoms in excited states that goes rapidly to lower energy levels emitting photons. A model for bullet propagation would have to elaborate a description of the conditions under which ions and excited species are created, how they propagate in space and how the behavior changes in different experimental setup, in agreement with the experimental results shown in this chapter.

For ionization propagation two possible different mechanisms can be considered: propagation of a ionization wave or electron motion.

Ion waves In absence of magnetic fields, neglecting reactions contributing to motion, it is possible to describe ions dynamics as in equations 3.4 [53], where M is the ion mass, n_i its density, γ_i is the adiabatic constant of ion species and T_i is the ion temperature.

$$\begin{aligned} \frac{\partial n_i}{\partial t} + \nabla \cdot (n_i v_i) &= 0 \\ Mn_i \left(\frac{\partial v_i}{\partial t} + (v_i \cdot \nabla) v_i \right) &= en_i E - \gamma_i K_B T_i \nabla n_i \end{aligned} \quad (3.4)$$

Those equations can be linearized considering their equilibrium solution plus a perturbation on every parameter. This perturbation can be expanded in linear plane waves (for detailed calculations see [53]). Imposing also electroneutrality condition ($n_i = n_e = n$), eqautions 3.4 becomes equations 3.5, where all quantities with subscript 1 are perturbations, ϕ is the electric potential relative to the electric field E , ω is the angular frequency of the wave perturbation and k is its wavenumber.

$$\begin{aligned} n_1 &= n_0 \frac{e\phi_1}{K_B T_e} \\ i\omega n_1 &= n_0 i k v_{i1} \\ i\omega M n_0 v_{i1} &= ik K_B (T_e + \gamma_i T_i) \frac{n_0 k v_{i1}}{\omega} \end{aligned} \quad (3.5)$$

The solution of this equation is a wave with speed v_s in equation 3.6, and ion temperature can be neglected compared to electron temperature under our hypothesis.

$$v_s = \sqrt{\left(\frac{K_B T_e \gamma_i + K_B T_i}{M} \right)} \simeq \sqrt{\left(\frac{K_B T_e \gamma_i}{M} \right)} \quad (3.6)$$

Considering also the ionization and recombination contributions there would be a suppression factor that would decrease the amplitude of the perturbation over time and space.

Ultimately if there is a perturbation on the electric field in a plasma, it propagates with a velocity proportional to the square root of electron temperature over ion mass. It is possible that the velocity of those ion waves is comparable with bullets measured velocities.

Electron velocity The second hypothesis to explain bullet propagation is that it is related to the actual motion of electrons inside the plasma, that colliding with ions leads to reactions as explained before.

There are two possible electron velocities values: electron thermal velocity, the speed of a particle at a specific temperature, or electron drift velocity, the speed of a charged particle inside an electric field.

Gas	V_p [kV]	E [kV/m]	T_e [eV]	μ_e [m^2/sV]
He	5.7	190	4.5	0.080
	6.6	220	5.2	0.079
	7.3	243	5.8	0.080
Ne	4.8	160	7.2	0.144
	5.3	177	7.3	0.142
	6.1	203	7.6	0.140

Table 3.10: Plasma parameters with different peak voltage values.

Gas	v_N [km/s]	v_s [km/s]	v_{th} [km/s]	v_d [km/s]
He	37.72	13.42	14.73	15.23
	46.48	14.15	15.53	17.40
	59.80	14.84	16.29	19.41
Ne	34.59	7.30	8.06	23.04
	42.82	7.41	8.18	25.13
	62.92	7.51	8.30	28.42

Table 3.11: Plasma velocities for different voltage peak values, evaluated with parameters in 3.10. v_N is the experimental bullet velocity measured inside the nozzle; v_s is the ion wave velocity; v_{th} is the electron average thermal velocity; v_d is the electron drift velocity.

With electron temperature and mobility, simulated by *Bolsig+*, is possible to estimate the average thermal velocity and the drift velocity as in equation 3.7.

$$v_{\text{th}} = \sqrt{\frac{2K_B T_e}{m_e}} \quad (3.7)$$

$$v_d = \mu_e E$$

Result comparison To give an electric field value as input in *Bolsig+* is possible to consider an electric field uniform in space with a conductive target positioned at 32 mm. In those conditions *Bolsig+* can estimate electron temperature and electron mobility, from them is possible to evaluate ionization wave velocity, thermal velocity and drift velocity, to be compared with bullet velocity in the nozzle. In table 3.10 are presented resulting parameters for helium and neon (compatible with those found [54], [55], [56]), in table 3.11 evaluated velocities.

All estimated velocities are lower than the actual measured velocities, but they have the same magnitude order, especially for drift velocities. Measured velocities are higher for neon bullets compared to helium bullets for the same voltage value, as shown in figure 3.26. This behavior is respected only by drift velocities, because neon has always higher mobility than helium, while other velocities decrease with increasing ion mass. It is possible to compare if the increase in velocity due to increase in voltage value is comparable with the increase of drift velocity. More specifically, the ratio of neon mobility over helium mobility has to be comparable with the ratio of the slopes in figure 3.26 for helium and neon. From the experiment ratio of the slopes is $m_{\text{Ne}}/m_{\text{He}} = 1.60$, while ratio of mobility values is $\mu_{\text{Ne}}/\mu_{\text{He}} = 1.75$. The values are compatible so it is possible to assume that the increase in neon bullet velocities is correlated with the increase of its mobility.

It is not possible to have an exact measure of the electric field with the experimental setup used in this work, however, with the assumption that velocities inside the nozzle are drift velocities, is possible to

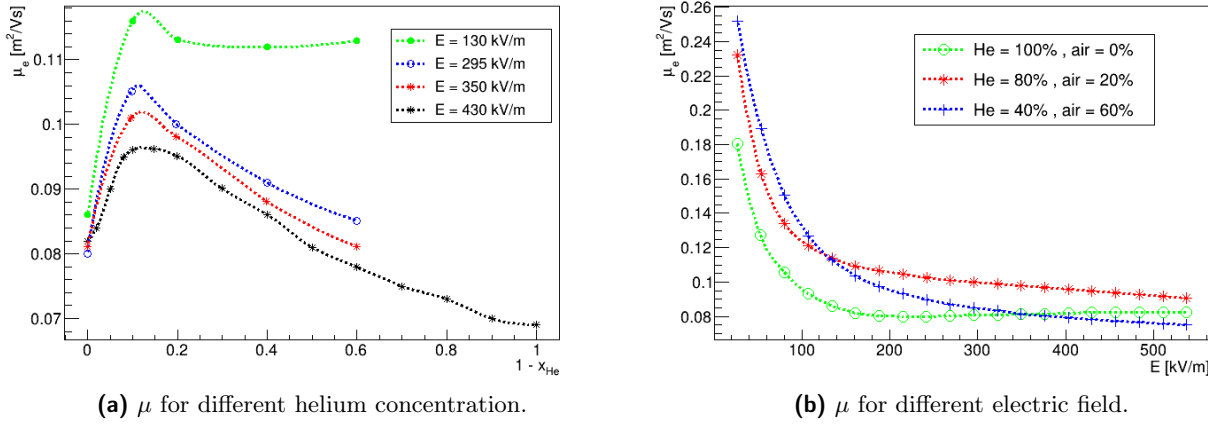


Figure 3.39: Electric mobility values with different electric field and gas composition. x_{He} is helium concentration, $1 - x_{He}$ is air concentration, where air is a gas of 70% nitrogen and 30% oxygen.

have an estimation of the electric field needed to reach those velocities. Electric field intensities would range from 300 to 700 kV/m, plausible values with the voltage values and distances measured in the experiment.

3.5.2 Mobility and velocity

With the assumption that bullet velocity is proportional to electron mobility, it is possible to describe bullet propagation qualitatively, inside the nozzle and in air.

Electron mobility in a gas is proportional to reactions rate relative to the gas, changes in gas composition will change mobility. For this description helium gas will be mixed with nitrogen and oxygen in different proportions, where the ratio of nitrogen to oxygen concentration remains constant at 7/3, similar to the value in air.

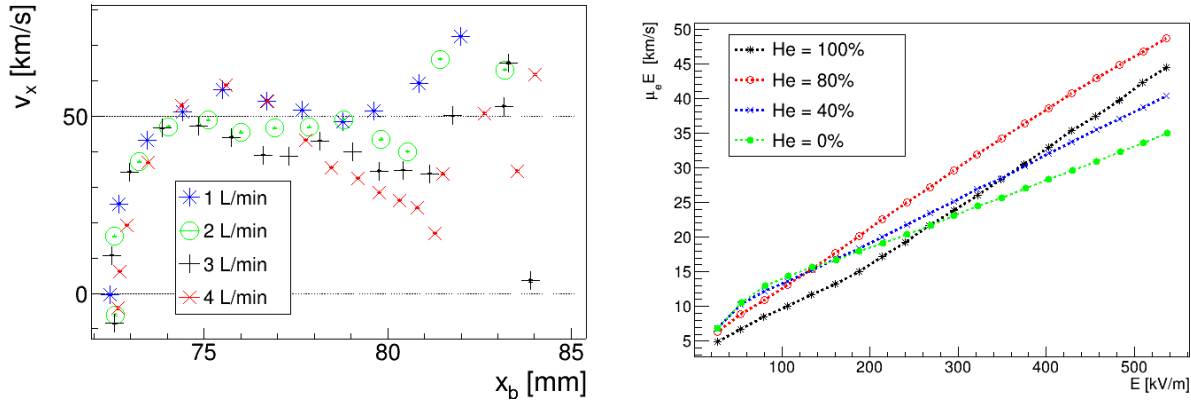
In figure 3.39 there is mobility as a function of the helium fraction with different electric fields, or as function of the electric field with different helium fractions. It's interesting to see that mobility has a peak when a little percentage of air is mixed in helium.

Bullet in nozzle When the bullet propagates inside the nozzle the gas is approximately only composed by helium and the electric field decreases due to voltage decrease and distance from the electrode increase. In those conditions the drift velocity decreases linearly, as in figure 3.40 (b), and in a similar way the bullet decelerates (a). When the bullet meets the air outside, it goes from one line to another in the graph, increasing or decreasing its velocity based on the air composition.

Bullet in air When the bullet meets the air outside gas composition changes rapidly and consequently electron mobility changes. In measurements there is a peak in drift velocity right after nozzle exit, as there is a peak in electron mobility if we add a low percentage of nitrogen and oxygen in helium, figure 3.41. The drift velocity peak is higher for higher values of the electric field, compatible with what is seen from experiment.

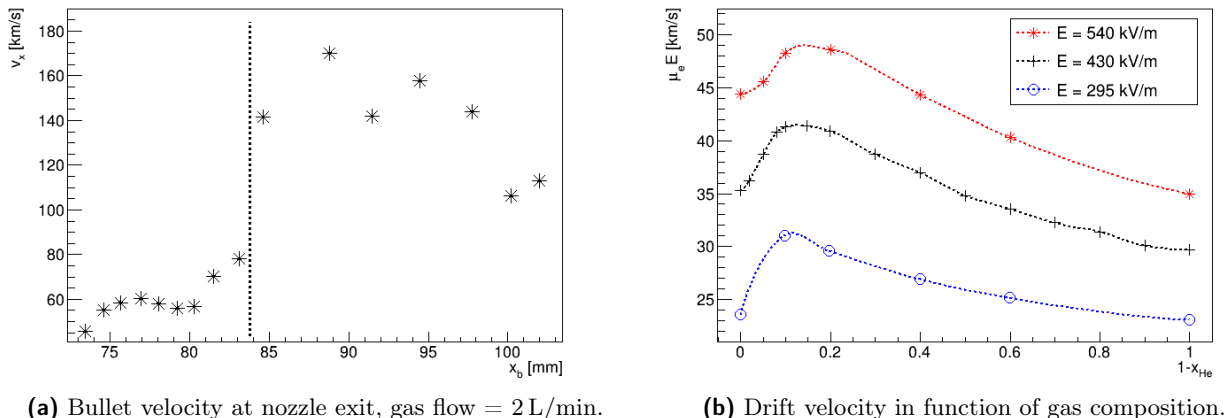
Ultimately, the following conclusions can be made for a free electron inside a plasma in an electric field :

- if the electric field is decreasing in time and gas composition does not change, electron's velocity decreases;



(a) Bullet velocity inside the nozzle for different gas flow.

(b) Drift velocity as a function of electric field.

Figure 3.40: Comparison of bullet and drift velocity inside the nozzle.

(a) Bullet velocity at nozzle exit, gas flow = 2 L/min.

(b) Drift velocity in function of gas composition.

Figure 3.41: Comparison of bullet and drift velocity outside the nozzle.

- electron velocities will be higher for plasma made ionizing neon if compared to a plasma made ionizing helium;
- if an increasing percentage of nitrogen and oxygen is added to a pure gas of helium, the electron velocity increases for small fractions of this gas and decreases for higher fractions.

All those observations can also be made for bullets observed in helium and neon with described measurements. Bullet propagation velocities follow the behaviour of electron drift velocities in a plasma inside an electric field. This analysis shows that electron mobility could be a fundamental parameter to understand the phenomenon of bullet production and their dynamics.

Chapter 4

Plasma spectrum

In various studies the spectrum of plasma DBD discharge in air at atmospheric pressure and ambient temperature has been observed ([57], [58]). It presents peaks relative to reactive species from water, oxygen, nitrogen and its oxides in a wavelength range from 200 to 880 nm.

Reactive species that are thought to be involved in blood coagulation mechanisms are Reactive Oxidant Species (such as hydroxil radical OH) and Reactive Nitrogen Species (derived from nitric oxide NO) [59]. This spectroscopy study is focalized on them and their precursor, i.e. on transitions relative to hydroxil, oxygen and molecular nitrogen.

4.1 Optical Emission Spectroscopy

The source produces plasma from a mixture gas of helium (or neon or argon) and air. Along free electrons, there are ions and species that collides with energetic electrons, and populate excited or metastable states with short lifetime. All reactive species partecipe in different reactions, and also in excitation and de-excitation reactions with consequent emission of radiation. When an electron goes from state p at higher energy to state k of lower energy, radiation is emitted with central wavelength λ_0 . Power emitted by this radiation is given by radiant flux $d\phi_\lambda$ and selecting a solid angle as in figure 4.1, is possible to define radiance L_λ , and intensity I , as in equations 4.1. Intensity for a radiation ultimately depends on $n(p)$, population density for state p , and Einstein Coefficient for the transition A_{pk} that is typical for the transition [60].

$$\begin{aligned}\lambda_0 &= \frac{hc}{E_p - E_k} \\ L_\lambda &= \frac{d^2\phi_\lambda}{dA \cos(\theta)d\Omega} \\ I &= \int L_\lambda d\lambda = n(p)A_{pk}\end{aligned}\tag{4.1}$$

Reactions that emit radiation in visible wavelength in air are vibronic transitions where molecule goes from a vibrational state to another, with a change of vibrational quantum number ν , and/or from a rotational state to another, with change of quantum number J ([61], [62]). When there is a vibrational transition, each line corresponds to different numbers $\nu' - \nu''$, these are transitions well spaced in the spectrum, easy to recognize. Rotational transitions gives birth to bands of peaks not markedly spaced, hard to resolve without an efficient spectrometer.

There are many reactions involving oxygen and nitrogen (see for example [63]), in this study only principal transition observable with our spectrometer are determined, to know dominant reactive species present in the plasma plume.

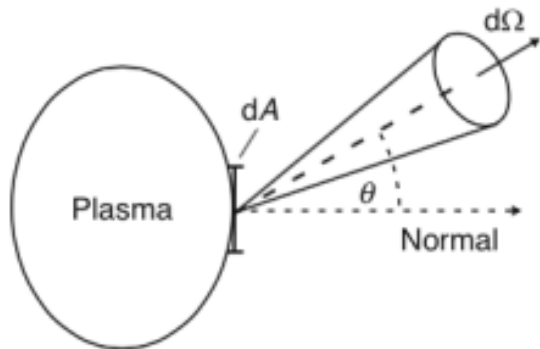


Figure 4.1: Representation of plasma emission from a section of plasma with area dA , under a solid angle $d\Omega$ in a direction θ .



Figure 4.2: Picture of the experimental setup for line recognition. It is possible to see the source, the metal target and the optical setup on the left. Plasma emission is collected by the lens and sent to the spectrometer.

In the first section of this study plasma emission lines are recognized and studied for different discharge parameters. In the second section intensities relative to specific elements are observed for different positions along plasma plume and different gas compositions.

4.2 Line recognition

Prototypes presented in chapter 2 produce equivalent discharge conditions. Plasma emission line recognition is done with prototype **A**, because it was the one that could be moved more easily to reach the spectrometer used in this part of the study. A metal plate is positioned as target at a distance of 10 mm from plasma exit, as in figure 4.2. Helium with a flow set to 2 L/min is used to start the discharge.

The spectrometer is an IsoPlane that separates emissions with different wavelengths with a grating. The spectrometer has a focal length of 320 mm and is equipped with three different gratings: 150, 1200 and 2400 gg/mm, corresponding to different resolutions. Light emitted by plasma is collected through a quartz lens, on the left in figure 4.2, and travels in an optical fiber connected to the spectrometer entry. At the spectrometer exit there is a CCD camera of 2048 pixels and a count limit of 65 000.

Once a grating is chosen, it is possible to set the starting wavelength on the acquisition system and from there the spectrometer takes measures until the end of the CCD, resulting in a specific wavelength interval for each grating. For each measure we select an appropriate acquisition time that allows to observe peaks with a good count number and avoid saturation.

It's important to stress out that, with this measuring method and due to complexity of plasma reactions and composition, it's not possible to extrapolate quantitative considerations between different

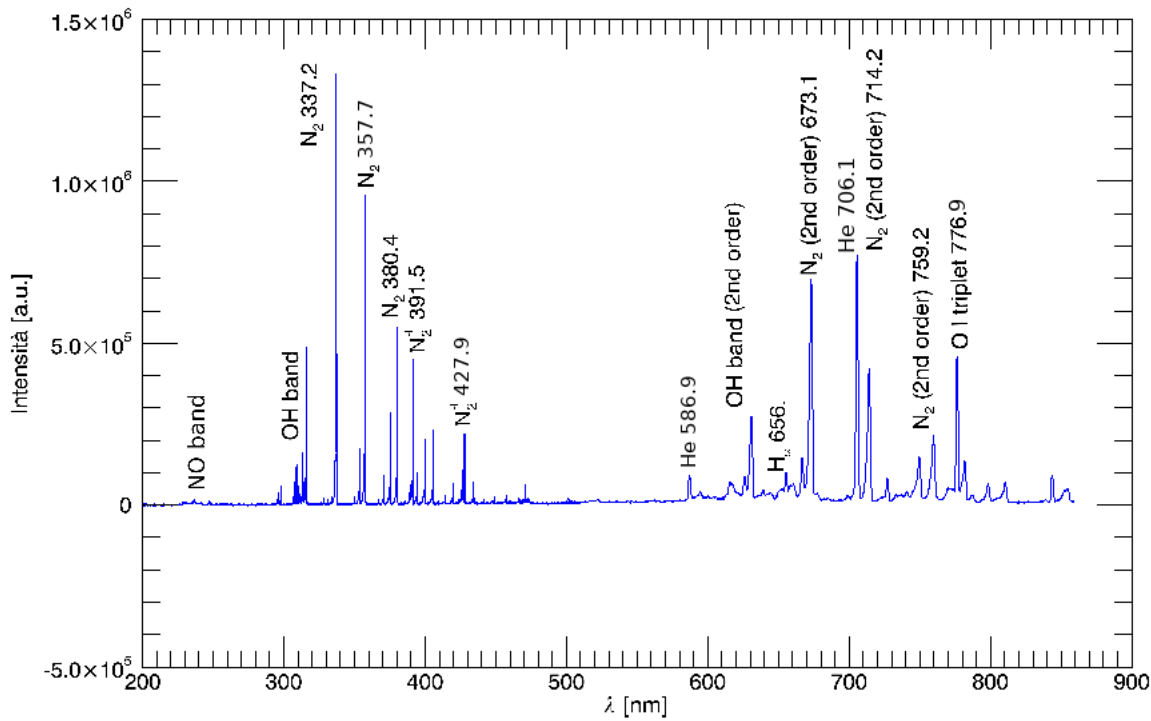


Figure 4.3: Spectrum with helium flow of 2 L/min, pulse parameters of $f = 5$ kHz and $V_p = 6.0$ kV. The emission is collected at the end of the nozzle, where plasma exits in air.

species concentration. However it's possible to recognize the presence of certain species and make some considerations watching spectra variation with different experimental setup.

4.2.1 Emission measurements

The emissions spectrum is observed in a wavelength range from 230 to 800 nm, with standard discharge parameters: $f = 5$ kHz and $V_p = 6.0$ kV. The first measurement is a rapid acquisition with the lowest resolution possible, to see interesting regions and have an idea of required exposition times. After that, the spectrometer does another acquisition with higher resolution for all wavelengths, measuring several spectra. The entire spectrum is reconstructed attaching different spectra, showed in figure 4.3, where are labelled principal transitions. For each measure a background spectrum is also taken, without plasma, to recognize peaks that are not relative to plasma emission.

The spectra are read with IDL routines [64] and analyzed with ROOT *TSpectrum.h* library [65]. In each spectrum each channel is divided by the exposition time of the spectrum, evaluating the count rate at a specific wavelength. White noise contribution is estimated as the average value from a portion of the spectrum that does not present peaks, hence it is subtracted to count rates for each wavelength. In the resulting spectra emission peaks are found with *TSpectrum* functions (where it is possible to set a threshold in height and the general width for lines to be searched) and isolate peaks from background. The exact wavelength for each transition is found with a gaussian fit in an interval that takes into consideration the asymmetry of the peak where it's needed.

As said before, this study is focused on measures related to ROS and RNS, so in lines for NO, OH and N₂.

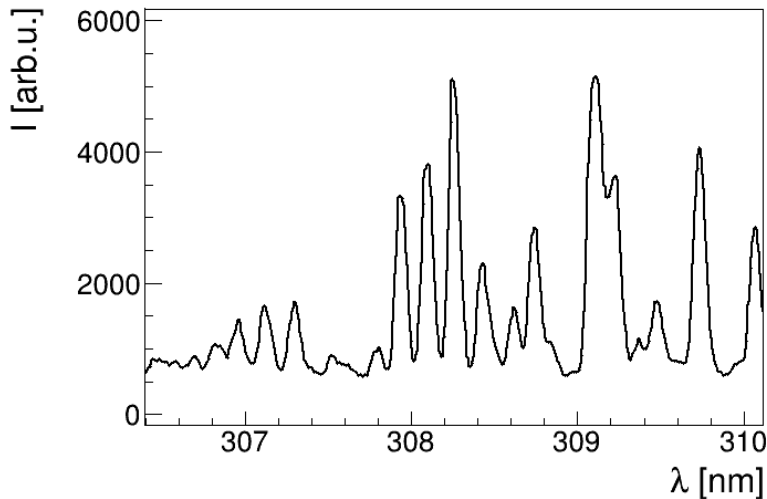


Figure 4.4: Emission spectrum of helium discharge with $f = 5$ kHz and $V_p = 6.0$ kV from 306 to 310 nm. It is possible to see the rotational band of OH.

NO lines In the spectrum there are two doublets for the transition $A^2\Sigma^+ \rightarrow X^2\Pi$ with vibrational numbers (0-0) and (0-1) ([66], [67]), presented in table 4.1. Intensities for the peaks are normalized with maximum value of 1000 for the acquisition, the table shows as the intensities for this transition is very low. Other transitions relative to this molecule have even lower relative intensity and are not observed.

λ [nm]	I [arb.u.]
236.31 ± 0.24	27
237.00 ± 0.15	26
247.02 ± 0.05	28
247.86 ± 0.12	27

Table 4.1: Peaks measured for NO.

OH lines In the spectrum is observed the rotational band for transition ($A^2\Sigma$, $\nu' = 0 \rightarrow X^2\Pi$, $\nu'' = 0$), 13 lines are found [68]. In figure 4.4 a portion of the spectrum in interesting wavelength range for OH, in table 4.2 are presented peak values.

N₂ and N₂⁺ lines Measured spectrum presents several lines relative to nitrogen molecules, including the strongest, for diatomic molecule dinitrogen. The Second Positive System for N₂ transition C³Π → B³Π and the First Negative System for N₂⁺ transition B²Σ → X²Σ are observed. Their positions and peak values are presented in table 4.3 ([69], [70]). For N₂ also a band of multiple rotational lines centered around 336.58 ± 0.01 nm is observed. Some of the peaks are seen in the second diffraction order, where there is more distance between lines. In figure 4.5 are presented two portions of the spectrum showing N₂ lines.

Atomic lines Other lines relative to different elements are presented in table 4.4, they are [71]:

- H_α line corresponding to transition from quantum number $n = 3$ to $n = 2$
- He two of the strongest lines for helium
- O strong line of oxygen

λ [nm]	I [arb.u.]
306.96 ± 0.01	53
307.11 ± 0.01	58
307.29 ± 0.01	62
307.94 ± 0.01	142
308.09 ± 0.01	148
308.26 ± 0.01	161
308.43 ± 0.01	112
308.62 ± 0.01	46
308.74 ± 0.01	137
309.11 ± 0.01	151
309.22 ± 0.01	120
309.45 ± 0.01	36
309.73 ± 0.01	125

Table 4.2: Peaks position and intensity measured for OH in helium discharge with parameters $f = 5$ kHz, $V_p = 6.0$ kV.

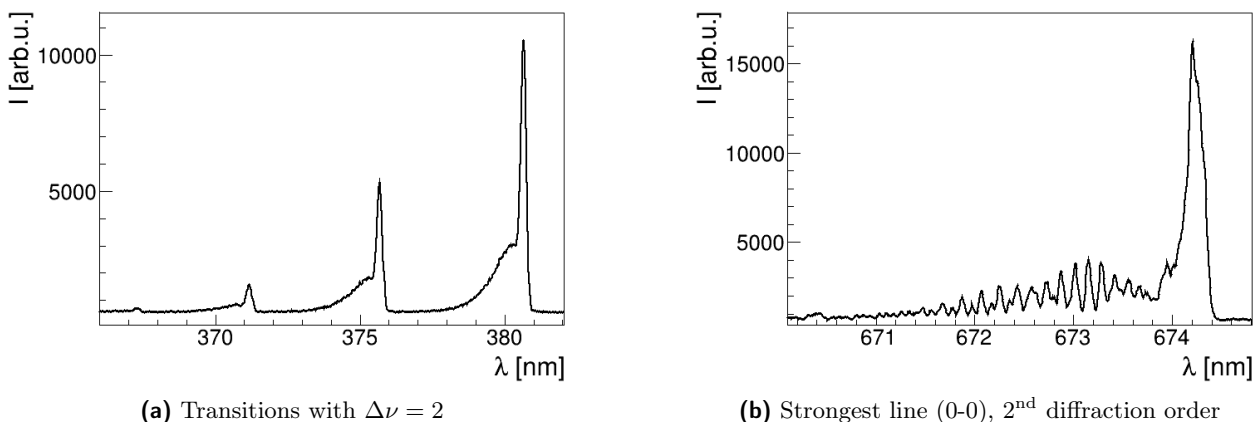


Figure 4.5: Emission spectrum of helium discharge with $f = 5$ kHz and $V_p = 6.0$ kV from 365 to 382 nm (a) and from 670 to 675 nm (b). It is possible to see vibrational and rotational bands for N₂ transitions.

	λ [nm]	I [arb.u.]	$(\nu' - \nu'')$
N_2	316.03 ± 0.01	381	(1-0)
	337.11 ± 0.01	1000	(0-0)
	357.77 ± 0.01	722	(0-1)
N_2	367.22 ± 0.20	58	(3-5)
	371.12 ± 0.04	172	(2-4)
	375.66 ± 0.02	232	(1-3)
	380.64 ± 0.02	423	(0-2)
N_2^+	391.50 ± 0.02	355	(0-0)
	427.45 ± 0.02	180	(0-1)

Table 4.3: Peaks position and intensity measured for N_2 and N_2^+ in helium discharge with parameters $f = 5$ kHz, $V_p = 6.0$ kV.

	λ [nm]	I [arb.u.]
H_α	655.96 ± 0.04	113
He	586.94 ± 0.05	122
	705.56 ± 0.01	649
O	776.89 ± 0.01	393

Table 4.4: Peaks position and intensity measured for H, He and O in helium discharge with parameters $f = 5$ kHz, $V_p = 6.0$ kV.

4.2.2 Pulse settings

Plasma emission intensity is measured with different voltage peak values and pulse repetition rates to understand how discharge settings influence reactive species production.

As seen in chapter 2 for different pulse repetition rates the electric behavior stays constant, however this parameter could still influence species production rate. Pulse repetition rate is related to the energy deposited on the ionized gas, an higher rate implies more pulses in a given time.

Emission spectrum is observed with three different parameter combinations, corresponding to different intensity of the treatment:

- low: $f = 5 \text{ kHz}$ and $\Delta t = 15 \mu\text{s}$
- medium: $f = 10 \text{ kHz}$ and $\Delta t = 10 \mu\text{s}$
- high : $f = 15 \text{ kHz}$ and $\Delta t = 10 \mu\text{s}$

For each setting plasma emission is observed along two different lines of sight:

- position 1: as close as possible to the end of the nozzle, near plasma exit point from the source;
- position 2: close to the target, at 10 mm from plasma exit point, where it collides with target.

Intensities for OH and N₂ species are evaluated collectively for the lines in a specific wavelength range. For OH lines all the rotational band between 306-309 nm is considered. Lines relative to N₂ are separated in those between 335-337 nm (rotational band and (0-0) transition) and those between 368-382 nm (vibrational transitions with $\Delta\nu = 2$).

In figure 4.6 there are measurement results for considered lines.

Intensities for OH decreases drastically increasing the distance from the source, in position 2 values are lower than 0.1% of those from position 1. OH lines for both positions have same intensity with low and medium power setup, while intensity is lower with higher frequency. For both positions there is a similar behavior.

Also N₂ intensities are related to pulse repetition rate: they decrease as the pulse rate increases. Increasing the rate from 5 to 15 kHz intensity values decrease around 60% in position 1, and reach lower values for position 2.

It seems that production of both those reactive species have rates dependant on pulse repetition rates, in particular the intensity of their emission decreases at higher frequencies.

4.2.3 Estimation of plasma temperatures

From diatomic molecule's spectra it's possible to evaluate some parameters that are indicators of plasma's state: rotational temperatures for OH and N₂, T_r , and vibrational temperature for N₂, T_v . These parameters are estimation of the temperature at which thermal energy is comparable to the gap energy between rotational or vibrational state transitions, they can be defined as in equations 4.2 where ν is the vibrational quantum number and I is the quantized moment of inertia of the molecule.

$$\begin{aligned} T_r &= \frac{\hbar^2}{2k_B I} \\ T_v &= \frac{h\nu}{k_B} \end{aligned} \tag{4.2}$$

Rotational temperatures can be considered an estimation of neutral gas kinetic temperature. Vibrational temperature gives an idea of the population of vibrational states, useful to determine chemical reactions inside plasma.

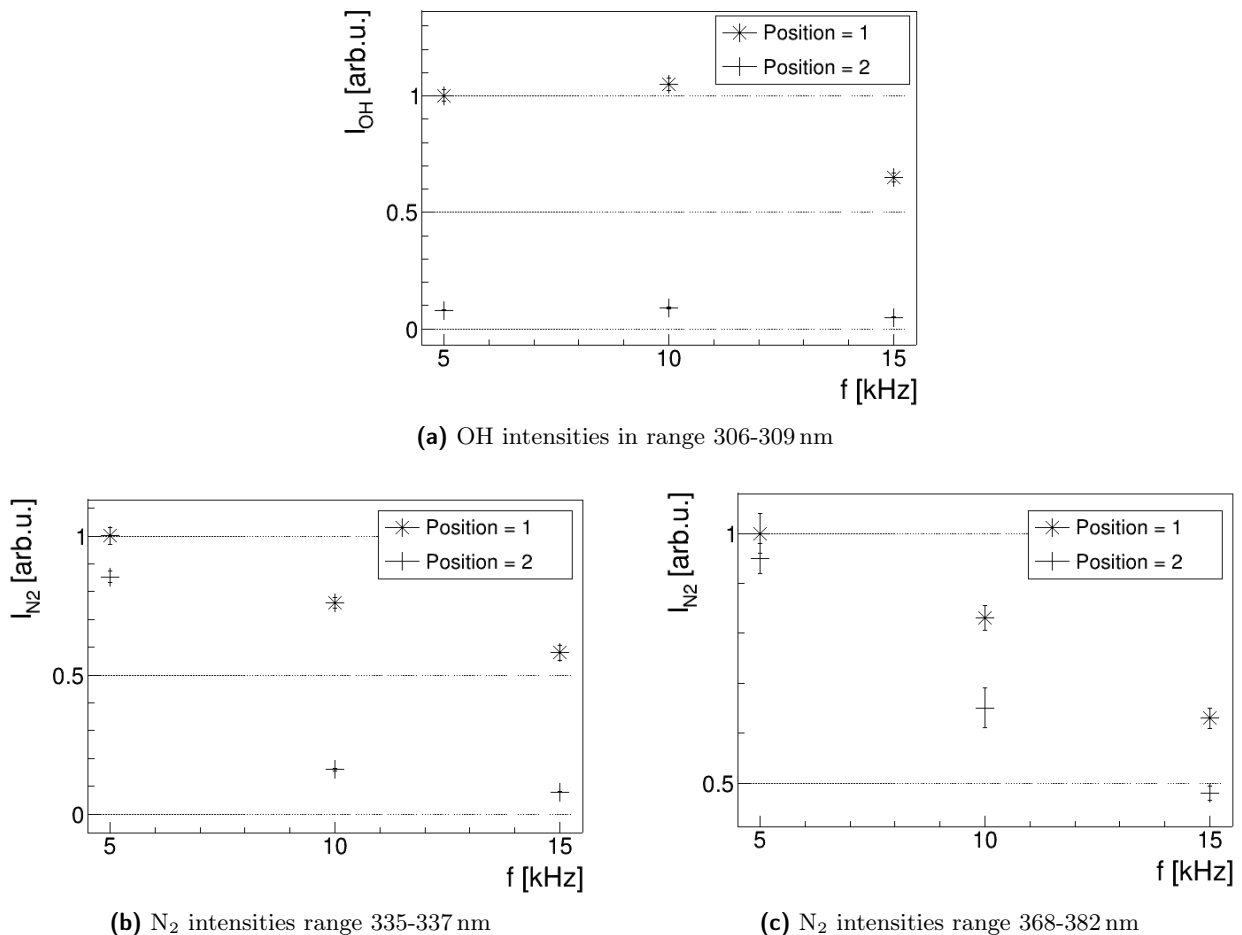


Figure 4.6: Relative intensities of selected portions of the spectrum, for different pulse repetition rates, for position 1 and position 2.

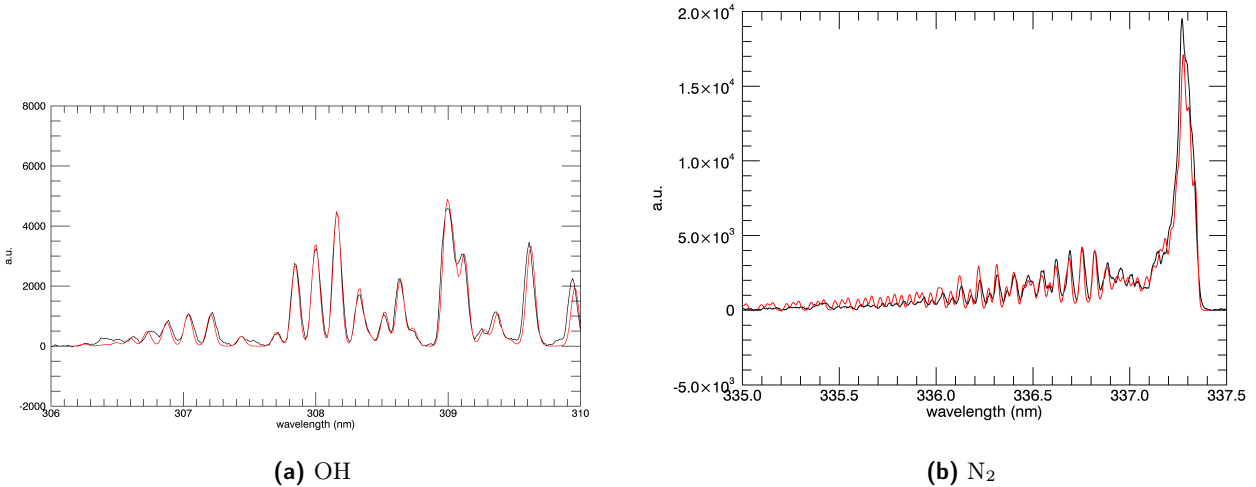


Figure 4.7: Example of optimal spectrum simulation for OH and N₂ considered species.

Rotational temperature for OH and for N₂

In rotational bands the intensity of a transition for a specific wavelength is proportional to the number density population of upper state (equation 4.1), that, considering a Maxwell-Boltzmann distribution, is proportional to the temperature of the species. In equation 4.3 the proportionality is explicated, with D_0 parameter that depends on number of initial molecules, partition function of the rotational state and quantum rotational numbers for upper and lower state, S is the oscillator strength specific for the molecule and E_r depends from a constant defined by the vibrational state and from quantum rotational number for upper state [72].

$$I = \left(\frac{2\pi}{\lambda}\right)^4 D_0 S \exp\left(-\frac{E_r}{k_B T_r}\right) \quad (4.3)$$

As explained before, rotational bands have many lines, not all distinguishable with the spectrometer used in this work. An approach to temperature estimation is to simulate spectra with different temperatures and to minimize differences for measured spectrum ([73]). In a predetermined range of temperatures spectra with different temperatures are simulated, where each line is a gaussian peak with its width that takes into consideration broadening due to thermal motion, Doppler effect and measure resolution. For each spectrum the mean square difference is evaluated and the temperature associated with the minimum difference is chosen as the one relative to the spectrum. The error is estimated taking an upper and a lower limit where the mean square difference is larger than 5% of the minimum value. An example of the spectrum is shown in figure 4.7, while resulting temperatures are shown in figure 4.8.

Estimated temperatures are compatible with each other, for each distance and for each pulse setup. It's then possible to evaluate a mean value for the species, that are $T_{r,\text{OH}} = 352 \pm 38$ K and $T_{r,\text{N}_2} = 321 \pm 41$ K, compatible with each other, and that, as said before, can be taken as an indicator of kinetic temperature for neutral species, so as temperature of the fluid. Those temperatures are higher than room temperature, but they are compatible with the definition of cold plasma.

Vibrational temperature for N₂

Given a set of vibrational transition lines with defined $\Delta\nu = \nu' - \nu''$, their relative intensities are correlated to each other, with a proportionality that involves vibrational temperature [70]. With peak intensities estimated for a given transition can be made the Boltzmann graph shown in figure 4.9 (a),

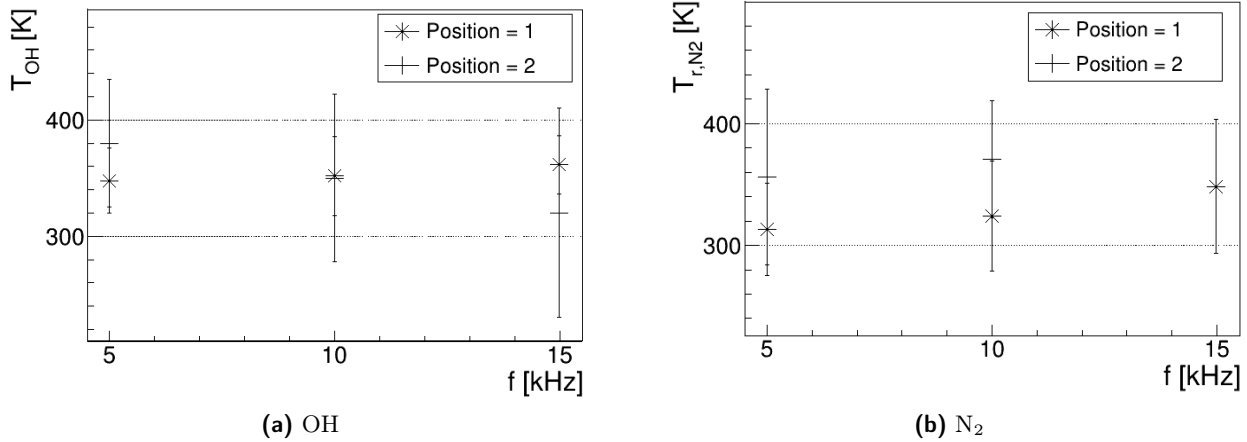
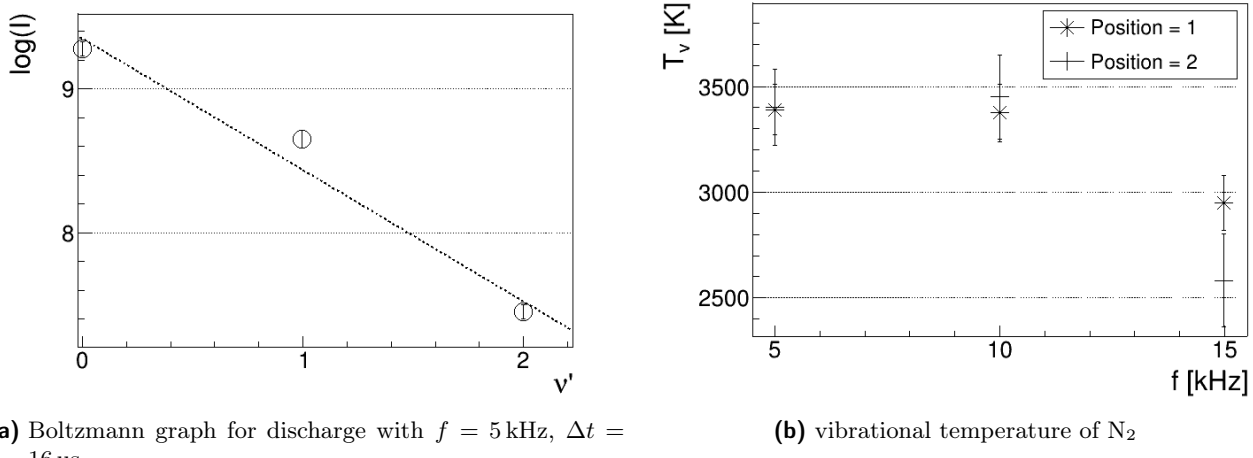


Figure 4.8: Estimation of rotational temperature of OH and N₂ molecules, for different parameters setup and positions.



(a) Boltzmann graph for discharge with $f = 5$ kHz, $\Delta t = 16$ μ s

(b) vibrational temperature of N₂

Figure 4.9: (a) Boltzmann graph made from N₂ vibrational transition intensities for helium discharge with $f = 5$ kHz and $V_p = 6.0$ kV, in position 1; (b) vibrational temperatures of N₂ molecule for different pulse parameters settings and emission measured from position 1 and 2.

for each experimental condition. From the Boltzmann graphs T_v can be evaluated as in formula 4.4.

$$\log(I(\nu')) = S\nu'' + I_0 \quad (4.4)$$

$$T_v[K] = \frac{10^4}{3.57 \cdot S - 0.03}$$

Results are in figure 4.9. For this parameter values are compatible with each other at low and medium power pulse settings with a mean value of $T_v = 3405 \pm 154$ K, while a lower temperature is found for high power pulse settings $T_v = 2781 \pm 322$ K. It seems that with an higher pulse repetition rate there is lower concentration of excited N₂, produced with lower energy.

4.3 Line intensity analysis

The second phase of this study is dedicated to measurements of plasma emission intensities at different positions along the plasma plume and with different gas composition.

For this study are used a portable mini spectrometer and source prototype **B**, with an experimental setup similar to the one in chapter 3.

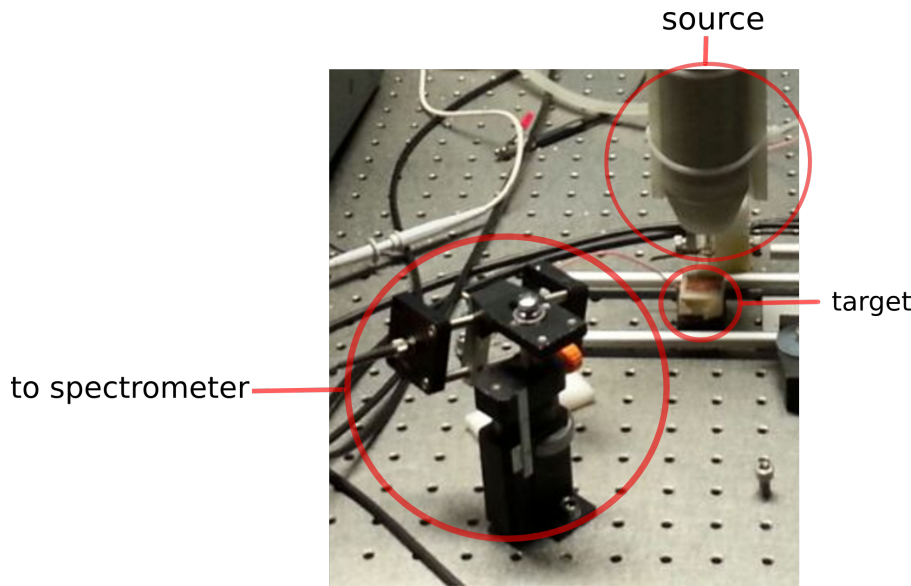


Figure 4.10: Picture of the experimental setup for intensity measurements. Spectrometer's lens on the left is focalized on the plasma plume, mounted on a support with variable height.

4.3.1 Experimental setup

In figure 4.10 can be seen the source and the lens focalized where plasma forms, mounted on a support with variable height. The source mounts the glass nozzle used in chapter 3, allowing to observe emission also inside it. A conductive target is placed at 10 mm from nozzle end.

It is used a mini spectrometer *Hamamatsu C10082CAH*, with resolution of 1 nm, spectral range from 150 nm to 850 nm and a CCD sensor *S10420-1106* with 2048 pixels. The efficiency of the spectrometer for different wavelengths is evaluated with measurements of emission from a lamp with known emission spectrum. With this calibration is possible to convert the number of counts in the number of photons emitted by plasma for each wavelength.

Helium, neon or argon are used to produce plasma, spectra from those three gasses is shown in figure 4.11. Given the low resolution of this spectrometer, it is not possible to identify all the peaks that are observed. Each spectrum presents the same emission lines and, in addition, lines relative to the element used to start the discharge. It is possible to identify four wavelength ranges relative to four elements:

- N₂ lines from 320 to 480 nm: one singlet and several doublets relative to the SPS described before in this chapter;
- one He line at 706.6 nm, observed only for helium plasma;
- Ne lines from 410 to 780 nm, several lines observed only for neon plasma with intensity generally higher than N₂ lines;
- Ar lines from 660 to 850 nm, several lines observed only for argon plasma.

Emission for different elements is evaluated selecting, for each element, some of the higher peaks in all spectra between those observed:

- N₂ : three lines centered at 353.6 nm (transition (1 – 2)), 380.5 nm (transition (0 – 2)) and 405.9 nm (transition (0 – 3));
- He : one line at 706.6 nm;
- Ne : one doublet at 638.3 nm and 640.6 nm, a single line at 703.5 nm and a single line at 725.5 nm;
- Ar : three different lines at 696.5 nm, 763.5 nm and 811.5 nm.

4.3.2 Position

The experimental setup allows to measure plasma emission at different heights along the nozzle axis, emission intensity evaluated in four different positions:

- -5 mm, inside the nozzle
- 0 mm, at the end of the nozzle
- 5 mm, between nozzle and target
- 10 mm, right before target position

Results are in figure 4.12. Total intensities are normalized to compare emissivity variation for different positions, while relative intensities are divided for the respective total intensity. With helium emission is lower inside the nozzle, increase at the exit and decreases slightly moving towards the target. For other gasses emission decreases increasing distance from the source. For every gas, emission from N₂ increases until it reaches a constant value. Lines from specific gasses decreases distant from the nozzle, with slope different for different gasses. It's interesting to note how neon emission decreases linearly, while N₂ emission increases and it's an effect that is observed visually on the plume: going from the nozzle to the target, plasma colour goes to red (neon emission) to violet (nitrogen emission).

It can be concluded that inside the nozzle the emission depends from the gas used to start the plasma, going outside the emission due to nitrogen species becomes dominant in the discharge.

4.3.3 Gas composition

Relative intensity for selected lines is analyzed for different gas composition. Helium is mixed with argon or nitrogen using specific flowmeters, that allow to add up to 0.2 L/min, with resolution of 0.01 L/min. With an helium flow to 2 L/min is possible to have gas mixtures where argon and nitrogen have a maximum percentage of 10%.

The spectrometer is pointed at the end of the nozzle and collects spectra for three different gas concentrations, measuring intensities shown in figure 4.13.

When nitrogen is added to the gas, total emission intensity lowers, while nitrogen emission does not change. It is possible that the increase in nitrogen concentration is too low if compared to the quantity naturally present in air and consequently there is not a significative increase of nitrogen emission at the end of the nozzle. In this position the gas is a mix between the gas used to start the discharge and air, where nitrogen is approximately the 70% of air. The percentage of gas in air is a function of the gas flow, for example it is possible to hypotize that at the end of the nozzle the percentage of discharge gas and air is equal. With a gas flow of pure helium, nitrogen would be the 35% of the total gas density. If the helium flow is substituted with 10% of nitrogen and 90% helium, as in the experiment condition, nitrogen would be the 40% of total gas density. If the relative emission of nitrogen is proportional to the fraction of nitrogen in the gas, the increase in the emission would be a value around 5%, an increment that could be not resolvable with the apparatus used in this experiment. Further measurements of nitrogen emission could verify this hypothesis and, in that case, they could be used to estimate nitrogen percentage for different positions inside the nozzle.

When argon is added to helium, total emission intensity increases, while relative emission from elements other than argon decreases slightly. It means that the only variation when there is a percentage of argon is that the emission relative to this element adds to the emission of helium and the emission relative to other elements stays unchanged.

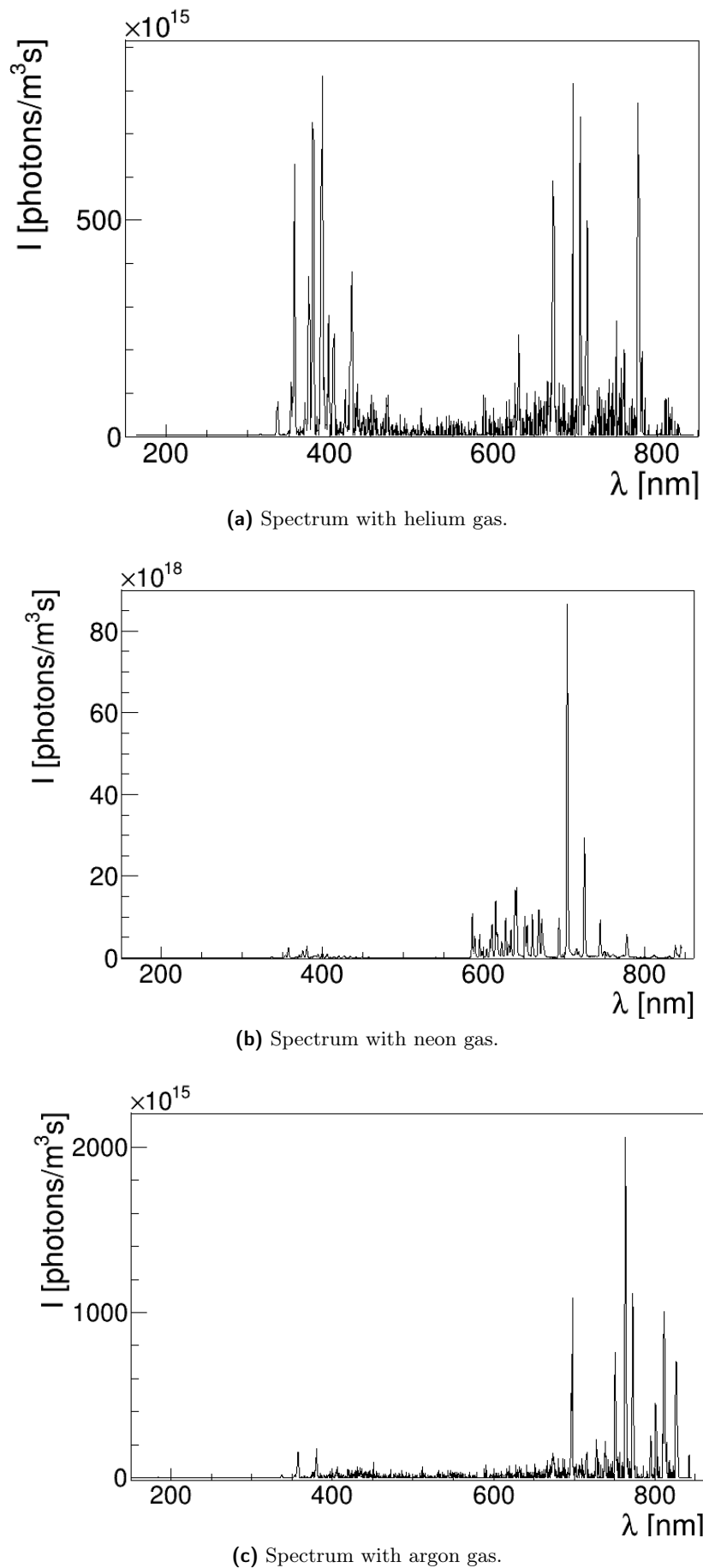


Figure 4.11: Plasma emission spectrum measured at the end of the nozzle, with different gasses used to start the discharge.

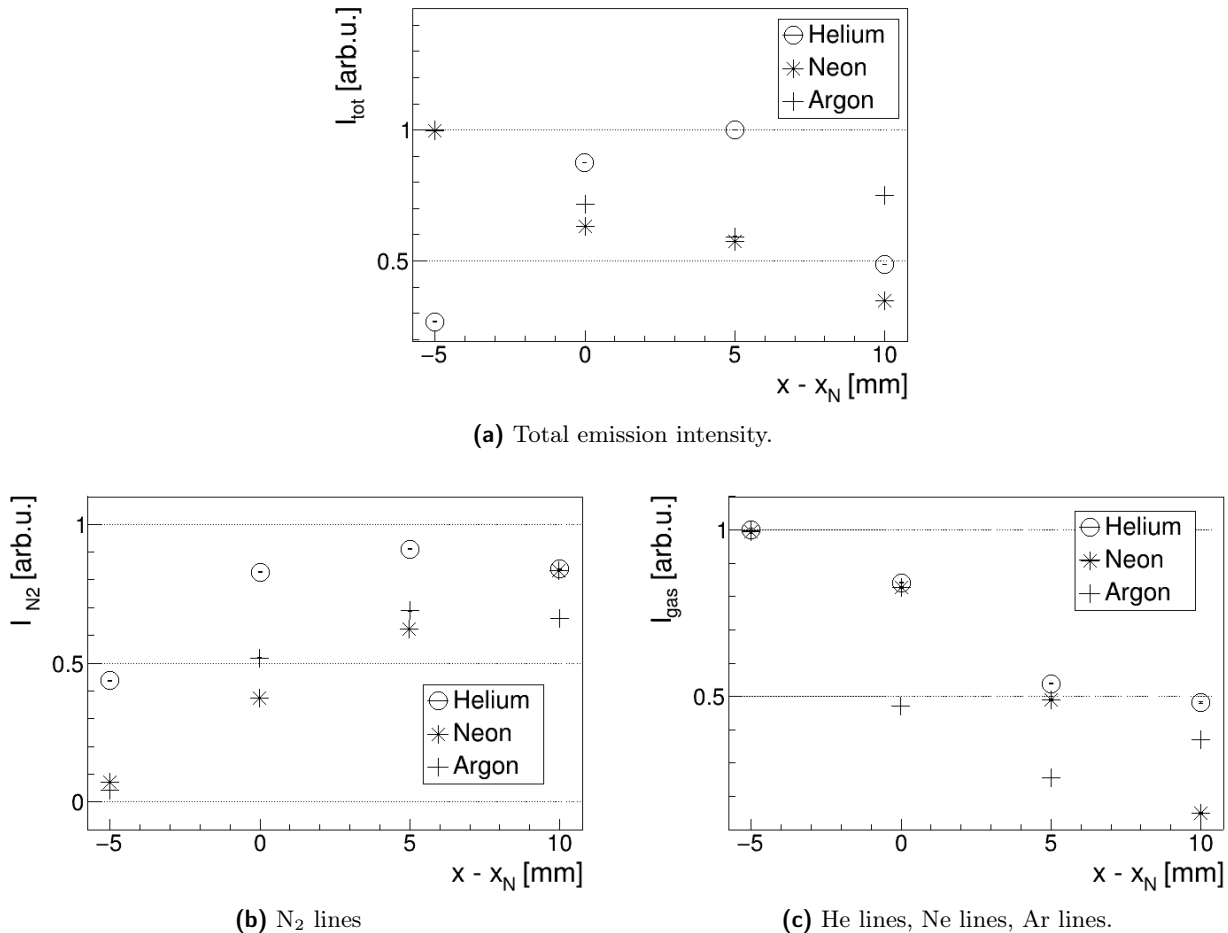


Figure 4.12: Axial profile of total intensities (a) and relative intensities for selected portions of the spectrum (b-c), with different starting gas. At 0 mm the lens points at the end of the nozzle, at 10 mm at a metal target. Relative intensities in (c) are for lines corresponding to the element that used as starting gas. Relative intensities take into consideration spectrometer's efficiency and total emission for each position.

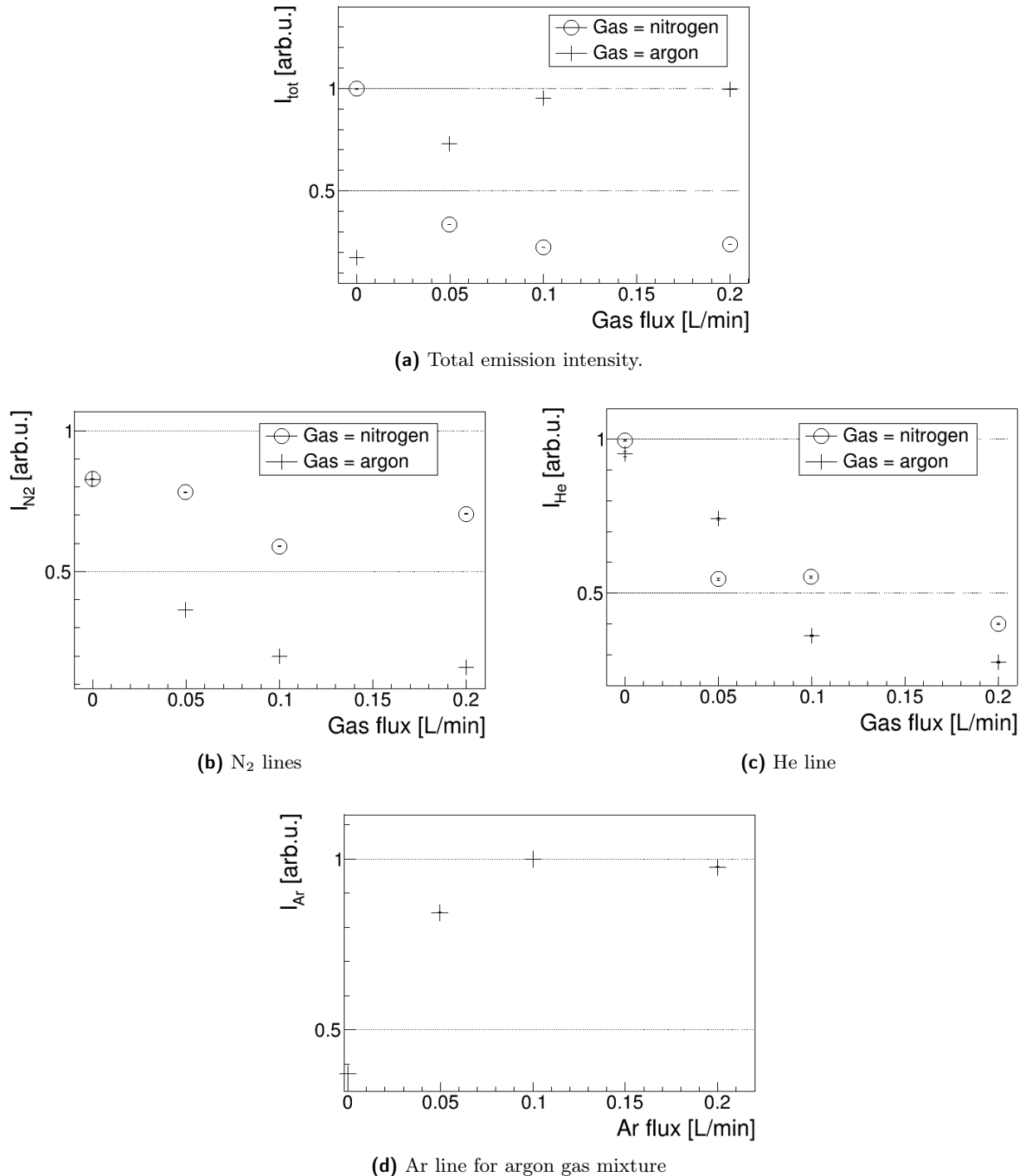


Figure 4.13: Behaviour of total intensities (a) and relative intensities for selected portions of the spectrum (b-c-d), changing the composition of the gas. A flow of 0.2 L/min corresponds to the 10% of the total gas flow. Relative intensities take into consideration spectrometer's efficiency and total emission for each gas mixture.

Chapter 5

Plasma power estimate

Direct application of plasma leads to deposition of accelerated particles on target. For non thermal blood coagulation it's fundamental that on biological tissues that a temperature increase due to this application must be below dangerous limits.

With the supposition that the main heating mechanism of our source is by convection, it is possible to estimate heat transfer rate, i.e. power, due to plasma application on a target. During this work only inorganic targets are utilized, while PCC will be applied to samples of blood and to living subjects, where heating effects are different if compared to inorganic matter. Heat transfer in living biological tissue is a complicated combination of thermal conduction, convection, perfusion of blood and metabolic heat generation [74]. The hypothesis behind the estimate of plasma power in this work is that the interaction between heat transfer mechanisms in biological tissues and heat deposition mechanism of our source is negligible. Under those conditions, with this power estimate will be possible to evaluate the temperature increase due to plasma application on every target once their thermal characteristics are known (for a review of thermal conduction parameters in biological tissues see [75]). Even if the studied case is particular and has many limits, this analysis gives a rough estimate of plasma power dependencies from application parameters such as pulse repetition rate or distance between source and target.

5.1 Experimental setup

Plasma heat power is estimated measuring how much temperature increases with the application of plasma on a target with known heat capacity. The use of a thermocamera allows to study target's temperature profile in its entirety, visualizing also heat conduction on target's borders. An object at thermal equilibrium in a temperature range around 300 K emits radiation in the long-wavelength infrared region (from 8 to 15 μm). This radiation can be collected and its intensity measured by a bolometer, evaluating the temperature of the object from its infrared emission, as in common thermal cameras ([76]). The detector more used is an uncooled microbolometer VOx with an array of pixels as in figure 5.1. Incident radiation strikes a material that has an absorption peak in infrared wavelength, temperature increases changing the electrical resistance of the circuit and the resulting current intensity is measured and associated to collected radiation intensity.

Camera The target is observed by a termographic camera *FLIR A655sc* ([77]) with a spectral range of 7.5 – 14 μm , resolution 640×480 and detector pitch 17 μm , equipped with a lens with focal 41.3 mm (field of view 15°). Temperature evolution is a phenomenon with characteristic time of several seconds, to have a reasonable resolution frame rate acquisition is set at 2 FPS.

The temperature conversion between intensity of the radiation and temperature is done by *FLIR* software, setting the appropriate emissivity.

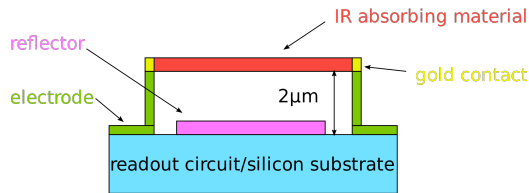


Figure 5.1: Representation of pixel in a microbolometer detector. When incident radiation arrives on the pixel, temperature increases and electric resistance of the circuit changes, giving rise to a current intensity proportional to radiation intensity.

Source The source is the latest one, prototype **B** in chapter 2, at different pulse repetition frequencies f and voltage peak values V_p . Plasma formation and deposition it's not a continuos phenomenon, it happens in correspondance of voltage pulses, with a characteristic time around $1\text{ }\mu\text{s}$, see chapter 3. Given a time interval, f defines the number of pulses that arrives in that interval.

The gas used to produce plasma is helium, with flow of $2\text{ L}/\text{min}$.

Target The target is an aluminium disk, with radius 7 mm and height 1 mm , on a plastic support with width 5 mm . Aluminium has specific heat capacity $c_p = 897\text{ J/kgK}$ and density $\rho = 2700\text{ kg/m}^3$, corresponding to target heat capacity $C = 0.373 \pm 0.005\text{ J/K}$.

Target is positioned at a distance of 210 mm from camera lens. At those conditions, once the image is on focus, pixel to pixel distance on acquired frames is $86.4\text{ }\mu\text{m}$.

To verify relation between power and application distance the target is positioned at three distance values from the en of the source head: 5.5 , 7.5 or 9.5 mm .

Measurements procedure Ultimately measurements are done with different voltage pulse repetition frequencies f , voltage peak values V_p and distances between target and source d . Once those parameters are set, the measure follows an approximative timeline:

- acquisition of at least 4 frames for background evaluation in 2 s
- start of gas flow for a minimum of 5 s
- start of the discharge for a minimum of 30 s
- stop of the discharge and acquisition with only gas flow for 5 s
- stop of gas flow

Start and end time for those phases can be observed directly from measures.

5.2 Temperature profile

Every frame gives information on the temperature of every pixel of acquired image at a given time, as in figure 5.2. To find the interested temperature difference, background temperature before discharge is evaluated as the average value acquired before gas opening and subtracted to pixel value in other frames. In a given direction the temperature profile is shown in figure 5.2.

Source is pointed to target center, for frames acquired with the discharge can be seen clearly where the temperature rises and can be estimated the application position. A square window with edge 15 mm si centered around the point with maximum temperature, to see the temperature increase on all the target. A gaussian interpolation inside the square allows to find the center position, compatible in each measurements set, at coordinates $x_c = 25.06 \pm 0.20\text{ mm}$, $y_c = 21.17 \pm 0.20\text{ mm}$.

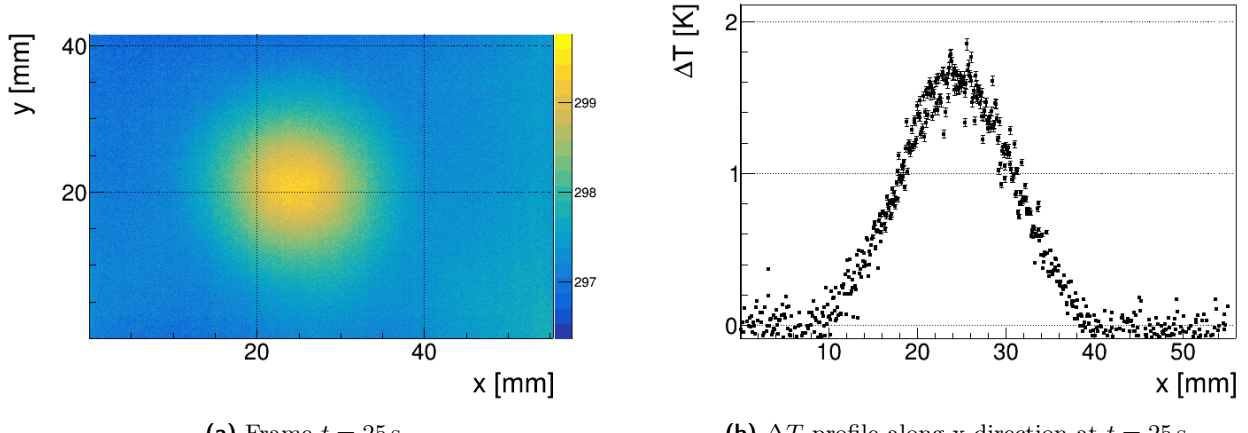


Figure 5.2: Example of measurement during discharge with parameters $f = 5\text{ kHz}$, $V_p = 7.2\text{ kV}$ and $d = 5.5\text{ mm}$.

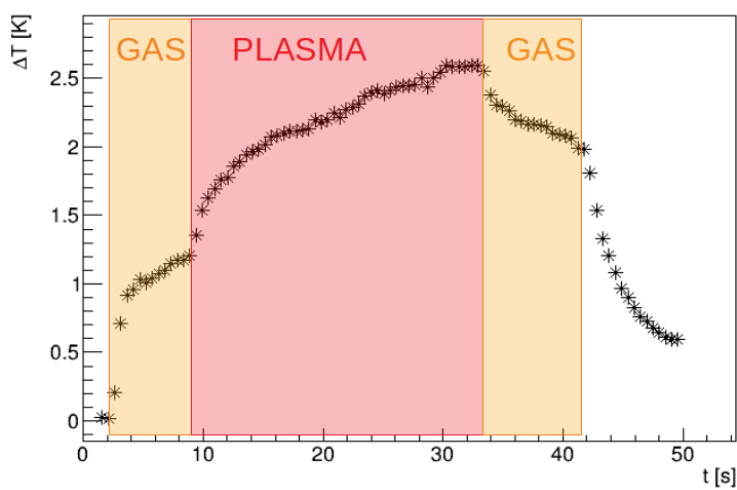


Figure 5.3: Average increase in temperature for every frame at different times, on a square around the target. There are three phases highlighted: gas phase before source activation, plasma phase and gas phase after source power off.

It's interesting to note that when there is only gas flowing on the target, temperature increases radially from the center, in an area larger than the target area, while when there is plasma, temperature increases rapidly in an area compatible with the target dimensions. It's possible that gas before ionization creates a gas layer with a radius larger than the target radius, but considering temperature increase only around the target it doesn't give problems in heat power evaluation due to discharge.

From each of those frames the average temperature difference and its evolution are evaluated as shown in figure 5.3. This graph allows to extrapolate time intervals for gas flow and discharge: where temperature changes rapidly there is gas opening, source activation, discharge end and gas flow stop. In figure 5.4 an example of how temperature profile changes during discharge.

5.3 Power estimation

During the plasma phase, temperature increase in target can be defined as the sum of power deposition plus thermalization contributions (see [78]), as in equation 5.1, where m is the mass of the portion of target considered, c_p is aluminium specific heat capacity, P is power deposited by plasma on target,

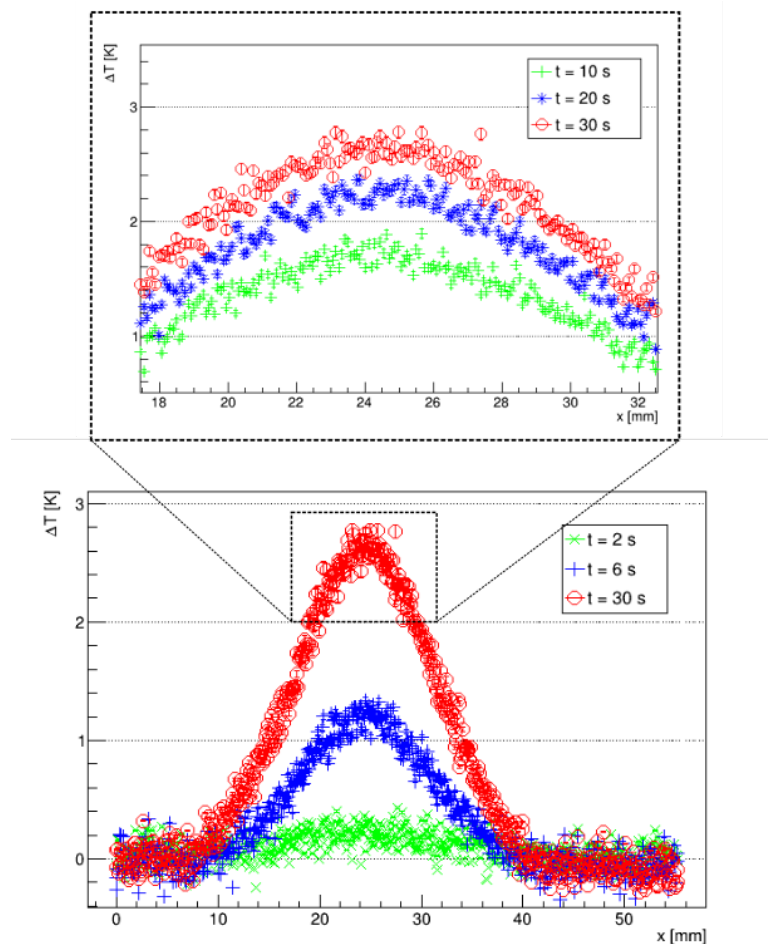


Figure 5.4: Evolution of temperature profile in x direction, with a zoom on the region around the target, for different times and phases: $t = 2$ s before gas opening, $t = 6$ s after gas opening and before discharge, $t = 10, 20, 30$ s during discharge.

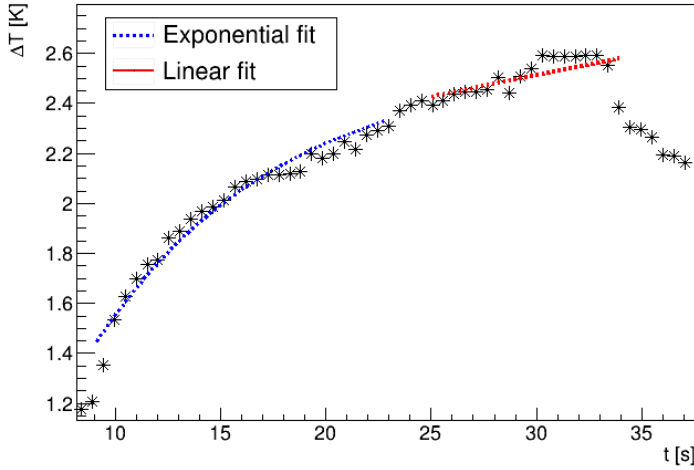


Figure 5.5: Average increase of temperature for a restricted time ranges inside plasma phase, with exponential and linear interpolations. The exponential fit shows the analytical solution for equation 5.1, the linear fit is the one from which power is extrapolated.

T_0 is a temperature limit and k a constant parameter dependant from the target.

$$mc_p \frac{dT}{dt} = P - k(T - T_{\lim}) \quad (5.1)$$

The analytical result of this equation is an exponential function, as in figure 5.5 for the center pixel in the image. The downside of the exponential fit it's that isn't possible to evaluate the contribution of power deposition from it. From temperature variation for temperatures close to T_0 , where the thermalization contribute is neglectable, is possible to extrapolate parameter P with a linear fit. The power parameter resulting from this interpolation is not a precise value because there are also thermalization contributes, but it is useful to study its behavior varying other parameters.

To assure that temperature variation are observed only inside the target, only pixels within a radius of 7 mm from the center of plasma application are considered. The average temperature variation in those conditions follows equation 5.2, where ρ is aluminium density, h is target width, A_p is target area, T_{avg} is the average temperature of a pixel, T_p is the temperature of a pixel.

$$mc_p T_{\text{avg}}(t) = \rho h A_p \frac{\sum_{\text{pixels}} T_p}{N_{\text{pixels}}} = Pt + T_0 \quad (5.2)$$

Plasma deposition isn't continuous in time but it happens within time intervals, as described in chapter 3. Power evaluated considering the total time interval of plasma application is an effective power P_{eff} that doesn't take into consideration the real time interval of interaction between plasma and target, a fraction of the total one. An estimate of the power associated with a single pulse P_{pulse} can be found considering the time interval for the interaction of every pulse Δt_{pulse} multiplied by the rate of pulses during the discharge f , as in equation 5.3. An appropriate time pulse duration is $\Delta t_{\text{pulse}} = 1 \mu\text{s}$, as shown in chapter 3.

$$P_{\text{pulse}} = \frac{P_{\text{eff}}}{\Delta t_{\text{pulse}} f} \quad (5.3)$$

Pulse rate dependency Power parameter is evaluated with different pulse repetition rate, voltage peak value set at $V_p = 7.2 \text{ kV}$ and distance between source and target $d = 5.5 \text{ mm}$. In figure 5.6 there are effective power during the discharge and the pulse power relative to a single pulse. As expected the effective power is proportional to frequency of pulses: greater frequency means more pulses in a

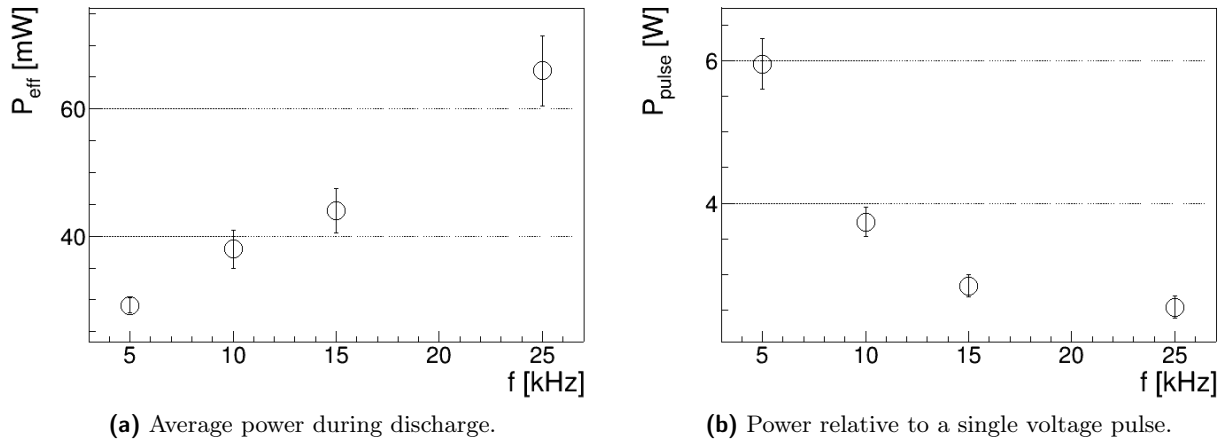


Figure 5.6: Plasma power deposition on target for different pulse repetition rates.

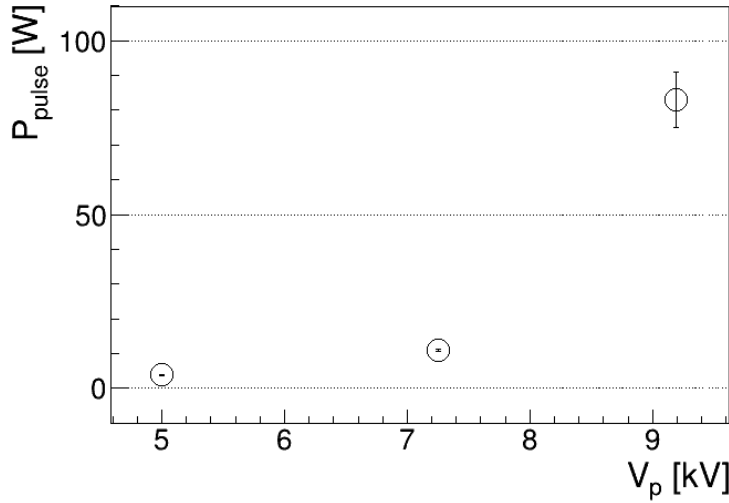


Figure 5.7: Plasma power of a single pulse for different voltage peak values.

given time. It's instead interesting to note that power for a single pulse decreases with increasing pulse rate. An explanation could be that for different pulse repetition rate the time interval relative to the single pulse, i.e. the time interval during which we see plasma bullets, decreases from $\Delta t_{\text{pulse}} = 1 \mu\text{s}$ for $f = 5 \text{ kHz}$ to values around $\Delta t_{\text{pulse}} = 500 \text{ ns}$ for $f = 25 \text{ kHz}$. This result could imply that for higher frequencies bullets have increasing speed.

Voltage peak value dependency Temperature increase is observed with distance between source and target $d = 5.5 \text{ mm}$ and pulse repetition rate $f = 5 \text{ kHz}$, for different voltage values. From figure 5.7 it is possible to see that power for the single pulse is correlated with the voltage peak value and increases rapidly when voltage increases. For voltage values from 5.0 kV to 9.2 kV temperature increase rate goes from 7.8 mK/s to 85.2 mK/s . With the higher voltage it is observed a temperature increase up to 2.2 K in 25 s of plasma application. This behavior is expected because with an higher peak voltage value there is more electrical power transferred from the source and bullets have higher velocity, as described in chapter 3.

Distance dependency The influence of the distance between target and source is measured setting voltage peak at $V_p = 7.2 \text{ kV}$ and $f = 5 \text{ kHz}$. In figure 5.8 it is possible to see how power decreases with increasing distance, as expected because for higher distances between source and target, bullets lose more energy before the impact and will transfer less energy to the target. For distance going from

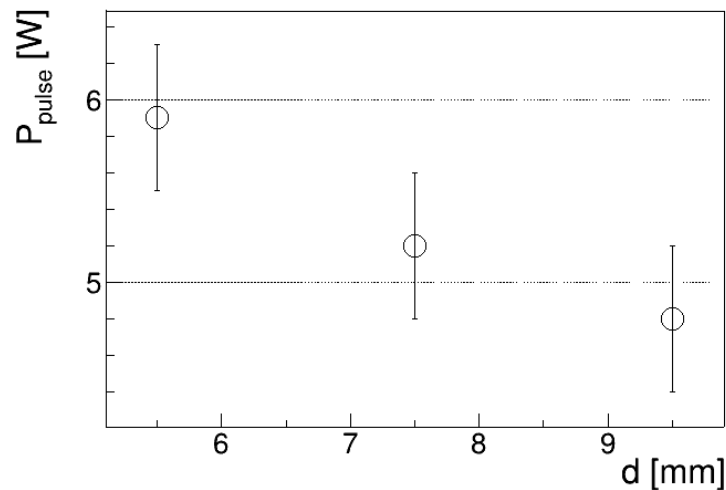


Figure 5.8: Plasma power of a single pulse for different target distances.

5.5 mm to 7.5 mm the pulse power loss rate is of 0.28 ± 0.05 W/mm.

Chapter 6

Conclusions

In this work a source for Cold Atmospheric Plasma has been developed, characterized and utilized to study formation and propagation of plasma produced with a DBD reactor. The source presents an electrode covered in dielectric placed inside a nozzle where there is neutral gas flowing. The electrode applies an electric field to the neutral gas producing plasma that is expelled in air.

The first phase of this work was to develop the components for a new prototype of the source and assemble them. Source scheme follows the one used to build older prototypes, with some changes to increase source efficiency. To create the electric field the source sends a fast voltage pulse to the electrode. The source was calibrated to know the voltage output in function of parameters set in the instrument, with or without helium gas flow that allows plasma production. The voltage waveform is a fast positive pulse with a FWHM always lower than 1 μ s. Voltage peak value is linear in a range from 4 to 10 kV, with or without plasma. Pulse repetition rate does not change voltage peak value, it is verified to be the same for rates from 5 to 40 kHz. With plasma is possible to measure current intensity flowing in a conductive target in front of the source. Also for current is measured a positive pulse with time width lower than 1 μ s. This DBD source is developed for biomedical uses, a fundamental feature is that current deposited on a target should stay below a limit value usually set greater than 10 mA. Measured peak current intensity is always less than 4 mA. A useful estimate of the effective current intensity sensed by a living target is an average value in a longer time interval. For a time interval of 1 ms the effective current is ≤ 0.3 mA, below any possible limit value for medical application. Current peak value results proportional to voltage peak value on the electrode, showing that plasma adds a resistive load between electrode and target. Plasma electrical resistance is estimated between 2.98 ± 0.11 M Ω and 11.82 ± 2.19 M Ω , different for different voltage peaks. In table 6.1 there is a summary of the electric parameters here described.

Range	
f	5-40 kHz
V_p	4-10 kV
I_p	0-4 mA
I_{eff}	0-0.3 mA
R_{pl}	3-12 M Ω

Table 6.1: Electric parameters of PCC and produced plasma. f is the voltage pulse repetition rate; V_p is the voltage peak applied on the electrode; I_p is current peak intensity measured on a conductive target in front of the source; I_{eff} is the average current intensity in a time interval of 1 ms; R_{pl} is an estimation of plasma resistance.

The main analysis done in this work revolves around the study of plasma propagation. Plasma produced with helium and neon gas propagates with the shape of *bullets*: localized portions of gas that emit light

and move with velocities ≥ 10 km/s. Bullets produced by PCC are observed with a fast acquisition setup that integrates plasma light emission in an interval of 15 ns. Resulting frames are analyzed to study position, dimensions and evaluate velocities of the bullets. Measurements are taken with helium and neon, for different experimental setups, changing voltage peak value, gas flow and target place in front of the source.

Bullet behavior is qualitatively the same for helium and neon gas, with a flow of 2 L/min. Plasma is observed around the electrode when voltage reaches a value over 5 kV. After formation, plasma covers all the nozzle area and the bullet moves away from the electrode, towards the end of the nozzle. Once it reaches the end of the nozzle the bullet speeds up and exits rapidly from it, propagating in the air outside. If there is not a target or if there is an insulating target, the bullet propagates in air decelerating until it stops or until the impact with the target. When an higher voltage pulse is applied on the electrode, bullets travel inside the nozzle with higher velocity and reach higher distances in air. One difference between helium and neon bullets is that the second ones have higher velocities for the same voltage value, but they travel shorter distances in air. Helium plasma bullets, for a voltage peak value between 5.5 and 7.5 kV, reach velocities inside the nozzle from 38 to 60 km/s, traveling distances from the end of the nozzle from 4 to 23 mm. Neon plasma bullets, for a voltage peak value between 4.5 and 6.5 kV, reach velocities inside the nozzle from 35 to 63 km/s, traveling distances from 6 to 15 mm.

A model that describes this exact behavior is not known yet. In this work it is excluded that the motion of the bullet is related to propagation of ion waves and it is demonstrated that it is related to electron mobility. A charged particle in an electric field E moves with a drift velocity $v_d = \mu E$, where μ is the particle mobility. The electron mobility, μ_e varies in function of reactions that happens inside the plasma. Simulation software *Bolsig+* gives an estimation of transport coefficients in a plasma inside an electric field, including μ_e , with settable composition of ionized gas.

The behaviour of electron drift velocity in a gas of helium, neon or a mix of helium and air reflects results found in the experiment. For a gas of helium or neon around 300 K, inside an electric field from 300 to 700 V/mm, at atmospheric pressure, it is found that μ_e is a near costant value, higher for neon. Drift velocities $v_d = \mu_e E$ are values ≥ 10 km/s and decrease linearly for decreasing electric field. This behaviour is comparable to the one found for bullet velocities inside the nozzle, where the electric field decreases moving away from the electrode and with decreasing voltage. Electron mobility μ_e is also evaluated for a gas of helium mixed with another gas of 70% nitrogen and 30% oxygen. Different gas composition introduces different reactions inside the gas, changing electron mobility. A gradual increase in the fraction of the second gas allows to simulate the contact of helium with air. For every value of the electric field drift velocities show a peak with low fraction of air in Helium, decreasing once the percentage grows over 20%. This behaviour resembles the acceleration of bullets when there is contact between gas flow and air outside the nozzle. It can be concluded that bullet velocity follows the behaviour of electron drift velocity, proportional to electron mobility. Further simulations or a model for plasma bullets could investigate this relation to understand how they are related.

For helium bullets it is studied the influence of gas flow in bullet behaviour, going from 1 to 4 L/min. Minimum velocity inside the nozzle and distance reached in air are inversely proportional to gas flow, i.e. they are lower with higher flow. Inside the nozzle there is always laminar flow, Reynold numbers are $R_n < 200$, distant from the critical value of 2000 identified as the transition value to turbulent flow. Lower velocity, and consequently the shorter distances reached, could be related to the different contact point between helium and air. If the flow is higher, the bullet propagates for more distance in a gas of (almost) pure helium, decelerating more before the acceleration due to impact with air.

The presence of an insulating target in front of the source does not influence bullet propagation. After the impact between bullet and target, both helium and neon bullets continue to propagate on the surface of the insulating target. The propagation on the target is observed as a round shaped figure with increasing diameter on the target. Maximum diameter and the velocity of expansion are proportional to voltage value and inversely proportional to distance between source and target. This behaviour is analogous to bullet propagation in air.

A conductive grounded target changes the behaviour of bullet propagation: velocities in air do not decrease before reaching the target. The bullet stops only after the impact with the target, reaching further distances. A conductive grounded target attracts the bullet. With the conductive target it is also possible to compare current measurements with the bullet motion. The most interesting result is that the current pulse starts to rise before the bullet reaches the target. Current pulse's starting time and maximum time are inversely proportional to distance between source and target and are proportional to voltage applied on the electrode. This phenomenon can be explained with the hypothesis that there is a portion of the bullet that does not emit light but carries charge. When a higher voltage is applied on the electrode all the bullet moves with higher velocity and current is measured before.

Bullet formation and propagation are not observed if plasma is produced ionizing argon. From the measurements with the fast camera it is possible to see that argon plasma does not form an homogeneous zone of glowing plasma, a bullet, but inside the nozzle there are several filaments. Those filaments start at the electrode and have different lengths in each frame. During the discharge the average value of the position reached by the end of the filaments moves towards the end of the nozzle. Once this value reaches the end of the nozzle it can be seen that plasma is expelled as formations of round shaped glowing gas, short in height and width. Those circles have a well defined position and dimensions, allowing to study the motion of the average values of their position and dimensions, as done with position and dimensions of Helium and Neon bullet. The result is that the average value of those formations moves away from nozzle end, with velocities from 30 to 60 km/s, depending on the presence of a conductive grounded target or of a grounded ring placed around the nozzle.

Reactive species produced inside plasma are thought to be related to the mechanism behind therapeutic effects of plasma biomedical applications. With spectrometric measurements it is possible to observe which of these species are inside the plasma. In this study plasma emission is analyzed with two spectrometers in the wavelength range between 200 and 800 nm.

Helium plasma emission lines are recognized with an high resolution spectrometer. It is possible to distinguish lines relative to OH rotational transitions, N₂ rotational and vibrational transitions, N₂⁺ vibrational transitions and other lines relative to O and He. The ratio between emission lines in a rotational band is related to the rotational temperature of the relative molecule. Rotational temperature can be considered an estimation of gas temperature. Resulting temperatures for OH and N₂ are $T_{r,\text{OH}} = 352 \pm 38$ K and $T_{r,\text{N}_2} = 321 \pm 41$ K, two values compatible with each other and comparable to room temperature. From N₂ vibrational transitions is possible to give also an estimation of its vibrational temperature $T_{v,\text{N}_2} = 3405 \pm 154$ K.

Emission is different for different positions inside the plasma plume. With a mini spectrometer is observed emission intensity at different heights of the column of helium plasma, neon plasma and argon plasma. Emission intensity relative to N₂ always increases going from the electrode to the air outside, while specific emission intensity for the gas used to start the discharge decreases. It is an expected result as the concentration of the gas used to start the discharge is higher inside the nozzle, while concentration of nitrogen is higher in the air outside.

Emission depends also on gas composition. With the same mini spectrometer is observed the variation in emission introducing a percentage of nitrogen or argon in a flux of Helium. Nitrogen up to the 10% of total gas flux does not increase emission intensity for N₂ lines. Nitrogen is the principal component of air so it is possible that the percentage inserted in the gas flux is low respect the quantity already present. With an increasing percentage of argon there is an increase in the emission intensity relative to argon lines, and a decrease of the one relative to N₂ and He lines.

A fundamental requirement for plasma produced by PCC is that it cannot increase temperature target over a certain safe limit. In this work is estimated power deposited by plasma on a target. As explained before, plasma production is a pulsed phenomenon, the power relative to a single pulse can be evaluated considering the time interval of interaction between plasma and target of 1 μ s. Typical values for the effective power deposited on the target are between 20 and 50 mW, while the power relative to a single pulse is between 2 and 6 W. Power for a single pulse decreases with increasing pulse repetition rate. It

is an unexpected result that could imply a different bullet behavior for different pulse repetition rates. Power for a single pulse increases rapidly with increasing voltage, while it decreases with increasing distance. It is expected because plasma bullets have more speed when there is a higher peak voltage on the electrode or when the target is placed closer to the source. Under the condition of negligible interaction between heating transfer mechanisms in biological living tissues and plasma deposition, with those power estimations it is possible to evaluate the increase in temperature when plasma produced by PCC will be applied for blood coagulation.

A future development for this thesis is the formulation of a model that explains all the observations here presented. A model that describes plasma bullets would help to understand and predict plasma electric behavior, plasma radiation emission and plasma power deposition on a target. Measurements made in this work give description on DBD plasma phenomenology that will be used to test future models.

Bibliography

- [1] M G. Kong et al. “Plasma medicine: An introductory review”. In: *New Journal of Physics* 11 (Nov. 2009). DOI: 10.1088/1367-2630/11/11/115012.
- [2] Gianluca De Masi et al. “Plasma Coagulation Controller: A Low- Power Atmospheric Plasma Source for Accelerated Blood Coagulation”. In: *Plasma Medicine* 8.3 (2018), pp. 245–254. ISSN: 1947-5764.
- [3] Victor J. Thannickal and Barry L. Fanburg. “Reactive oxygen species in cell signaling”. In: *American Journal of Physiology-Lung Cellular and Molecular Physiology* 279.6 (2000), pp. L1005–L1028. DOI: 10.1152/ajplung.2000.279.6.L1005.
- [4] Ursula Rauen et al. “Nitric oxide increases toxicity of hydrogen peroxide against rat liver endothelial cells and hepatocytes by inhibition of hydrogen peroxide degradation”. In: *American Journal of Physiology-Cell Physiology* 292.4 (2007), pp. C1440–C1449. DOI: 10.1152/ajpcell.00366.2006.
- [5] E Martines et al. “A novel plasma source for sterilization of living tissues”. In: *New Journal of Physics* 11.11 (2009). DOI: 10.1088/1367-2630/11/11/115014.
- [6] E Stoffels et al. “Mass spectrometric detection of short-living radicals produced by a plasma needle”. In: *Plasma Sources Science and Technology* 16.3 (2007). DOI: 10.1088/0963-0252/16/3/014.
- [7] Gregory Fridman et al. “Blood Coagulation and Living Tissue Sterilization by Floating-Electrode Dielectric Barrier Discharge in Air”. In: *Plasma Chemistry and Plasma Processing* 26.4 (2006), pp. 425–442. DOI: 10.1007/s11090-006-9024-4.
- [8] Beate Haertel et al. “Non-Thermal Atmospheric-Pressure Plasma Possible Application in Wound Healing”. In: *Biomolecules & Therapeutics* 22.6 (2014). DOI: 10.4062/biomolther.2014.105.
- [9] Dayun Yan, Jonathan H. Sherman, and Michael Keidar. “Cold atmospheric plasma, a novel promising anti-cancer treatment modality”. In: *Oncotarget* 8.9 (2016). DOI: 10.18632/oncotarget.13304.
- [10] M. Laroussi. “Nonthermal decontamination of biological media by atmospheric-pressure plasmas: review, analysis, and prospects”. In: *IEEE Transactions on Plasma Science* 30.4 (2002), pp. 1409–1415. DOI: 10.1109/TPS.2002.804220.
- [11] X. Deng, J. Shi, and M. G. Kong. “Physical Mechanisms of Inactivation of *Bacillus subtilis* Spores Using Cold Atmospheric Plasmas”. In: *IEEE Transactions on Plasma Science* 34.4 (2006), pp. 1310–1316. DOI: 10.1109/TPS.2006.877739.
- [12] S. U. Kalghatgi et al. “Mechanism of Blood Coagulation by Nonthermal Atmospheric Pressure Dielectric Barrier Discharge Plasma”. In: *IEEE Transactions on Plasma Science* 35.5 (2007), pp. 1559–1566. DOI: 10.1109/TPS.2007.905953.
- [13] A. Von Engel and J.R. Cozens. “Flame Plasmas”. In: ed. by L. Marton. Vol. 20. Advances in Electronics and Electron Physics. Academic Press, 1965, pp. 99 –146.
- [14] M. Goossens. *An Introduction to Plasma Astrophysics and Magnetohydrodynamics*. Astrophysics and Space Science Library. Springer Netherlands, 2012. ISBN: 9789400710764.

- [15] X M Zhu et al. "Measurement of the electron density in atmospheric-pressure low-temperature argon discharges by line-ratio method of optical emission spectroscopy". In: *Journal of Physics D: Applied Physics* 42.14 (2009). DOI: 10.1088/0022-3727/42/14/142003.
- [16] R Ohyama, M Sakamoto, and A Nagai. "Axial plasma density propagation of barrier discharge non-thermal plasma bullets in an atmospheric pressure argon gas stream". In: *Journal of Physics D: Applied Physics* 42.10 (2009), p. 105203. DOI: 10.1088/0022-3727/42/10/105203.
- [17] J Amorim, M A Ridenti, and V Guerra. "Experimental and theoretical study of atmospheric-pressure argon microplasma jets". In: *Plasma Physics and Controlled Fusion* 57.7 (2015), p. 074001. DOI: 10.1088/0741-3335/57/7/074001.
- [18] Thomas J. Bruno W. M. Haynes David R. Lide. *CRC handbook of chemistry and physics: a ready-reference book of chemical and physical data*. 99th edition. CRC Press. ISBN: 978-1-4987-5429-3, 1498754295.
- [19] L. Bárdos and H. Baránková. "Cold atmospheric plasma: Sources, processes, and applications". In: *Thin Solid Films* 518.23 (2010). ISSN: 0040-6090.
- [20] Gregory Fridman et al. "Applied Plasma Medicine". In: *Plasma Processes and Polymers* 5.6 (). DOI: 10.1002/ppap.200700154.
- [21] Ulrich Kogelschatz. "Dielectric-Barrier Discharges: Their History, Discharge Physics, and Industrial Applications". In: *Plasma Chemistry and Plasma Processing* 23.1 (2003). DOI: 10.1023/A:1022470901385.
- [22] By E. V. Shun'ko. URL: <https://commons.wikimedia.org/w/index.php?curid=27512503>.
- [23] Ya. Z. Slutsker et al. "Electrical model of cold atmospheric plasma gun". In: *Physics of Plasmas* 24.10 (2017), p. 103510. DOI: 10.1063/1.4986023.
- [24] Tao Shao et al. "Electrical characterization of dielectric barrier discharge driven by repetitive nanosecond pulses in atmospheric air". In: *Journal of Electrostatics* 67.2 (2009), pp. 215 –221.
- [25] E Stoffels et al. "Plasma needle for medical treatment: recent developments and perspectives". In: *Plasma Sources Science and Technology* 15.4 (2006), S169–S180. DOI: 10.1088/0963-0252/15/4/s03.
- [26] M. Laroussi and X. Lu. "Room-temperature atmospheric pressure plasma plume for biomedical applications". In: *Applied Physics Letters* 87.11 (2005), p. 113902. DOI: 10.1063/1.2045549.
- [27] XinPei Lu and Mounir Laroussi. "Dynamics of an Atmospheric Pressure Plasma Plume Generated by Submicrosecond Voltage Pulses". In: 2016.
- [28] Cecilia Piferi. "Caratterizzazione di sorgenti di plasma per applicazioni mediche". 2016/17.
- [29] *Coils core datasheet*. URL: https://www.mouser.it/datasheet/2/400/e_32_16_9-1527777.pdf.
- [30] J. Upadhyay et al. "Development of high-voltage pulse generator with variable amplitude and duration". In: *Review of Scientific Instruments* 85.6 (2014), p. 064704. DOI: 10.1063/1.4884883.
- [31] Julien Jarrige, Mounir Laroussi, and Erdinc Karakas. "Formation and dynamics of plasma bullets in a non-thermal plasma jet: influence of the high-voltage parameters on the plume characteristics". In: *Plasma Sources Science and Technology* 19.6 (2010), p. 065005. DOI: 10.1088/0963-0252/19/6/065005. URL: <https://doi.org/10.1088%2F0963-0252%2F19%2F6%2F065005>.
- [32] T Darny et al. "Analysis of conductive target influence in plasma jet experiments through helium metastable and electric field measurements". In: *Plasma Sources Science and Technology* 26.4 (2017), p. 045008. DOI: 10.1088/1361-6595/aa5b15.
- [33] *ROOT documentation for TVirtualFFT class*. URL: <https://root.cern.ch/doc/master/classTVirtualFFT.html>.
- [34] R. Brun. *ROOT documentation for Landau() function*. 1995. URL: <https://root.cern.ch/doc/master/namespacETMath.html#a656690875991a17d35e8a514f37f35d9>.

- [35] U. Kogelschatz, B. Eliasson, and W. Egli. "Dielectric-Barrier Discharges. Principle and Applications". In: *Journal de Physique IV Colloque* 07.C4 (1997), pp. C4–47–C4–66. DOI: 10.1051/jp4:1997405.
- [36] Takaaki Tomai, Tsuyohito Ito, and Kazuo Terashima. "Generation of dielectric barrier discharge in high-pressure N₂ and CO₂ environments up to supercritical conditions". In: *Thin Solid Films* 506–507 (2006), pp. 409 –413. ISSN: 0040-6090. DOI: <https://doi.org/10.1016/j.tsf.2005.08.101>.
- [37] Lewi Tonks and Irving Langmuir. "A General Theory of the Plasma of an Arc". In: *Phys. Rev.* 34 (6 1929), pp. 876–922. DOI: 10.1103/PhysRev.34.876.
- [38] M.A. Lieberman and A.J. Lichtenberg. *Principles of Plasma Discharges and Materials Processing*. Wiley, 1994. ISBN: 9780471005773.
- [39] Stephanie Tümmel et al. "Low Temperature Plasma Treatment of Living Human Cells". In: *Plasma Processes and Polymers* 4.S1 (2007), S465–S469. DOI: 10.1002/ppap.200731208.
- [40] N Mericam-Bourdet et al. "Experimental investigations of plasma bullets". In: *Journal of Physics D: Applied Physics* 42.5 (2009), p. 055207. DOI: 10.1088/0022-3727/42/5/055207.
- [41] Eric Robert et al. "Experimental Study of a Compact Nanosecond Plasma Gun". In: *Plasma Processes and Polymers* 6.12 (2009), pp. 795–802. DOI: 10.1002/ppap.200900078.
- [42] Wen Yan and Demetre J. Economou. "Simulation of a non-equilibrium helium plasma bullet emerging into oxygen at high pressure (250–760Torr) and interacting with a substrate". In: *Journal of Applied Physics* 120.12 (2016), p. 123304. DOI: 10.1063/1.4963115.
- [43] D Breden, K Miki, and L L Raja. "Self-consistent two-dimensional modeling of cold atmospheric-pressure plasma jets/bullets". In: *Plasma Sources Science and Technology* 21.3 (2012), p. 034011. DOI: 10.1088/0963-0252/21/3/034011.
- [44] Seth A. Norberg, Eric Johnsen, and Mark J. Kushner. "Helium atmospheric pressure plasma jets touching dielectric and metal surfaces". In: *Journal of Applied Physics* 118.1 (2015), p. 013301. DOI: 10.1063/1.4923345.
- [45] *Flea camera datasheet*. URL: <https://www.ptgrey.com/Content/Images/uploaded/Flea.pdf>.
- [46] *How to read a pgm file*. URL: <http://netpbm.sourceforge.net/doc/pgm.html>.
- [47] Julien Jarrige, Mounir Laroussi, and Erdinc Karakas. "Formation and dynamics of plasma bullets in a non-thermal plasma jet: influence of the high-voltage parameters on the plume characteristics". In: *Plasma Sources Science and Technology* 19.6 (2010), p. 065005. DOI: 10.1088/0963-0252/19/6/065005.
- [48] R. Brun. *ROOT documentation for TH2 class*. URL: <https://root.cern.ch/doc/master/classTH2.html>.
- [49] ashok kumar Singh and Beer Bhaduria. "Finite Difference Formulae for Unequal Sub-Intervals Using Lagrange's Interpolation Formula". In: *Journal of Math. Analysis* 3 (Jan. 2009), pp. 815–827.
- [50] Dong Jun Jin, Han S. Uhm, and Guangsup Cho. "Influence of the gas-flow Reynolds number on a plasma column in a glass tube". In: *Physics of Plasmas* 20.8 (2013), p. 083513. DOI: 10.1063/1.4819246.
- [51] G J M Hagelaar and L C Pitchford. "Solving the Boltzmann equation to obtain electron transport coefficients and rate coefficients for fluid models". In: *Plasma Sources Science and Technology* 14.4 (2005), pp. 722–733. DOI: 10.1088/0963-0252/14/4/011.
- [52] *Various databases, retrieved on March 14, 2019*. URL: <https://www.lxcat.net>.
- [53] Francis F. Chen. *Introduction to Plasma Physics and Controlled Fusion*. 2nd. 1984.
- [54] Yuri P. Raizer. *Gas Discharge Physics*. 1991. DOI: 10.1007/978-3-642-61247-3.

- [55] A S Dickinson, Malsoon Seo Lee, and L A Viehland. “The mobility of He ions in helium gas”. In: *Journal of Physics B: Atomic, Molecular and Optical Physics* 32.20 (1999), pp. 4919–4930. DOI: 10.1088/0953-4075/32/20/309.
- [56] H R Skullderud and P H Larsen. “Mobility and diffusion of atomic helium and neon ions in their parent gases”. In: 23.6 (1990), pp. 1017–1041. DOI: 10.1088/0953-4075/23/6/010.
- [57] Nisha Chandwani et al. “Determination of Rotational, Vibrational and Electron Temperatures in Dielectric Barrier Discharge in air at atmospheric pressure”. In: (June 2014). DOI: 10.13140/RG.2.1.2078.6725.
- [58] Ioana Gerber et al. “Air Dielectric Barrier Discharge Plasma Source For In Vitro Cancer Studies”. In: *Clinical Plasma Medicine* 9 (Feb. 2018), p. 4. DOI: 10.1016/j.cpme.2017.12.006.
- [59] S. P. Kuo et al. “Applications of Air Plasma for Wound Bleeding Control and Healing”. In: *IEEE Transactions on Plasma Science* 40.4 (2012), pp. 1117–1123. ISSN: 0093-3813. DOI: 10.1109/TPS.2012.2184142.
- [60] Hans-Joachim Kunze (auth.) *Introduction to Plasma Spectroscopy*. 1st ed. Springer Series on Atomic, Optical, and Plasma Physics 56. Springer-Verlag Berlin Heidelberg, 2009. ISBN: 9783642022326,3642022326.
- [61] Gerhard Herzberg. *Molecular Spectra and Molecular Structure I: Spectra of Diatomic Molecules*. 2nd. D. Van Nostrand, 1950. ISBN: 9780442033859,0442033850.
- [62] Wikipedia contributors. *Vibronic spectroscopy*. 2018. URL: https://en.wikipedia.org/w/index.php?title=Vibronic_spectroscopy&oldid=823782704.
- [63] I A Kossyi et al. “Kinetic scheme of the non-equilibrium discharge in nitrogen-oxygen mixtures”. In: *Plasma Sources Science and Technology* 1.3 (1992), pp. 207–220. DOI: 10.1088/0963-0252/1/3/011.
- [64] LIAM E. GUMLEY. *Practical IDL Programming*. San Francisco: Morgan Kaufmann, 2002. ISBN: 978-1-55860-700-2.
- [65] M. Miroslav. *ROOT documentation for TSpectrum class*. URL: <https://root.cern.ch/doc/v614/classTSpectrum.html>.
- [66] Andre Knie. “Photon induced inner-shell excitation processes of nitrous oxide probed by angle resolved fluorescence and Auger-Electron spectrometry”. Dr. Kassel: Univ. Kassel, 2013. ISBN: 978-3862194582.
- [67] H.A. Van Sprang, H.H. Brongersma, and F.J. De Heer. “Absolute emission cross sections for the calibration of optical detection systems in the 120–250 nm range”. In: *Chemical Physics Letters* 65.1 (1979), pp. 55 –60. ISSN: 0009-2614.
- [68] C. de IZARRA. “COMPUTER SIMULATION OF THE UV OH BAND SPECTRUM”. In: *International Journal of Modern Physics C* 11.05 (2000), pp. 987–998. DOI: 10.1142/S0129183100000857.
- [69] S. B. Bayram and M. V. Freamat. “Vibrational spectra of N₂: An advanced undergraduate laboratory in atomic and molecular spectroscopy”. In: *American Journal of Physics* 80.8 (2012), pp. 664–669. DOI: 10.1119/1.4722793.
- [70] N Britun et al. “Determination of the vibrational, rotational and electron temperatures in N₂and Ar–N₂rf discharge”. In: *Journal of Physics D: Applied Physics* 40.4 (2007), pp. 1022–1029. DOI: 10.1088/0022-3727/40/4/016.
- [71] A. Kramida et al. *NIST Atomic Spectra Database*. 2018. URL: <https://physics.nist.gov/asd>.
- [72] Se Youn Moon and W. Choe. “A comparative study of rotational temperatures using diatomic OH, O₂ and N₂+ molecular spectra emitted from atmospheric plasmas”. In: *Spectrochimica Acta Part B: Atomic Spectroscopy* 58.2 (2003). INTERSIBGEOCHEM 01, pp. 249 –257. ISSN: 0584-8547.
- [73] Charles de Izarra. “UV OH spectrum used as a molecular pyrometer”. In: *Journal of Physics D: Applied Physics* 33.14 (2000), pp. 1697–1704. DOI: 10.1088/0022-3727/33/14/309.

- [74] Gopal Chandra Shit and Amal Bera. “Temperature Response in a Living Tissue with Different Heating Source at the Skin Surface Under Relaxation Time”. In: *International Journal of Applied and Computational Mathematics* (Dec. 2015). DOI: 10.1007/s40819-015-0120-0.
- [75] Kerstin Giering et al. “Review of Thermal Properties of Biological Tissues”. In: *SPIE-The International Society For Optical Engineering* (1995), pp. 45–65.
- [76] Rikke Gade and Thomas B. Moeslund. “Thermal cameras and applications: a survey”. In: *Machine Vision and Applications* 25.1 (2014), pp. 245–262. ISSN: 1432-1769. DOI: 10.1007/s00138-013-0570-5.
- [77] *Flir thermal camera datasheet*. URL: https://www.flir.com/globalassets/imported-assets/document/rnd_011_us.pdf.
- [78] Antonio Pimazzoni. “Investigation of the parameters of a particle beam by numerical models and diagnostic calorimetry”. PhD thesis. Università degli Studi di Padova, 2018.